Université du Québec

Institut national de la recherche scientifique

Énergie Matériaux Télécommunications

Reconfigurable Metamaterial-based Antenna Using a Novel class of Miniaturized Agile Unit-cells

by

Behnam Zarghooni

A dissertation submitted in partial fulfillment of the requirements for the degree of
Doctor of Philosophy (Ph. D.) in Telecommunications

Evaluation Jury

Research director	Prof. Tayeb A. Denidni
	INRS-EMT
Internal examiner	Prof. Serioja O. Tatu
	INRS-EMT
External examiner	Prof. Cevdet Akyel
	École Polytechnique de Montréal
External examiner	Dr. Michel Clénet
	Defence Research and Development Canada

To my dear father Mr. Rahmatolah Zarghooni who inspired me to become an engineer and to my dear mother Mrs. Touran Doroudgar who filled my heart with love and affection and to my lovely wife and the biggest adventure of my life Mahsa.

Abstract

In this thesis, a new class of reconfigurable and compact metamaterial unit-cells is introduced and used to present a novel technique for beam-switching antennas. Two metamaterial inspired antennas are designed and implemented using this technique at two different frequency bands i.e. S-band and millimeter-wave band.

The prospective role of reconfigurable unit-cells in the future of metamaterial theory is investigated and a novel reconfigurable metamaterial unit-cell is designed that can provide a controllable refractive index. Moreover, a novel miniaturization technique is introduced that can be applied on any rectangular-shaped metamaterial unit-cell. This technique is analytically investigated and a step-by-step guideline is provided. A combination of these two concepts is exploited to design a controllable metamaterial medium that can be easily integrated in the structure of planar antennas.

As the final objective of this work, the aforementioned artificial medium is embedded on the substrate of a planar dipole antenna and a radiation-pattern reconfigurable antenna with a switchable beam in the E-plane is designed and implemented in the S-band. The same technique is used at millimeter waves and an antenna with deflected beam in this band is presented.

Both antenna structures are fabricated and measured to validate the simulation results. Also, the designed unit-cells in the S-band are fabricated and the performance of the unit-cells is verified by a modified version of the well-known free-space measurement method. Two custom-made dielectric lenses are designed and fabricated for this method. Furthermore, an analytical model is derived to explain the beam-tilting effect produced by the metamaterial unit-cells. This model successfully describes the behavior of both antennas at the vicinity of the metamaterial unit-cells.

Table of Contents

Chapter 1 Introduction

Chapter 2 Reconfigurable Antennas

Chapter 3 Millimeter Waves

Chapter 4 Metamaterials

Chapter 5 Stepped-Impedance Resonator (SIR) Technique, for miniaturization of Rectangular Metamaterial Unit-cells

Chapter 6 The Unit-cell Structure

Chapter 7 The Antenna Structure

Chapter 8 The Paraffin Lens

Chapter 9 Conclusion and Future Research

Chapter 10 Résumé

References

List of Figures

List of Tables

Chapter 1

Introduction

1.1 Motivation

Today, modern telecommunication systems provide us with various functionalities such as high data-rate transmission, multiband performance and different diversities, but at the same time, it should be low-cost, robust, compact and easy to use. All these points show that if multiple functions can be preformed by a single system, the cost and complexity of the system can be reduced significantly. That is why intelligent systems have been deployed extensively in a variety of commercial, industrial and military applications.

On the other hand, the antenna design is an inseparable part of any telecommunication system and improvement of this section can have a significant effect on the overall performance of the communication system. Therefore, employing reconfigurable antennas that are capable of providing diversity at different levels is a promising solution to enhance the system performance.

Based on the abovementioned facts, the research area of reconfigurable antennas has received ever-growing attention since several decades [1]. In fact, there are a lot of researches conducted on different aspects of reconfiguration such as radiation-pattern, directivity, polarization and frequency [2-5]. To achieve these objectives, various approaches including mechanically and electronically controlled antenna arrays or single elements have been used. In accordance with the application of the system, different techniques can be employed to implement each approach. However, it is needless to say that electrically controlled single agile antennas are always amongst the most interesting subjects due to their vast applications in modern communication systems in the form of independent antennas or array elements.

Millimeter-wave (MMW) bands (30-300 GHz) have drastically gained much focus and attracted researchers in the past few years. They have a great potential to meet the modern demands of emerging communication systems and applications. Beside the high-speed, large bandwidth and high capacity, at this regime, the integration of compact and high-efficiency antennas is very easy. These attributes make the millimeter-wave band a suitable choice for many applications such as Gigabit wireless communications, imaging sensors, automotive radars and deep-space communications [6-9]. All these systems require low-cost and high-efficiency integrated antenna solutions. Many millimeter-wave communication and radar systems require antennas with a reconfigurable radiation pattern to achieve beam-scanning or beam-shaping capabilities. Some examples are point-to-point and point-to-multipoint links, ground stations for satellites, automotive radars, deep-space communication links and Gigabit wireless indoor communication systems 43]. However, millimeter-wave bands suffer from the high attenuation characteristics associated with multipath fading, high conductor losses and mutual coupling problems. To overcome these issues and improving the system's signal to noise ratio (SNR), bit-error rate (BER) and channel capacity, different aspects of reconfigurability such as frequency-reconfiguration, polarization reconfiguration, and pattern reconfiguration can be used.
On the other hand, in the last decade, metamaterials have provided novel solutions to overcome limitations and difficulties of conventional microwave components [10] and have been extensively used in a variety of antenna applications. Today, different types of metamaterials such as zero-index, high-index and low-index materials are used in different applications [11]. However, there is still more to achieve in the metamaterial theory and features such as nonlinear and reconfigurable metamaterials are to be explored [12]. Reconfigurable metamaterials have shown a great potential in providing features required in intelligent antenna and microwave components. Moreover, to reach the final goal of the metamaterial theory, which is imitating the behavior of the atoms, one must focus on the reconfigurable metamaterial structures.

The abovementioned matters about reconfigurable antennas and millimeter waves along with the extensive applications of metamaterials have motivated us to conduct a comprehensive research in the field of reconfigurable metamaterial antennas at S-band and also millimeter waves. Consequently, this project aims to design, fabricate and test a miniaturized and reconfigurable metamaterial unit-cell in the S-band and then use this unit-cell in an integrated structure with a planar single element antenna to provide the beam-switching capability. In addition to the S-band, this antenna will be simulated and implemented at millimeter wave frequencies. We will prove that this method of beam-switching has several advantages over other conventional methods including the very low-profile structure and being free from gain drop when the beam is tilted.

1.2. Problem statement and research objectives

Recent works in the literature have presented different techniques for beam-tilting applications in different frequency bands [13]. Using controllable metamaterial unit-cells can be a promising solution for beam-switching and at the same time gain enhancement [14]. On the other hand, to be able to integrate metamaterial unit-cells with modern compact-sized antennas used in today's telecommunication systems, the size of the unit-cell should be reduced as much as possible. Different methods have been used to reduce the size of metamaterial unit-cells such as using fractal and Greek-key structures [15]. However, no controllable method has been formulized until today. Designing a reconfigurable metamaterial unit-cell is another challenging task that can help us to obtain more agility and wider bandwidth from a single unit-cell [16]. Reconfigurable unit-cells also provide the possibility to design an independent and detachable reconfigurable unit that can be attached to or be separated from the main antenna unit as needed as shown in Fig 1.1.
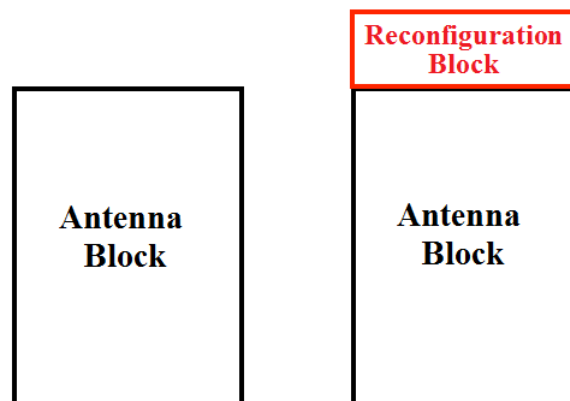
Fig. 1. 1. Detachable beam-tilting unit.

In this work, a new class of compact and reconfigurable metamaterial unit-cells is introduced. The name of RMDS, which stands for Reconfigurable Miniaturized DSR-Spiral is chosen for the unit-cell, because it can switch between a compact Spiral and an optimized Double Split-ring Resonator (DSR). Both of these configurations are miniaturized using a novel algorithm developed in this thesis that is based on the application of stepped-impedance resonators (SIRs). This unit-cell is used as an integrated metamaterial loading, which can be controlled independently in front of a planar antenna. This mechanism provides a very effective method to control the antenna beam in its azimuth plane. It is important to mention that unlike other conventional methods of beam tilting, there is no gain drop in our proposed approach and in fact, even a slight gain enhancement is noticed when the beam is tilted. To prove the effectiveness of our method, two sets of unit-cells and antennas will be developed, functioning in the S-band and millimeter waves, respectively.

As the specific objectives of our project, the two designed antenna systems must operate at 2.45 GHz and 60 GHz, respectively. Both antennas provide a sweep on the whole azimuth plane with the step of 60° over a bandwidth of 15%, while the realized gain is kept more than 6 and 9 dB for the S-band and millimeter-wave prototype respectively. This feature is highly needed in adaptive antennas capable of providing space diversity.

1.3. Organization of the Dissertation

In this section, a short explanation on the organization of this thesis is presented and the purpose of each chapter is discussed. First and foremost in Chapter 2, a literature review is performed on the concept of reconfigurable antennas. In this chapter, different aspects of reconfiguration and the existing solutions for each aspect are investigated. Secondly in Chapter 3, a brief survey is done on the millimeter waves and a variety of the applications of this band in the modern communication systems are discussed. In this chapter, pattern reconfiguration is introduced as a suitable solution to overcome the problems of the millimeter-wave band and feasible methods of reconfiguration at this band are briefly discussed. Moreover in Chapter 4, a detailed study is presented on the concept of metamaterials and various applications of these structures in reconfigurable antennas and at millimeter wave frequencies are investigated. Following all the aforementioned chapters, a comprehensive study on our novel miniaturization technique for metamaterial unit-cells is presented in Chapter 5. Furthermore, the structure of stepped impedance resonators and their applications in metamaterial unit-cells are discussed and the issues of this method for miniaturization of metamaterial structures are studied. This chapter plays an important role in the organization of the thesis and its contents are used for the design

and implementation of our metamaterial structure. The Chapter 6 is totally devoted to design, simulation, fabrication and measurement of the novel RCSD unit-cell. This unit-cell relies on DC-biased PIN-diodes to provide a reconfigurable structure. However, in this chapter first for the proof of the concept the unit-cells are replaced by short circuit and open circuit in the ON and OFF state, respectively and then real diodes are modeled and used in the structure of the unit-cell. Two different sizes of this unit-cell are presented for the S-band and the MMW band respectively. It has to be mentioned that the reconfigurable unit-cell at the MMW band is not in the scope of our work in this thesis and it will be used along with a dipole antenna to provide a millimeter-wave antenna with the tilted beam. The technique of multiple feed lines will be used to switch the beam of this antenna at the MMW band. After the design of the unit-cell, we focus on the design and implementation of the antenna in Chapter 7 and two different antennas are presented, one for each frequency band. The experimental and simulation results for all the prototypes are presented in the same chapter. In Chapter 7, we also try to reduce the effect of the bias network for the S-band antenna as much as possible. Finally, the work is concluded in Chapter 8 and a summary of the accomplishments of the thesis is presented. Furthermore in this chapter, some new ideas are introduced for possible future investigations. A detailed summary of the thesis is provided in Chapter 10 in French.

1.4 List of The Publications

[1] **B. Zarghooni** and T. A. Denidni, "New Compact Metamaterial Unit-cell Using SIR Technique," *IEEE Microw. Compon. Lett.*, vol. 24, no. 5, pp. 3150317, March 2014.

[2] **B. Zarghooni**, A. Dadgarpour and T. A. Denidni, "Effect of Stepped-Impedance Resonators on Rectangular Metamaterial Unit-cells," *Wiley Intl. Journal of RF & Microw. Computer Aided Eng.* Feb. 2015.

[3] **B. Zarghooni**, A. Dadgarpour and T. A. Denidni, "Greek-key Pattern as a Miniaturized Multiband Metamaterial Unit-cell," *IEEE Antennas Wireless Propag. Lett*. vol. 14, pp. 1254-1257, Feb. 2015.

[4] **B. Zarghooni**, A. Dadgarpour and T. A. Denidni, "Reconfigurable Planar Metamaterial Unit-cell," *IET Microw. Antennas Propag.,* March 2015.

[5] **B. Zarghooni**, A. Dadgarpour and T. A. Denidni, "Beam-switching Antenna Using Reconfigurable Metamaterial Unit-cells," Submitted to *IEEE Trans Antennas Propag.,* Aug 2015.

[6] **B. Zarghooni**, A. Dadgarpour and T. A. Denidni, "Dielectric Lens for Metamaterial Measurement," Submitted to *IEEE Trans Antennas Dielectric and Insulation,* June 2015.

[7] **B. Zarghooni**, A. Dadgarpour and T. A. Denidni, "Millimeter-wave Antenna Using Two-Sectioned Metamaterial Medium," Accepted with revision in *IEEE Antennas Wireless Propag. Lett*. May 2015.

[8] **B. Zarghooni**, A. Dadgarpour and T. A. Denidni, "Crescent-Shaped Metamaterial Unit-cell," Submitted to *IEEE Antennas Wireless Propag. Lett*. May 2015.

[9] **B. Zarghooni** and T. A. Denidni, "Supershaped Metamaterial Unit-cells Using the Gielis Formula," in *IEEE Int. Symp. on Antennas and Propag. (APSURSI)*, Vancouver, Canada, July 2015.

[10] **B. Zarghooni** and T. A. Denidni, "Reconfigurable Metamaterial Dipole Antenna," in *IEEE Int. Symp. on Antennas and Propag. (APSURSI)*, Memphis, USA, July 2014.

[11] T. A. Denidni and **B. Zarghooni**, "Stepped Impedance Resonator Technique for Metamaterial Miniaturization," invited paper in *Int. Symp. on Antenna Tech. and Applied Electromagnetics (ANTEM)*, Victoria, Canada, July 2014. *(Invited Paper)*

[12] **B. Zarghooni** and T. A. Denidni, "New Fractal Metamaterial Unit-cell for Microwave Applications," in *European Conference on Antennas Propag. (EuCap),* April 2014.

[13] **B. Zarghooni** and T. A. Denidni, "Miniaturized DNG Superstrate for Microstrip Antenna Applications," in *IEEE Int. Symp. on Antennas and Propag. (APSURSI)*, Orlando, USA, July 2013.

[14] **B. Zarghooni** and T. A. Denidni, "Design and Simulation of Novel Compact Unit-cell for DNG Metamaterials based on Stepped-Impedance Resonator Technique," in *IEEE Int. Symp. on Antennas and Propag. (APSURSI)*, Chicago, USA, July 2012.

[15] **B. Zarghooni** and T. A. Denidni, "Agile Double Negative Metamaterial Unit-cell for Advanced Antenna Applications," in *Int. Symp. on Antenna Tech. and Applied Electromagnetics (ANTEM)*, Toulouse, France, June 2012.

[16] **B. Zarghooni** and T. A. Denidni, "Design and simulation of Novel Compact and Reconfigurable Double Negative Metamaterial Unit-cell," in Int. Conf. on Metamaterials Photonic Crystals and Plasmonics (*META)*, Paris, France, April, 2012.

[17] **B. Zarghooni** and T. A. Denidni, "A partially filled substrate for a rectangular patch antenna," in *IEEE Int. Symp. on Antennas and Propag. (APSURSI)*, Washington, USA, July 2011.

[18] A. Dadgarpour, **B. Zarghooni,** B. S. Virdee and T. A. Denidni, "Beam Tilting Antenna using Integrated Metamaterial Loading," *IEEE Trans. Antennas Propag.*, vol. 62, no. 5, pp. 2874-2879, Feb. 2014.

[19] A. Dadgarpour, **B. Zarghooni,** B. S. Virdee and T. A. Denidni, "Millimeter-Wave High-Gain SIW End-Fire Bow-tie Antenna," *IEEE Trans. Antennas Propag.*, vol. 63, no. 5, pp. 2337-2342, Feb. 2015.

[20] A. Dadgarpour, **B. Zarghooni** and T. A. Denidni, "High-gain end-fire bow-tie antenna using artificial dielectric layers," *IET Microw. Antennas Propag.,* May 2015.

[21] A. Dadgarpour, **B. Zarghooni,** B. S. Virdee and T. A. Denidni, "Beam-Deflection Using Gradient Refractive-Index Media for 60 GHz End-Fire Antenna," *IEEE Trans. Antennas Propag.*, June. 2015.

[22] A. Dadgarpour, **B. Zarghooni** and T. A. Denidni, "Mutual-Coupling suppression for 60 GHz MIMO Antenna using Metamaterials," in *IEEE Int. Symp. on Antennas and Propag. (APSURSI)*, Vancouver, Canada, July 2015.

[23] A. Dadgarpour, **B. Zarghooni** and T. A. Denidni, "Beam forming bow-tie antenna for Millimeter-wave Applications using Metamaterial Lens," in *IEEE Int. Symp. on Antennas and Propag. (APSURSI)*, Vancouver, Canada, July 2015.

[24] A. Dadgarpour, **B. Zarghooni** and T. A. Denidni, "High gain planar Bow-tie Antenna Using Zero-index Metamaterials," in *IEEE Int. Symp. on Antennas and Propag. (APSURSI)*, Memphis, USA, July 2014.

[25] A. Dadgarpour, **B. Zarghooni** and T. A. Denidni, "High Gain End-fire Bow-tie Antenna Array Using Low-index Metamaterial," in *Int. Symp. on Antenna Tech. and Applied Electromagnetics (ANTEM),* Victoria, Canada, July 2014.

Chapter 2

Reconfigurable Antennas

2.1. Introduction

In recent years, demands on high quality, low cost, and high data rate communication systems, capable of adapting to unpredictable environment conditions have led to rapid growth of some attractive research subjects called adaptive or reconfigurable antennas [17,18]. The purpose of these research areas is to overcome the restrictions of conventional antennas. Of course there are some efficient techniques to use non-reconfigurable antennas in smart arrangements such as phased array systems, but using smart antennas as elements of these intelligent networks, can lead to better parameters such as scan angles and considerably enhance the overall performance of the communication system. On the other hand, if a single reconfigurable element is used instead of an intelligent array, the cost and complexity of the system can be significantly reduced.

In this chapter, the reconfigurable antennas are divided into three main groups from the aspect of the adjustable parameters i.e. bandwidth of operation, radiation-pattern and polarization. Moreover, the most common methods for each group is presented and discussed. Finally, a brief discussion about reconfigurable antennas in the millimeter-wave bands is deliberated.

2.2. Reconfigurable Antennas

2.2.1. Frequency-Reconfigurable Antennas

Today, in modern telecommunication systems, we can see many conditions where a system works in different frequency bands. The simplest scenario is the case where a transceiver transmits signals in one frequency and receives at another frequency. In this case, instead of using a separate antenna for each band, a frequency-reconfigurable antenna is used to reduce the system cost and also make it easier to implement and less bulky. The most important objective in the design of these antennas is to keep the desired radiation-pattern and polarization characteristics over all the operational frequency bands. This is a challenging task because normally the physical size of the antenna cannot be easily modified during the operation. Of course it is always possible to use mechanical switches to actually change the antenna's physical characteristics, but the alternative solution is to modify the current distribution on the antenna and change the electrical length of the structure.

Techniques in Frequency-Reconfigurable Antennas

All the various techniques used in frequency reconfiguration can be categorized in three main groups: mechanical approaches, electrical techniques and finally the methods that work on controlling the properties of the materials used in the antenna's structure.

In the mechanical methods, the antenna structure is moved or reshaped by means of electromechanical switches. As two examples of these methods, we can mention Piezo-electric actuators [19, 20] and micro-machined plastic deformation [21]. The main advantage of mechanical frequency-reconfiguration methods is that they can cover a wide range of frequencies. The other benefits of these techniques are their relatively low loss, linear behavior and low inter-modulation harmonic level. However, their major drawbacks, i.e. bulky structures and low switch speed of the actuators make them incompatible with most of modern applications.

The electrical methods usually use an array of controllable switches such as PIN-Diodes FETs and radio frequency micro-electro-mechanical switches (RF-MEMS) or variable

capacitors. These methods are much faster than mechanical methods but they have their own drawback, which is the requirement of a relatively complicated biasing network to control the switch elements.

2.2.2. Radiation-pattern Reconfigurable Antennas

Another interesting subject in smart antennas is the radiation-pattern reconfiguration. This term is used for beam-steering techniques as well as methods for controlling the antenna gain in both azimuth and elevation planes. The purpose of the radiation-pattern reconfigurable antennas is usually enhancing the link quality by simply focusing the signals to a desired direction, or to be able to alter the gain to change the coverage area. It is evident that the main method to implement these features is to control the current distribution of the antenna, which in turn leads to modify the frequency behavior and consequently the impedance matching of the antenna. Therefore, keeping the desired matching properties has to be considered when the beam or gain of the antenna is being changed.

Techniques in Radiation-Pattern-Reconfigurable Antennas

As for the frequency reconfiguration, various electrical or mechanical methods can be used to provide a reconfigurable pattern. Imagining a mechanical approach to steer the beam of the antenna is pretty easy, and all we need is to mount the antenna on a rotating structure. However, same as the previous section, these structures have the important drawback of being bulky and low-speed. Therefore, using electrically controlled elements and materials should be considered for modern communication systems. Active elements such as PIN-diodes RF-MEMS, and controllable media such as ferroelectric, ferromagnetic [22-24] are some of the common methods that are used in the literature.
There is also one more and very important method of configuration for this type of reconfigurable antennas i.e. phased array approach. In this method, a linear or multi-dimensional array of antennas is used along with a controlled feed network, which adjusts the phase of each element. The outcome of this system is the ability to control the direction of the radiated electromagnetic waves from the antenna. The phased array method is free of some of the above-mentioned difficulties for other methods. However, in this method the design of phase shifters is a challenging task and involves a lot of loss.
One other interesting method that can be used to modify the radiation pattern of an antenna is to utilize a reconfigurable artificial medium in vicinity of the antenna. Examples are reconfigurable EBG structures with controllable PIN-diodes around a dipole antenna to actively change the direction of the antenna beam [25-29]. However,

these EBG structures have their own drawbacks which include having a large-sized unit-cell compared to the wavelength, and the negative effect of the bias network that is used to control active unit-cells on the antenna parameters.

On the other hand, metamaterial structures possess very small unit-cells compared to the wavelength ($\lambda/10$), which enable us to reduce the size of the bias network. Moreover, Reconfigurable metamaterials provide the unique ability to control the effective constitutive parameters of the medium which can be very helpful to deflect and steer the antenna's beam in a desired direction.

2.2.3. Polarization-Reconfigurable Antennas

Antennas with the polarization-reconfigurable capability are used when we need to avoid the interfering signals in unpredictable environment conditions and also to provide additional degrees of freedom for antenna diversity to enhance a link quality. Polarization-reconfigurability is realized by controlling the direction of the current distribution. This is usually done by modifying the antenna itself, or the feed network. The main challenge in designing these types of antennas is to keep a good impedance matching and radiation-pattern while the polarization reconfigurability is maintained.

Techniques in Polarization-Reconfigurable Antennas

According to the available reported researches, switching techniques are among the most practical approaches to design and implement polarization-reconfigurable antennas. These methods include the application of electrically controlled elements such as PIN-diodes and RF-MEMS. Other techniques such as mechanical methods and controlling material properties are not so popular because of the difficulty of implementation and due to a high level of loss.

2.3. Conclusion

According to the survey done in this chapter, design and implementation of reconfigurable single-element antennas is a challenging task and more research is needed to be conducted in this field. The current feasible methods for reconfiguration of different parameters of the antennas suffer from high cost and complexity level, which makes it crucial to tend to novel techniques for this purpose. Using the new approaches like reconfigurable metamaterials not only enables us to exploit adaptive antennas as components of intelligent phased-array systems, but also help us to have single-element

smart antennas, which can be extremely useful in the design and implementation of low-cost, high-performance, and low-profile telecommunication systems.

Chapter 3

Millimeter Waves

3.1. Introduction

As mentioned in the objectives, one of the important goals of this thesis is to present a low-profile and efficient solution for reconfiguration of the radiation pattern in the millimeter-wave frequency band. More precisely, this design can be used for future generation of indoor Gigabit wireless LAN networks [30]. In this chapter, first the ever-growing tendency toward the millimeter waves is studied and the applications of this frequency band are briefly explained and then, the feasible reconfiguration techniques for this band are investigated. It has to be mentioned that using metamaterials for beam-tilting and reconfigurable metamaterial unit-cells for beam-switching applications is one of the novelties of our work, which is successfully designed and implemented for a planar S-band antenna (presented in Chapter 7, Section 4). The same idea has been implemented for a planar millimeter-wave (Chapter 7, Section 5).

3.2. Tendency towards the Millimeter Waves

Millimeter-wave (MMW) bands (30-300 GHz) for practical applications have regained significant interest since the last few years. They have already demonstrated a great potential to meet stringent demands for emerging wireless systems and applications thanks to the availability of potentially more matured low-cost MMW technologies. In addition to larger bandwidth, better resolution and smaller size, the integration of compact and high-efficiency antennas can be made very easy with circuit systems. Those basic attributes make MMW bands a suitable choice for a large number of anticipated applications such as gigabit wireless communications, innovative imaging sensors, efficient automotive radars and deep space communications [31].
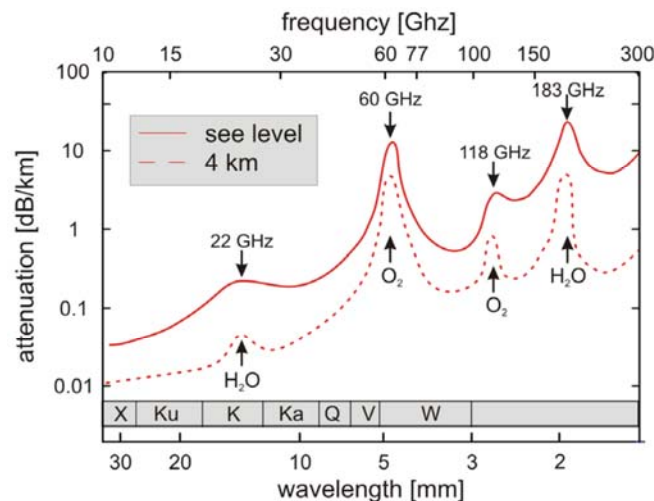
Fig. 3.1. Average atmospheric attenuation versus frequency [32].

Moreover, according to the well-known atmospheric absorption curve shown in Fig. 3.1, the attenuation of electromagnetic waves in the air decreases significantly over certain frequency ranges such as E/W-band (75-110 GHz) [32]. This physical phenomenon has spurred the main motivation for creating unique wireless systems for communications, sensing and other applications. A wide range of applications have attracted much attention from industry and academia to the exploitation of E/W-band (75-110 GHz) [25-26]. The E/W-band spectral window offers possibility great potential of gigabyte data wireless transmission over several kilometers in normal weather conditions [5]. Frequency bands of 71-76 GHz, 81-86 GHz (usually referred as E-band), and 94.1-97 GHz (part of W-band) are all allocated by the US Federal Communication Commission (FCC) as gigabyte wireless spectrum [33,34]. Over those frequency windows, the atmospheric absorption drops to less than 1dB/Km and spells out the capability of long-range gigabyte point-to-point wireless services [32]. Obviously, wide bandwidth and low

atmospheric loss allow for the E/W-band implementation of high resolution and long-range radars [35], detectors, and imaging sensors [36], which may be used in helicopter, aircraft/automobile collision avoidance radar, passive millimeter wave imaging, and radar sensors [37]. Furthermore, there are some interesting potentials in the lower section of the millimeter-wave band, where the oxygen molecule absorption causes a significant attenuation around 60 GHz. This section has been proposed for Short Range Devices (SRD). In other words, since there is a high attenuation at this frequency, it can be used for communication between two devices without causing any interference for the adjacent receivers and transmitters. The other interesting feature is the very high bandwidth at 60 GHz that is capable of providing Gigabit per second data transmission rate. Having these features makes the 60 GHz a suitable choice for the frequency of future high-speed indoor wireless LANs.

All of the abovementioned systems require low-cost and high-efficiency integrated antenna solutions. Some of those MMW systems are specified with antennas having reconfigurable radiation beam pattern to achieve beam-scanning and/or beam-reshaping capabilities that may demand for a smart use of variable gain and polarization. Those technical measures are proposed to tackle a number of problems encountered in beam-to-beam alignments and in intelligent channel capability enhancement for point-to-point backhaul applications [38].

On the other hand, from the system developer's point of view, MMW bands may suffer from high attenuation hurdles associated with potential multipath fading in special environments, high conductor/propagation losses and mutual coupling problems. To overcome these issues and improve signal-to-noise ratio (SNR), bit-error rate (BER), channel capacity and interference reduction of system, different re-configurability techniques such as frequency hopping or diversity, polarization switching or diversity, and pattern beam smartness or diversity can be deployed.

3.3. Reconfiguration techniques at Millimeter waves

In this section, we review the most common techniques used at millimeter waves to realize reconfigurable antenna structures. As we have previously mentioned in Chapter 2, there are different aspects of reconfigurability such as, frequency, polarization, radiation-pattern and directivity. However, only one of these aspects, which is the pattern diversity is in the scope of this thesis. Therefore in this section, we focus our attention to some of the feasible techniques for radiation-pattern reconfiguration at the millimeter waves. Although we have named various techniques for pattern diversity in the previous chapter, we have to keep in mind that not all of them are easy to implement in the millimeter-

wave frequency band. For example, all the methods involving ferromagnetic and ferroelectric materials are not suitable for millimeter waves because of the high level of loss and also high power consumption [39]. On the other hand, it is evident that liquid crystals are not a good choice for millimeter waves because of the difficulty of implementation in this band [40]. Moreover, mechanical techniques are not usually used at the millimeter-wave band because of the lack of the ability of integration with the circuits [41]. In the following paragraphs we name some of the feasible techniques to be used for design and implementation of radiation-pattern reconfigurable antennas at the millimeter-wave frequency bands.

Using frequency as the variable factor for providing pattern diversity is one of the most effective techniques at the millimeter waves [42]. In these methods, the antenna is designed to operate at two or more frequency bands and in each of them a particular pattern is realized. Therefore, when the frequency of operation is changed, the radiation-pattern of the antenna is also changed. As examples of this method, we can point to leaky-wave antennas [43], where the angle of the antenna beam can be controlled by altering the frequency. In general, employing these methods provides the advantage of avoiding the active elements such as diodes and FETs, which are expensive, lossy and hard to implement at the millimeter waves. However, providing a completely reconfigurable pattern at one frequency is not possible. The other solution that is very useful at lower frequency bands is to use electrically controlled PIN diodes. With this approach, we can easily change the structure of the antenna and thus provide the desired pattern. But we have to keep in mind that this solution is much more expensive in millimeter waves and also the biasing network that is used to control the diodes may cause serious problems in the performance of the antenna. Nevertheless, with the recent advances in the on-cheap fabrication technology and SIW structures, high frequency PIN-diodes are attracting more attention and are being used in a variety of applications.

RF-MEMS (Radio Frequency Micro Electro-Mechanical Switches) are one of the most interesting choices at millimeter waves. This technology that was originally invented by IBM research laboratory [44] involves surface micromachining techniques and can be used for a wide range of frequencies. In fact, in this approach we can achieve RF functionality by moving sub-millimeter sized parts. Some factors such as integrated biasing solutions and compact packaging make them ideal for millimeter-wave applications. However, the difficult process of design and implementation is one of the limiting factors. If we want to avoid the difficulties of working with RF-MEMS and the lossy nature of PIN-diodes and keep the reconfigurable pattern for a single frequency, one of the easiest ways is to use antennas with multiple feeds. This method is usually used in literature to verify the performance of some novel prototypes [45]. But a

combination of this method along with SPDT (Single Pole Double Throw) switches can be used to implement reconfigurable-pattern antennas. In fact, we can design multiple feed lines with different beam angles and then switch the feeds and obtain the desired radiation-pattern. The SPDT switches are very easy to use and can be controlled with an external DC command circuit that doesn't affect the performance of the antenna [45].

3.4. Conclusion

Like other types of antennas at other frequency bands, different aspects of reconfigurability such as frequency, polarization, radiation-pattern and directivity can be used in millimeter-wave antennas. However, radiation-pattern reconfiguration is a crucial technique to be used at the millimeter waves to overcome some of the inherent limitations of this frequency band. To implement this technique in a cost-effective and easy way, it is evident that not all the techniques can be used and some special methods are required for millimeter waves. In this chapter, a number of special approaches have been named and briefly investigated such as frequency-dependent pattern diversity, high-frequency PIN-diodes, RF-MEMS and multiple-feed antennas with SPDT switches.

Chapter 4

Metamaterials

4.1. Introduction

Artificial periodic structures have been the area of debate in the last 20 years. There is a variety of names by which these materials are called such as DNG (Double Negative), EBG (Electromagnetic Bandgap), PBG (Photonic Bandgap) or FSS (Frequency Selective Surface). All of these structures are composed of periodically repeated sub-structures that are called unit-cells. The periodicity and dimensions of the unit-cells are different in each structure, for example in DNGs the periodicity is in order of $\lambda/10$ and in EBG and PBG structures is in the order of $\lambda/2$. Each of these periodic arrangements has its own application for example the EBG and PBG structures are capable of prohibiting the propagation of electromagnetic waves in a certain frequency range and thus providing a band-gap. DNGs on the other hand, provide a homogeneous medium which is capable of showing negative effective constitutive parameters such as permittivity (ε), permeability (μ) and refractive index (n) to the incident wavelength. Today, the term metamaterial is used for all the periodic structures with periodicity in the order of $\lambda/10$ regardless of the sign of the constitutive parameters. The metamaterial technology has enabled us to provide custom dielectrics with double negative, near-zero refractive-index, or high-

index double positive that do not exist in the nature or they are very hard to reach with conventional dielectrics.

4.2. History

One of the first efforts in the realization of artificial materials was the experiment of J. C. Bose, the British-Indian scientist, on twisted structures in 1898 [46]. K. F. Lindman, the Finnish physicist, was another pioneer in this field who worked on chiral media in 1914 [47]. Furthermore, in another experiment in 1948, W. E. Kock, the well-known American researcher in the field radar and electromagnetic waves, made an experiment on metal-lens antennas [48]. However, the first serious work on metamaterials was the famous paper of Victor Veselago, the Russian physicist in 1967 where he solved the Maxwell's equations for materials with simultaneously negative permittivity and permeability [49]. But, it took more than 30 years for the first metamaterial prototype to be implemented. First, in 1996 Pendry et al. presented an artificially electric plasma using thin wires to produce negative permittivity [50]. Only three years later in 1999, the same group realized the first artificially magnetic plasma using split-ring resonators (SRRs) [51]. Finally in 2001, Smith et al. implemented the first artificial double negative media using a combination of SRRs and thin wires [52]. Since then, various types of unit-cells with different characteristics have been designed and implemented for metamaterials and many different applications have used these structures including the famous concept of perfect lens and super lens [53]. In 2002, a non-resonant class of metamaterials called transmission-line metamaterials was developed by three research groups almost at the same time [54-56]. These research groups used the distributed model of conventional transmission lines, composed of series inductors and shunt capacitors, and turned into a left-handed media by switching the place of inductors and capacitors. Furthermore, they presented the concept of CRLH (Composite Right-Left Handed) media, which is capable of demonstrating both left-handed and right-handed behaviors by embedding inductors and capacitors in both shunt and series stubs.

Despite the very exciting features of metamaterials in changing the constitutive parameters of the mater, the resonant nature of metamaterials remains an unsolved problem which leads to narrow bandwidth and high loss for these structures and limits their application in many aspects. However in 2005, the gradient-index metamaterials were realized and defined a category of novel applications involving the bending of the electromagnetic waves [56]. Examples of these applications include invisibility cloak [55].

4.3 Characterization of Metamaterials

Regardless of the type or the application, the most important thing in the investigation of a metamaterial medium is to extract its effective constitutive parameters i.e. electric permittivity (ε), magnetic permeability (μ) and the refractive index (n). In periodic metamaterials, the unit-cells play the role of the atoms in conventional materials. Therefore, if the size of the unit-cell is much smaller than the wavelength, the periodic structure can be considered as a homogeneous medium and the macroscopic-scaled electromagnetic fields inside the medium and consequently the relative permittivity and permeability can be calculated by averaging the local fields [56]. These average parameters are similar to the parameters of Lorentz and Drude models, which are developed for static and quasi-static conditions [57]. These models can be used to explain the behaviour of a resonant system versus frequency simply by considering the system as a mass and spring mechanical equivalent. It is important to mention that these models can explain only the behavior of a single unit-cell and the real behaviour of the material is the sum of all resonant particles. To better clarify the behavior the Lorentz-based and Drude-based metamaterials, a brief description of each model is explained in the following subsections.

4.3.1 The Lorentz Model

We use the Lorentz model to explain the behavior of permittivity and permeability versus frequency. This model is in fact derived by describing the electron's motion as a driven damped harmonic oscillator [57]. Two famous special cases of this model are the Debye and Drude models. The main application of the Lorentz model is to describe the temporal response of a component of the polarization field to the same component of the electric field in one medium as below

$$\frac{d}{dt^2}P_i + \Gamma_L \frac{d}{dt}P_i + \omega_0^2 P_i = \varepsilon_0 \chi_L E_i \tag{4-1}$$

Where P_i is , Γ_L is, ω_0 is, χ_L is and E_i is .

Where the first term shows the acceleration of the charges, the second term is the damping factor, the third one is responsible for the resonance frequency and the right hand of the equation shows the coupling factor. Solving this equation for P_i, we can write

$$P_i(\omega) = \frac{\chi_L}{-\omega^2 + j\Gamma_L\omega + \omega_0^2}\varepsilon_0 E_i(\omega) \tag{4-2}$$

As we know the relation of the electric susceptibility, the electric field and the polarization, we can say

$$\chi_{e,Lorentz}(\omega) = \frac{P_i(\omega)}{\varepsilon_0 E_i(\omega)} = \frac{\chi_L}{-\omega^2 + j\Gamma_L\omega + \omega_0^2} \tag{4-3}$$

Where $\chi_{e,Lorentz}$ accounts for the electric susceptibility.

Having the electric susceptibility, we can easily find the permittivity as below

$$\varepsilon_{Lorentz}(\omega) = \varepsilon_0[1 + \chi_{e,Lorentz}] \tag{4-4}$$

There are two important special cases for the Lorentz model

(a) The Debye Model: when the acceleration term can be neglected, we will have

$$\Gamma_d \frac{d}{dt}P_i + \omega_0^2 P_i = \varepsilon_0 \chi_d E_i \tag{4-5}$$

$$\chi_{e,Debye}(\omega) = \frac{\chi_d}{j\Gamma_d\omega + \omega_0^2} \tag{4-6}$$

(b) The Drude Model: when the resonance term can be neglected, we will have

$$\frac{d^2}{dt^2}P_i + \Gamma_D \frac{d}{dt}P_i = \varepsilon_0 \chi_D E_i \tag{4-7}$$

$$\chi_{e,Drude}(\omega) = \frac{\chi_D}{-\omega^2 + j\Gamma_D\omega} \tag{4-8}$$

From the above equations, some important points can be inferred.

(1) In high frequencies, the permittivity goes to ε_0 in all the models.

(2) If the coupling coefficient is positive, only Lorentz and Drude models can produce negative permittivity.

(3) In the Lorentz model, because of its resonant nature, the negative permittivity occurs only in a small frequency range after the resonance.

(4) In the Drude model, the negative permittivity occurs when $\omega < \sqrt{\omega_p^2 - \Gamma_D^2}$ which is a wider frequency range than the Lorentz model.

According to Ziolkowski and Heyman, in a double negative (DNG) media, the refractive index *n* can be negative [56]. In this case for a low loss media we can write

$$\sqrt{\varepsilon} = \sqrt{\varepsilon_r\varepsilon_0 - j\varepsilon''} \approx -j(|\varepsilon_r\varepsilon_0|^{1/2} + j\frac{\varepsilon''}{2|\varepsilon_r\varepsilon_0|^{1/2}}) \tag{4-9}$$

$$\sqrt{\mu} = \sqrt{\mu_r \mu_0 - j\mu''} \approx -j(|\mu_r \mu_0|^{1/2} + j\frac{\mu''}{2|\mu_r \mu_0|^{1/2}}) \qquad (4\text{-}10)$$

For the wave number and the wave impedance we have

$$k = \omega\sqrt{\varepsilon}\sqrt{\mu} \approx -\frac{\omega}{c}|\varepsilon_r|^{1/2}|\mu_r|^{1/2}[1 + j\frac{1}{2}(\frac{\varepsilon''}{|\varepsilon_r|\varepsilon_0} + \frac{\mu''}{|\mu_r|\mu_0})] \qquad (4\text{-}11)$$

$$\eta = \frac{\sqrt{\mu}}{\sqrt{\varepsilon}} \approx \eta_0 \frac{|\mu_r|^{1/2}}{|\varepsilon_r|^{1/2}}[1 + j\frac{1}{2}(\frac{\mu''}{|\mu_r|\mu_0} - \frac{\varepsilon''}{|\varepsilon_r|\varepsilon_0})] \qquad (4\text{-}12)$$

and the refractive index is

$$n = \frac{kc}{\omega} = \sqrt{\frac{\varepsilon}{\varepsilon_0}}\sqrt{\frac{\mu}{\mu_0}} = -[(|\varepsilon_r||\mu_r| - \frac{\varepsilon''}{\varepsilon_0}\frac{\mu''}{\mu_0}) + j(\frac{\varepsilon''|\mu_r|}{\varepsilon_0} + \frac{\mu''|\varepsilon_r|}{\mu_0})]^{1/2} \qquad (4\text{-}13)$$

$$\approx -|\varepsilon_r|^{1/2}|\mu_r|^{1/2}[1 + j\frac{1}{2}(\frac{\varepsilon''}{|\varepsilon_r|\varepsilon_0} + \frac{\mu''}{|\mu_r|\mu_0})] \qquad (4\text{-}14)$$

According to the above equations, and because of the passive nature of the DNG medium, both of the real and imaginary parts the refractive index n must be negative.

4.3.2 Constitutive Parameters of bulk Metamaterials

The basic engineering parameters of metamaterials are the relative permittivity ε_r, and the relative permeability μ_r. Based on these two parameters, we can categorize metamaterials in three general groups: DPS (Double Positive), in which both ε_r and μ_r are positive, SNG (Single Negative), which has either negative ε_r or only μ_r but not both at the same time and finally, DNG (Double Negative), where ε_r and μ_r are both negative. Methods of characterization of metamaterials involve measurement of the transmission and reflection coefficients of a sample slab.

The majority of bulk metamaterials is based on two structures; here we describe both structures and explain the mechanism of producing negative permittivity and permeability for each one of them.

(a) Array of thin wires

Considering an array of parallel wires, it has been proved that this array has a high-pass behavior for an incoming wave with the electric field parallel to the wires [58]. It means that, for a structure shown in Fig. 3.1, below a cut-off frequency, we have the condition of total reflection.
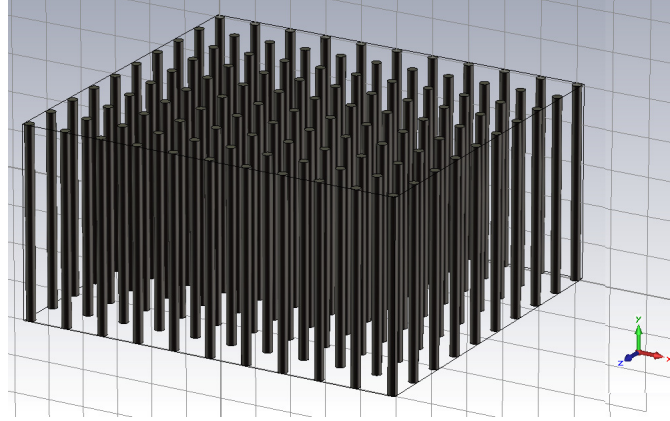
Fig. 4.1. Array of thin wires.

The total reflection in the wire array is similar to wave propagation in plasmas, thus if the spacing between the array's elements is very small compared to the wavelength, the thin wire array can be seen as a plasma. In this case we have

$$\varepsilon_z = \varepsilon_z^{'} - j\varepsilon_z^{"} = 1 - \frac{f_p^2}{f^2 + \dfrac{j\gamma f}{2\pi}}$$ (4-15)

Where f_p is plasma cutoff frequency, γ is the loss factor and f is the frequency. We should note that equation (4-15) is only for ε in the Z direction, and for X and Y directions, ε_r is always a positive number. The diagram shown in Fig. 4.2 is the simulated behavior of the real and imaginary parts of the relative permittivity based on the equation (4-15).
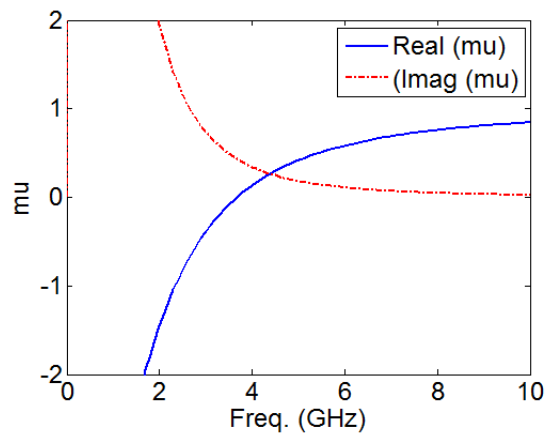
Fig. 4.2. The complex effective permittivity of the thin wire array.

(b) An array of Split-Ring Resonators (SRR)

A single SRR is in fact a small loop antenna, loaded by a capacitance, which works slightly above the resonance; therefore its magnetic field is out of phase with the magnetic field of the incident wave and therefore, the induced magnetic field is smaller than that of the incident field. This means that the relative permeability of such a media is negative.
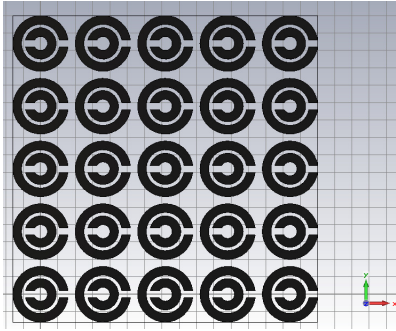
Fig. 4.3. Array of Split-ring resonators.

For SRRs, permeability is governed by equation (4-16) [59].

$$\mu = \mu' - j\mu'' = 1 - \frac{f_{mp}^2 - f_0^2}{f^2 - f_0^2 - \frac{j\gamma f}{2\pi}} \tag{4-16}$$

Where f_{mp} or magnetic plasma frequency (the frequency where $\mu_{eff}=0$), f_0 is the resonance frequency, and γ is the loss factor. The general behavior of magnetic permeability of SRRs is depicted in Fig. 4.4.
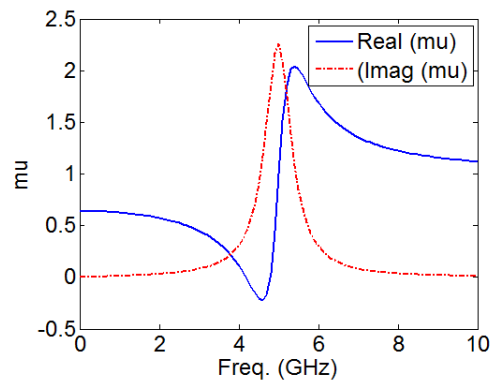
Fig. 4.4. The constitutive parameters of the split-ring resonator array.

The SRR is an anisotropic media. Therefore, only for a magnetic field perpendicular to the SRR, it possesses a negative permeability and for a magnetic vector parallel to the SRR, the permeability is positive. To have a nearly isotropic two-dimensional SRR-based metamaterial, we should have a 3D unit-cell with one SRR located in the XY and the other in the YZ plane. This general SRR-based metamaterial is described by a permeability tensor as follows [11,57]:

$$\overline{\mu} = \mu_0 \begin{bmatrix} \mu_{tr} & 0 \\ 0 & \mu_{lr} \end{bmatrix} \tag{4-17}$$

Where μ_{tr} is the relative permeability in transversal direction and μ_{lr} the relative permeability in the longitudinal direction.

Double Negative Metamaterials are fabricated by combination of thin wire arrays and SRR structures. Because the spacing between metamaterial's array elements is much smaller than a wavelength, DNG Metamaterials can be described by macroscopic parameters (ε and μ). The permittivity is a scalar number originated from thin wire array and the permeability is a uniaxial 2×2 tensor originated from the SRR structure.

We can write the wave equation for a waveguide filled with metamaterial as follows [57]

$$\nabla \times \overline{\mu}_r^{-1}(\nabla \times E) = k_0^2 \varepsilon_r E \tag{4-18}$$

$$k_0^2 = \omega^2 \mu_0 \varepsilon_0 \tag{4-19}$$

Solving this equation for a conventional DPS dielectric shows that there is a cut-off frequency above which we have propagation with the wave number of $\beta_y > 0$ (Forward Propagation). For isotropic ENG or MNG materials, there is no propagation. For isotropic DNG materials, we have propagation above a cut-off frequency with $\beta_y < 0$ (Backward Propagation). Finally, for the case of uniaxial MNG metamaterials, we have backward ($\beta_y > 0$) propagation below the cut-off frequency. It has to be mentioned that due to energy conservation law, every passive material should be dispersive [11,57]. Therefore, negative μ and ε exist only in a limited bandwidth.

4.3.3. Extraction of Metamaterial Constitutive Parameters

To be able to extract the effective constitutive parameters more accurately, a numerical retrieval method based on the S-parameters of the metamaterial is introduced in [60]. This method is much more accurate than the Lorentz and Drude models, but because of the complexity of the method, it's difficult to use it in the design of metamaterials, and is rather used in analysis of the metamaterial unit-cells. In the retrieval method explained in

[60], the S-parameters of the unit-cell i.e. S_{11} and S_{12} are considered as reflection and transmission coefficients. The relation between these parameters and the refractive index n and the impedance z can be found from the following equations.

$$S_{11} = \frac{R_{01}(1 - e^{j2nk_0d})}{1 - R_{01}^2 e^{j2nk_0d}} \tag{4-20}$$

$$S_{12} = \frac{(1 - R_{01}^2)e^{jnk_0d}}{1 - R_{01}^2 e^{j2nk_0d}} \tag{4-21}$$

Where $R_{01} = (z-1)/(z+1)$ and d is the distance that the incident wave travels inside the unit-cell. The impedance and refractive index can be simply obtained from the above equations

$$z = \pm\sqrt{\frac{(1 + S_{11})^2 - S_{12}^2}{(1 - S_{11})^2 - S_{12}^2}} \tag{4-22}$$

$$e^{jnk_0d} = Xk \pm j\sqrt{1 - X^2} \tag{4-23}$$

$$n = \frac{1}{k_0d}(\mathrm{Im}[\ln(e^{jnk_0d})] + 2m\pi - j\,\mathrm{Re}[\ln(e^{jnk_0d})]) \tag{4-24}$$

Where $X = 1/(2S_{12}(1 - S_{11}^2 + S_{12}^2))$. Since the metamaterial slab is a passive material, the real part of z and also imaginary part of n must be positive. The imaginary part of n can be uniquely determined, but to calculate the real part, we need to use the branch of the logarithm function. Various methods can be used to solve the equation and calculate n and z. In this thesis, we use a method based on Kramers-Kronig relationship explained in [61].

4.4. Common Unit-cell Geometries for bulk Metamaterials

After the successful realization of metamaterials by arrays of SRRs and thin wires, other types of unit-cells have been developed to enhance the bandwidth performance, facilitate the fabrication process or to miniaturize the unit-cell structure. As four particular examples of these efforts, we can name, broadside-coupled SRR (BC-SRR) [62], axially symmetric SRR [63], Omega-shaped resonators [64] and S-shaped unit-cells [65]. In the following paragraphs a brief explanation is given about each of these important unit-cells designs.

4.4.1. Broadside-Coupled SRR

The BC-SRR unit-cell is a creative structure that provides a very good miniaturization factor in a simple design. This structure consists of two split-rings printed on the top and bottom layer of the substrate as shown in Fig. 3.5.
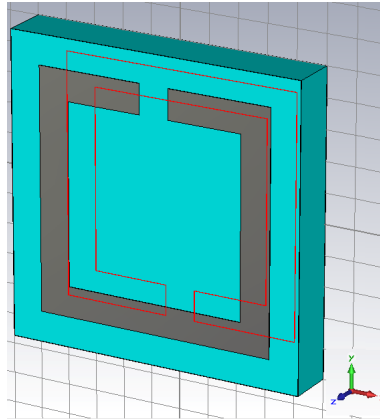
Fig. 4.5. Broadside-coupled SRR.

This unit-cell is excited by an electromagnetic wave incident from the edges. More comparison between the frequency response of the BC-SRR and conventional SRR is accomplished in [62,66].

4.4.2. Axially symmetric SRR

As shown in Fig. 3.6, this unit-cell has a symmetric structure in both elevation and azimuth planes that results in a very good field transmission and field symmetry [63].
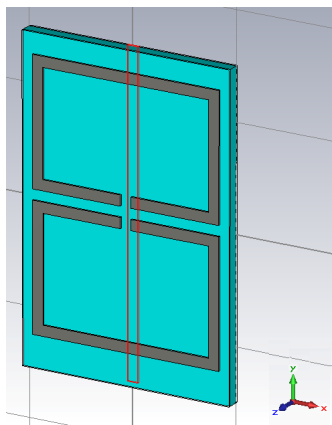
Fig. 4.6. Axially Symmetric SRR.

4.4.3. Omega-shaped Resonator

Omega resonator is another creative design, which is shown in Fig. 3.7. This structure in fact combines a line with a half-ring but suffers from an inherent unsymmetrical configuration that leads to bi-anisotropic behavior. To overcome this problem, two printed layers of the omega geometry are usually used at the top and bottom layer of the substrate.
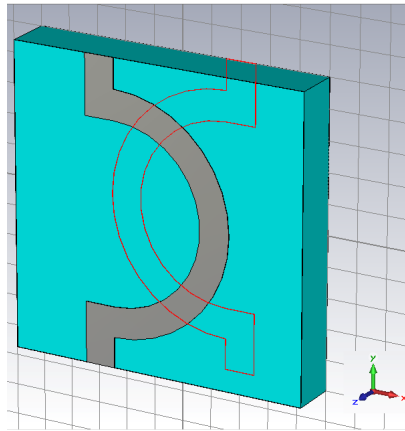
Fig. 4.7. Omega-shaped Resonator.

4.4.4. S-shaped Resonator

A schematic view of the S unit-cell geometry is shown in Fig. 3.8. This structure has the advantage of providing the resonance in permittivity and permeability in a single geometry. Another advantage of the S unit-cell is the relatively wide bandwidth.
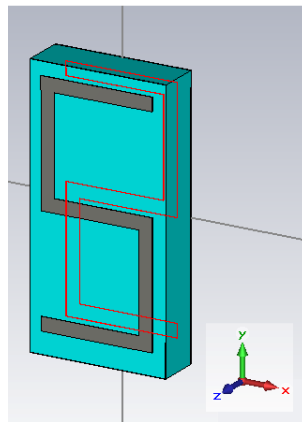
Fig. 4.8. S-shaped Resonator.

4.5. Metamaterial Applications

One of the most important applications of metamaterials, which is also one of the objectives of this thesis, is in the context of the antennas. In fact, various types of metamaterials can be used to enhance the performance of antennas in different ways or to realize reconfigurable and smart antenna elements. Some of the most important antenna applications of metamaterials are briefly explained in the following sections.

4.5.1. Gain Enhancement

The basic principle behind the gain enhancement methods involving metamaterials relies on the refractive index of the metamaterial medium placed in front or integrated within the structure of the antenna. This region can be a zero-index metamaterial (ZIM) or a near zero-index medium, which, according to the Snell's law of refraction, tends to focus the electromagnetic rays toward a normal vector. (Fig. 4.9)
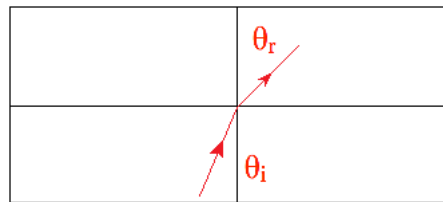
Fig. 4.9. The Snell's law of refraction.

The other possibility is to put a high-index medium in the way of electromagnetic rays that is in fact a lens and focus the antenna rays into a certain direction. Both of these methods have been proved to have a gain enhancement effect while because of the integrated nature of the metamaterial unit-cells, the size of the resulting structure is more compact compared to other methods of gain enhancement.

4.5.2. Beam-tilting

Tilting the antenna beam is one of the other interesting applications of metamaterials. In fact, according to our research in [67], we can use an integrated metamaterial section with a different refractive index compared to the antenna's substrate and provide a tilt angle for the antenna's beam. As shown in Fig. 4.10, we used a wide-band bowtie dipole antenna and then printed metamaterial unit-cells on the substrate (upper right corner of Fig. 4.10) to achieve the desired beam-tilting.
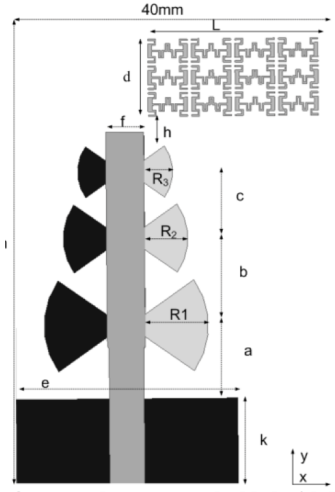
Fig. 4.10. Metamaterials for beam-tilting applications [67].

The advantage of this method is to possess a very low-profile structure and more importantly, eliminating the gain drop when the beam is tilted.

4.5.3. Mutual coupling Reduction

Although artificial structures such as EBGs are already used for mutual coupling reduction, metamaterials provide other types of solutions for this purpose. In fact, because of the frequency response of a metamaterial unit-cell to an incident wave, which produces a very low S_{21}, a metamaterial can be used to filter the surface waves between the elements and reduce the mutual coupling. Therefore, inserting an array or even a single metamaterial unit-cell with the size of $\lambda/10$ between the antenna elements has a significant effect on reducing the mutual coupling.

4.5.4. Phase Shifters, Couplers and Dividers

Phase shifters benefit from one of the special properties of left-handed metamaterials, which is to possess a phase constant inversely proportional to the frequency [68]. This unique characteristic leads to the realization of miniaturized phase shifters using metamaterials. Another advantage of metamaterial phase shifters is the possibility of the zero-degree phase shift resulted from combination a left-handed media (with negative phase shift) and a right-handed media (with positive phase shift). This can help us to avoid one-wavelength stubs and consequently, this reduces the size of the structure. The same principle as the phase shifters is true for the couplers and dividers.

Chapter 5

Stepped-Impedance Resonator (SIR) Technique, for miniaturization of Metamaterial Unit-cells

5.1. Introduction

As mentioned in the previous chapter, the size of a metamaterial unit-cell is in the order of $\lambda/10$, where λ is the wavelength of the corresponding electromagnetic wave in the free space. However, a variety of sizes between $\lambda/6$ and $\lambda/10$ have been used in the literature [69-71]. Normally when a special design is used to achieve a multiband or reconfigurable behavior, the size of the unit-cell is increased [72-74]. Nevertheless, for a metamaterial to be considered as a homogeneous medium, it is crucial to have small unit-cells compared to the wavelength and with smaller unit-cells, we can achieve more smooth performance in terms of the effective parameters. For this reason, various techniques of miniaturization have been applied to metamaterial unit-cells. For instance, Baena et al. have introduced spiral resonators as an example of a compact metamaterial unit-cell in [75]. Moreover, the BC-SRR is a highly miniaturized unit-cell compared to the conventional SRR [62]. As other examples of miniaturization techniques, we can point to the use of fractal and Greek-key structures [75,76]. All of the existing works on the size

reduction of metamaterial unit-cells use their own special geometries and to our knowledge, there is no method that can be generalized to all kinds of unit-cells.

In this chapter, we introduce a novel technique for miniaturization of metamaterial unit-cells, which is based on the application of stepped-impedance resonators. This method considers a metamaterial unit-cell as an assembly of several metallic segments and employs the concept of stepped-impedance resonators to reduce the size of each segment. In other words, our proposed technique makes some controlled modifications in the geometry of the unit-cell and therefore, can be combined with any other miniaturization technique [66,77]. It is important to mention that the method we introduce here, is optimized for rectangular-shaped unit-cells and the circular unit-cells are beyond the scope of this thesis. However, one particular case of a modified three-turn spiral is studied at the end of this chapter.

5.2. SIR Technique

Stepped-impedance resonators (SIRs) have been developed more than three decades ago [78]. Back then, the lumped-element resonators were widely used due to their compact size and ease of implementation. However, the main drawback of these resonators, which is their low Q-factor, was the motivation to introduce the stepped-impedance resonators as a new class of high-Q and compact resonators. Since then, SIR structures have been widely used in filters, duplexers and dividers [79]. The SIR configuration of a simple microstrip line is shown in Fig. 5.1, which is a three-section stub where the linewidth of the middle section is larger than the other sections and consequently, its characteristic impedance is lower.
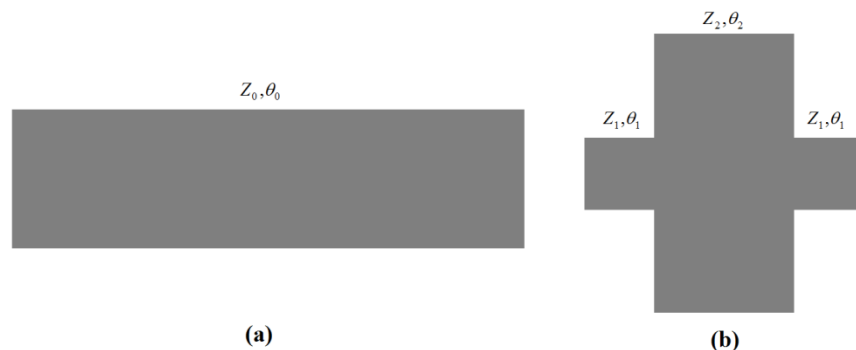
Fig. 5.1. A conventional microstrip line (a) and its equivalent SIR configuration (b).

By choosing the appropriate values for different lengths of the SIR configuration, we can prove that both of them have equal ABCD matrices. However, before getting in to

mathematical proof of this concept, it is important to mention that this transformation should effect on metamaterial unit-cell structures. The main difference between a microstrip line and a common unit-cell is that most of the unit-cells do not have a ground plane. Therefore in order to be able to define a characteristic impedance for a section of a unit-cell, one should consider another type of transmission line with the same impedance behavior as the microstrip line. A very good candidate for this transmission line is the paired strip line, which consists of two parallel lines one on the top and one on the bottom layer of a dielectric substrate [80]. This structure is especially ideal for metamaterial unit-cells because most of the times the same unit-cell is printed on both sides of the substrate. Fig. 5.2 shows a schematic view of the paired strip line.
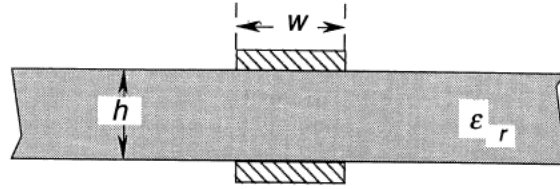
Fig. 5. 2. The Paired strip transmission line [80].

The characteristic impedance of a paired-strip transmission line is calculated in [80] which is

$$Z_0 = \begin{cases} \dfrac{\eta_0}{\sqrt{\varepsilon_r}} \{\dfrac{a}{b} + \dfrac{1}{\pi}\ln 4 + \dfrac{\varepsilon_r+1}{2\pi\varepsilon_r}\ln[\dfrac{\pi e(\frac{a}{b}+0.94)}{2}] + \dfrac{\varepsilon_r-1}{2\pi\varepsilon_r^2}\ln\dfrac{e\pi^2}{16}\}^{-1} & (a/b)>1 \\[4mm] \dfrac{\eta_0}{\pi\sqrt{\varepsilon_r}} \{\ln\dfrac{4b}{a} + \dfrac{1}{8}(\dfrac{a}{b})^2 - \dfrac{\varepsilon_r-1}{2(\varepsilon_r+1)}(\ln\dfrac{\pi}{2} + \dfrac{\ln\frac{4}{\pi}}{\varepsilon_r})\} & (a/b)<1 \end{cases} \tag{5-1}$$

Where $a=w/2$ (half of the strip width), $b=h/2$ (half of the substrate thickness), η0 is the impedance of the free space ($\approx 377\ \Omega$) and ε_r is the relative permittivity of the substrate. In order to use paired-strips to calculate the characteristic impedance of a section of a metamaterial unit-cell, we have to ensure that the behavior of its characteristic impedance is the same as a microstrip line, because all the assumptions that we are going to make are based on the fact that the impedance of the middle section is lower than the two other sections with a predictable impedance ratio. Fig. 5.3 compares the characteristic impedance of paired-strip to a microstrip line.
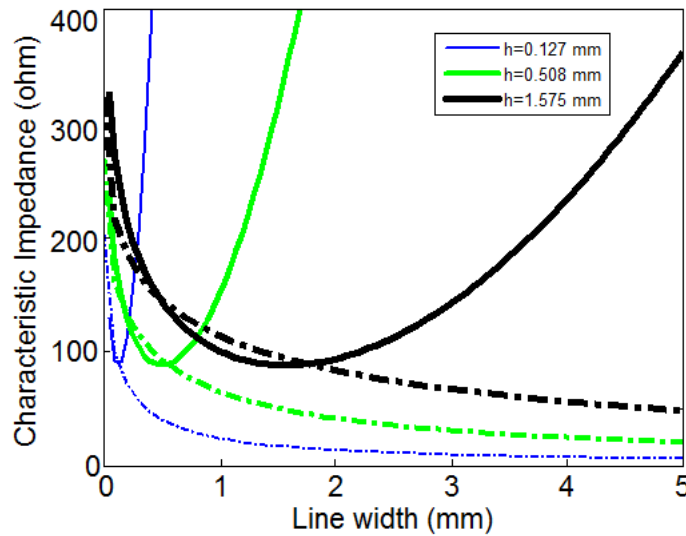
Fig. 5.3. The characteristic impedance of the paired-strip (solid curves) and microstrip transmission lines (dotted curves) versus the line width and substrate thickness.

In Fig. 5.3, two sets of curves are plotted for two different scenarios. The first scenario is a microstrip line with the line width shown on the horizontal axis (from 0 to 5 mm) on a substrate with the relative permittivity of 2.2. The characteristic impedance of this line is plotted in the form of dotted lines for three different substrate thicknesses (0.127, 0.508 and 1.575 mm). The second scenario is a paired-strip transmission line, which has the same conductor on the top of the substrate, but instead of the ground plane on the bottom, it has the exact same strip. The characteristic impedance of this transmission line is plotted in the form of solid lines for the same substrate with the same thicknesses.

Referring to Fig. 5.3, it is inferred that for a certain substrate thickness when the line width is below the intersection of the dotted and solid curves, both of the structures have almost identical characteristic impedances. In other words, when the substrate thickness is increased, we can expect the equality of the characteristic impedances to be extended to a higher limit on the horizontal axis. For example, when the substrate thickness is *h*=1.575 mm, the characteristic impedance is almost equal for both structures until the line width of 2 mm. In simple words, from Fig. 5.3, we can conclude that if a *thick enough* substrate and a *narrow enough* line is used, the two curves can be almost the same. The phrases "narrow enough" and "thick enough" can be quantified as shown in Eqn. (5-2). This equation shows the condition to be met for a paired-strip structure to be considered as a microstrip line.

$$\frac{h}{w} \leq 1 \qquad\qquad (5\text{-}2)$$

According to Eqn. (5-2), which is in fact extracted from Fig. 5.3, when the substrate thickness is increased, wider lines can be used.

The ABCD matrix of conventional the transmission line (shown in Fig 5.1. (a)) can be written as shown below, where θ_0 and Z_0 are the electrical length and characteristic impedance of the conventional line.

$$\begin{bmatrix} A & B \\ C & D \end{bmatrix} = \begin{bmatrix} \cos(\theta_0) & jZ_0\sin(\theta_0) \\ j\dfrac{1}{Z_0}\sin(\theta_0) & \cos(\theta_0) \end{bmatrix} \tag{5-3}$$

Referring to Fig. 5.1, the ABCD matrix of line (a) can be replaced with three matrices for the sections of the SIR configuration.

$$\begin{bmatrix} A & B \\ C & D \end{bmatrix} =$$
$$\begin{bmatrix} \cos(\theta_1) & jZ_0\sin(\theta_1) \\ j\dfrac{1}{Z_0}\sin(\theta_1) & \cos(\theta_1) \end{bmatrix} \begin{bmatrix} \cos(\theta_2) & jZ_0\sin(\theta_2) \\ j\dfrac{1}{Z_0}\sin(\theta_2) & \cos(\theta_2) \end{bmatrix} \begin{bmatrix} \cos(\theta_1) & jZ_0\sin(\theta_1) \\ j\dfrac{1}{Z_0}\sin(\theta_1) & \cos(\theta_1) \end{bmatrix} \tag{5-4}$$

The right sides of the Equations (5-3) and (5-4) should be equal; therefore, we can find the relation between θ, θ_1, and θ_2 as follow

$$\cos(\theta_2) = \frac{\cos(\theta)(1 - K^2\tan^2(\theta_1)) + \dfrac{1}{M}\sin(\theta)(1 + K^2)\tan(\theta_1)}{1 + K^2\tan^2(\theta_1)} \tag{5-5}$$

where M and K are defined as below

$$M = \frac{Z_1}{Z_0}, K = \frac{Z_1}{Z_2} \tag{5-6}$$

The miniaturization factor is determined by

$$\gamma = \frac{2\theta_1 + \theta_2}{\theta} \tag{5-7}$$

Since in metamaterials the dimensions of the unit-cells are in the order of $\lambda/10$, for finding an estimation about the miniaturization factor we can set $\theta = 2\pi/\lambda \times \lambda/10 = 2\pi/10$.

Fig. 5.4 shows the miniaturization factor for different values of K and M for $\theta = 2\pi/10$ and also for $K=6$ for the length of $\lambda/20$.
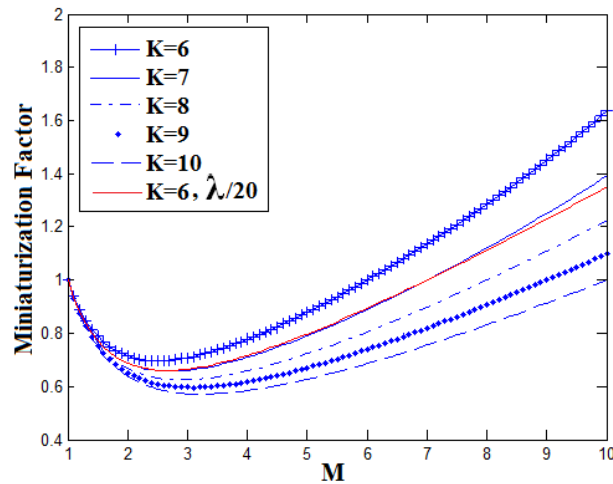
Fig. 5.4. Miniaturization factor for different values of M and K.

From Fig. 5.4, we can choose the optimum values of M and K for obtaining the best miniaturization factor.

5.3. Effect of the Higher Modes

In the previous section, we developed a model for a three-sectioned transmission line with different linewidths in each section. This model is based on the ABCD matrix of a transmission line with known length. However, it is important to mention that the extracted matrix model is based on the single-mode approximation [81]. In this section, we investigate the conditions that need to be met on the impedance ratio or in fact the parameter K for the single-mode approximation to be valid. The effect of the SIR technique on a rectangular structure is a stepped structure as shown in Fig. 5.5.
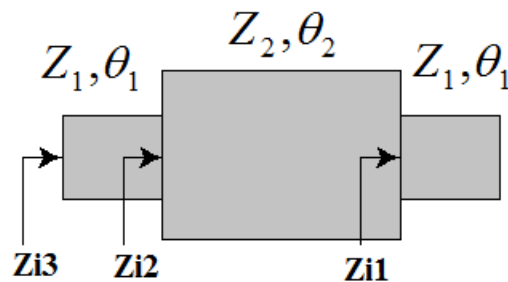
Fig. 5.5. The SIR configuration and its possible resonances.

In Fig. 5.5, we can find two resonances seen from Z_{i2} and Z_{i3}. Two different cases can be imagined for the three-sectioned stub, which are a short-circuited and an open-circuited stub, respectively. Each case is investigated by writing the resonance condition in the

following sections.

5.3.1. Short-circuited stub

When the stub shown in Fig. 5.5 ends to a short-circuit we have

$$Z_{i1} = jZ_1 \tan(\theta_1) \tag{5-8}$$

The first resonance occurs for Z_{i2} as below

$$Z_{i2} = Z_2 \frac{Z_{i1} + jZ_2 \tan(\theta_2)}{Z_2 + jZ_{i1} \tan(\theta_2)} \tag{5-9}$$

We can substitute Z_{i1} from Eqn. (5-8) in Eqn. (5-9) and we obtain

$$Z_{i2} = Z_2 \frac{[jZ_1 \tan(\theta_1)] + jZ_2 \tan(\theta_2)}{Z_2 + j[jZ_1 \tan(\theta_1)]\tan(\theta_2)} \tag{5-10}$$

or

$$Z_{i2} = Z_2 \frac{[jZ_1 \tan(\theta_1)] + jZ_2 \tan(\theta_2)}{Z_2 - Z_1 \tan(\theta_1) \tan(\theta_2)} \tag{5-11}$$

Setting the denominator equal to zero in Eqn. (5-11) gives us the first resonance condition as follow

$$\frac{Z_2}{Z_1} = \tan(\theta_1)\tan(\theta_2) \tag{5-12}$$

For the second resonance we have:

$$Z_{i3} = Z_1 \frac{Z_{i2} + jZ_1 \tan(\theta_1)}{Z_1 + jZ_{i2} \tan(\theta_1)} \tag{5-13}$$

Substituting Z_{i2} from Eqn. (5-11) gives us

$$Z_{i3} = Z_1 \frac{Z_1 \frac{j[Z_1 \tan(\theta_1) + Z_2 \tan(\theta_2)]}{Z_2 - Z_1 \tan(\theta_1)\tan(\theta_2)} + jZ_1 \tan(\theta_1)}{Z_1 + j \times Z_1 \frac{j[Z_1 \tan(\theta_1) + Z_2 \tan(\theta_2)]}{Z_2 - Z_1 \tan(\theta_1)\tan(\theta_2)} \times \tan(\theta_1)} \tag{5-14}$$

The second resonance condition can be calculated by setting the denominator of Eqn. (5-14) equal to zero as follow

$$Z_1 Z_2 - Z_1^2 \tan(\theta_1)\tan(\theta_2) = Z_1^2 \tan^2(\theta_1) + Z_1 Z_2 \tan(\theta_1)\tan(\theta_2) \tag{5-15}$$

The Eqn. (5-15) can be simplified as below

$$\frac{Z_2}{Z_1} = \frac{\tan(\theta_1)[\tan(\theta_1) + \tan(\theta_2)]}{1 - \tan(\theta_1)\tan(\theta_2)} \tag{5-16}$$

If we set the lengths equal in Eqn. (5-12) and (5-16) as mentioned in Eqn. (5-17)

$$\theta_1 = \theta_1 = \theta \tag{5-17}$$

then the first resonance condition becomes:

$$\frac{1}{K} = \frac{Z_2}{Z_1} = \tan^2(\theta) \tag{5-18}$$

If we consider the first resonance at f_0, the first higher mode occurs when $\theta_A = \pi - \theta$ and also when the frequency is increased to $2f_0$ which in turn leads to $\theta_B = 2\theta$ (because $\theta = 2\pi L/\lambda$ or $\theta = 2\pi f L/c$). Fig. 5.6 shows the normalized resonance frequency versus the impedance ratio $K = Z_1/Z_2$. This figure in fact plots the function $\theta = \tan^{-1}(\sqrt{1/K})$ versus the impedance ratio, which is shown in logarithmic order to include a very long range from 0.1 to 10.
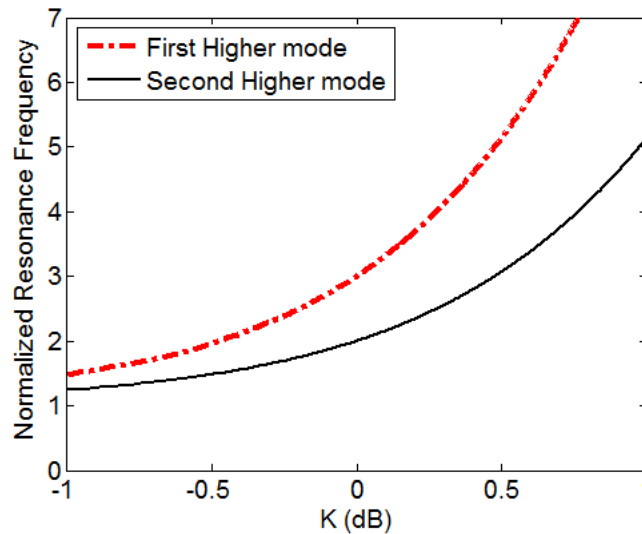
Fig. 5.6. The normalized resonance frequency versus impedance ratio for the first resonance when the stub is short-circuited.

From Fig. 5.6, we can infer that if $K>1$, the distance between the higher modes is more than in the scale of the normalized frequency, and the single-mode approximation is valid for the first resonance in the structure of the SIR configuration.
The same goes for the second resonance in Eqn. (5-16) where we can take all the lengths equal to θ and simplify the equation as below

$$\frac{1}{K} = \frac{Z_2}{Z_1} = \frac{2\tan^2(\theta)}{1 - \tan^2(\theta)} \qquad (5\text{-}19)$$

This time we need to plot the inverse function of Eqn. (5-19) that is

$$\theta = \tan^{-1}\sqrt{\frac{1}{2K+1}} \qquad (5\text{-}20)$$

Fig. 5.7 plots the two nearest higher modes to the first resonance (for $\theta_A=\pi-\theta$ and $\theta_B=2\theta$)
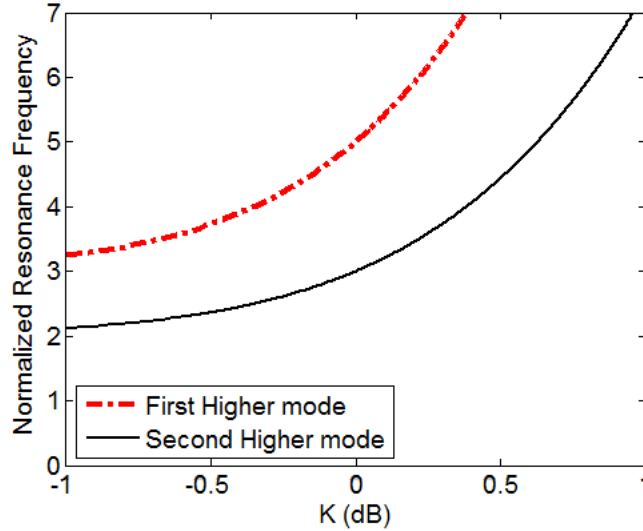
Fig. 5.7. The normalized resonance frequency versus impedance ratio for the second resonance when the stub is short-circuited.

Referring to Fig. 5.7, it is obvious that even a low K provides enough space between the higher modes of the second resonance when the stub is short-circuited.

5.3.2. Open-circuited stub

In this section, the second possible condition (Open-circuited) for a three-sectioned stub shown in Fig. 5.5 is studied. When the stub ends as an open circuit, for Z_{i1} we have

$$Z_{i1} = \frac{Z_1}{j\tan(\theta_1)} \qquad (5\text{-}21)$$

and for the first resonance at Z_{i2}

$$Z_{i2} = \frac{Z_2}{j}\frac{Z_1 - Z_2\tan(\theta_2)\tan(\theta_1)}{Z_2\tan(\theta_1) + Z_1\tan(\theta_2)} \qquad (5\text{-}22)$$

Setting the denominator equal to zero for $\theta_1=\theta_2=\theta$ leads to

$$(Z_1 + Z_2)\tan(\theta) = 0 \tag{5-23}$$

According to Eqn. (5-23), the condition for having the first resonance is $\tan(\theta)=0$ which is of course not acceptable. For the second resonance seen from Z_{i3}

$$Z_{i3} = \frac{Z_1}{j}\frac{Z_1 Z_2 - Z_2^2\tan(\theta_1)\tan(\theta_2) - Z_1 Z_2\tan^2(\theta_1) - Z_1^2\tan(\theta_1)\tan(\theta_2)}{2Z_1 Z_2\tan(\theta_1) + Z_1^2\tan(\theta_2) - Z_2^2\tan(\theta_2)\tan^2(\theta_1)} \tag{5-24}$$

Setting the denominator to zero with equal lengths yields

$$(2Z_1 Z_2 + Z_1^2)\tan(\theta) - Z_2^2\tan^3(\theta) = 0 \tag{5-25}$$

which in turn leads to

$$\theta = \tan^{-1}(\sqrt{2K + K^2}) \tag{5-26}$$

The first two modes near the main resonance are plotted in Fig. 5.8 as below.
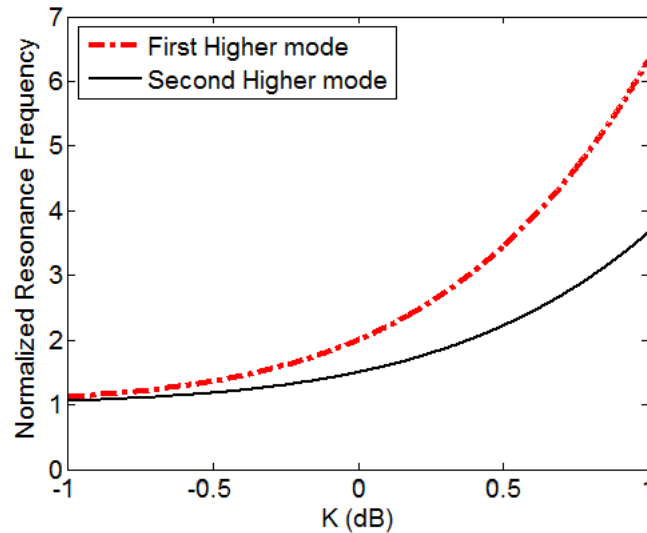
Fig. 5.8. The normalized resonance frequency versus impedance ratio for the second resonance when the stub is open-circuited.

According to Fig. 5.8, the parameter K should be greater than 0.5 in order to have the two modes far enough.

5.4. Case study: effect of the SIR technique on a rectangular BC-SRR and a circular spiral

To better understand the effect of the SIR technique, two special cases are studied in this section. The first one is the well-known BC-SRR unit-cell in the rectangular form, which has an inherent miniaturization factor by itself. This specific example clearly

demonstrates the ability of the SIR technique to be combined with another size reduction method. The second case that is investigated in this section is a simple circular split-ring. This particular case has been chosen to prove that the same algorithm can be useful for a circular-shaped geometry. However, more investigation is needed to cover all the aspects of the circular structures.

5.4.1. SIR effect on BC-SRR

Broadside-coupled split-ring resonators or BC-SRRs are proved to have a very good performance in terms of the size reduction compared to the conventional SRRs [62,66]. In this section, we apply the SIR miniaturization technique on a BC-SRR unit-cell and prove that the resulting structure, which is called SIR-BC-SRR, has an even better miniaturization factor. But, before showing the SIR-BC-SRR structure, a comparison between the performance of BC-SRR and SIR-SRR in terms of miniaturization factor is presented in Figs 5.9 and 5.10.

Fig. 5.9 (a)-(c) show a schematic view of a conventional SRR, a conventional BC-SRR and an SIR-SRR unit-cell. All the unit-cells are printed on a square-shaped substrate of Rogers RT/5880 with a relative permittivity of 2.2 and a thickness of 1.575 mm. The side of the substrate is 10 mm and thickness of the ring is 1mm.

(a)

(b)

(c)
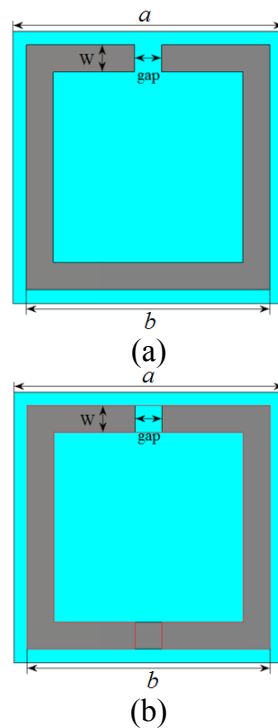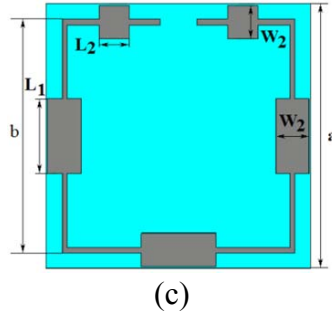
Fig. 5.9. A comparison between Conventional SRR (a), BC-SRR (b) and SIR-SRR (c) unit-cells. (dimensions in *mm*: *a*=10, *b*=9.70, *W*=0.88, *gap*=1.30, L_1=3.24, L_2=2, W_1=0.17, W_2=1.17)

All the three aforementioned structures are simulated with the PEC (Perfect Electric Conductor) and PMC (Perfect Magnetic Conductor) boundary conditions along the X and Y directions, respectively and two waveguide ports located in the Z direction. The extracted parameters for all the unit-cells are shown in Fig. 5.10.

(a)

(b)

(c)
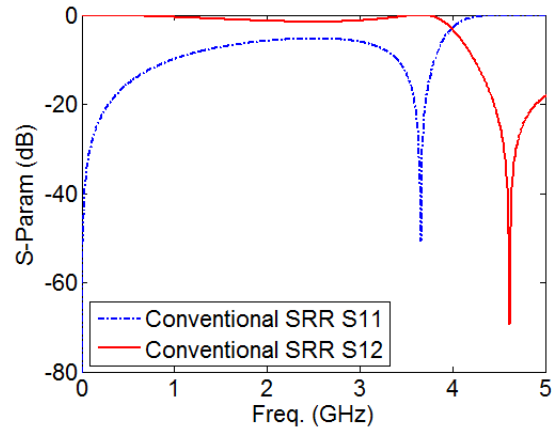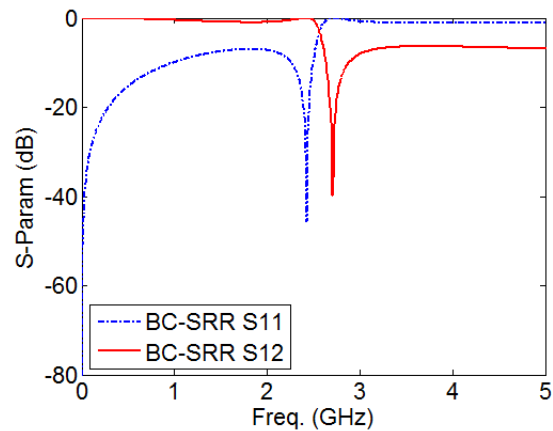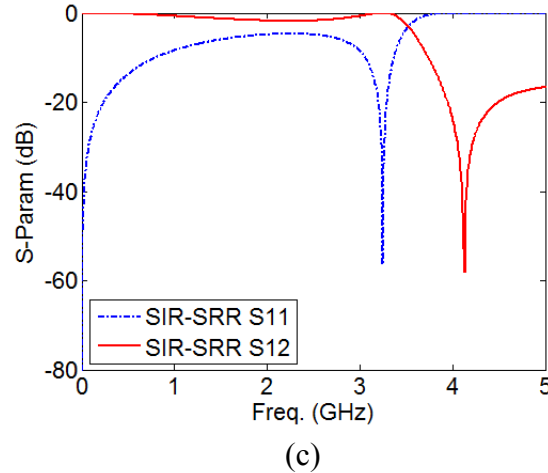
Fig. 5.10. The S-parameters of the conventional SRR (a), BC-SRR (b) and SIR-SRR (c).

According to Fig. 5.10, we can observe that in the case of conventional SRR, the first resonance of S_{11} is located at f_{SRR}=3.66 GHz, while for the BC-SRR, this resonance occurs at f_{BC-SRR}=2.42 GHz, which corresponds to a miniaturization factor of 0.66. On the other hand, for the SIR-SRR structure (Figs 5.9 (c) and 5.10 (c)), the first resonance is moved to $f_{SIR-SRR}$=3.25 GHz which means a miniaturization factor of 0.88. Of course at the first glance the BC-SRR might look superior to the SIR-SRR in terms of size reduction, but it has to be mentioned that the BC-SIR unit-cell is based on a very special technique, which only works for this type of unit-cell while the SIR-based unit-cell is based on a geometrical method that can be applied on any type of structure including the BC-SRR itself. In fact, if we apply the SIR technique on the BC-SRR structure, the resulting SIR-BC-SRR unit-cell, which is shown in Fig. 5.11, benefits from both methods at the same time, and can show a better size reduction factor. The results are shown in Fig. 5. 12.
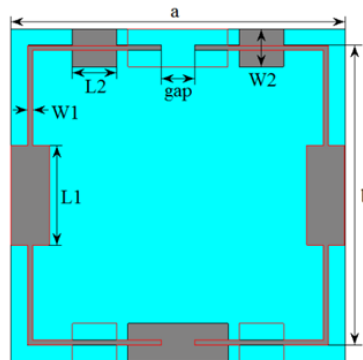
Fig. 5.11. The schematic view of the SIR-BC-SRR unit-cell.
(dimensions in *mm*: *a*=10, *b*=9.70, *W*=0.88, *gap*=1.30, L_1=3.24, L_2=2, W_1=0.17, W_2=1.17)
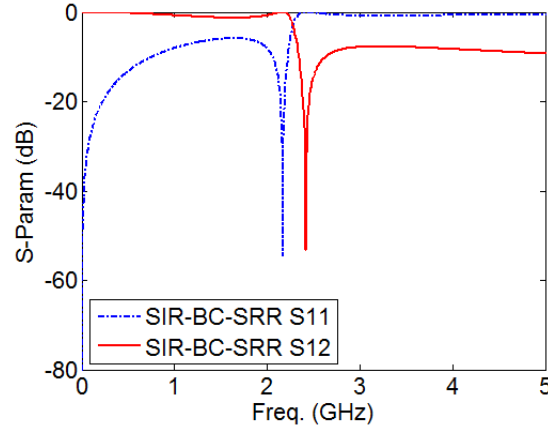
Fig. 5.12. The simulated S-parameters for SIR-BC-SRR unit-cell.

According to Fig. 5.12, the first resonance in the SIR-BC-SRR unit-cell occurs at $f_{SIR-BC-SRR}$=2.17 GHz, which means a miniaturization factor of 0.58, which is 13% better than the BC-SRR unit-cell.

5.4.2. SIR effect on a three-turn circular spiral

The SIR technique has the potential to be applied not only on rectangular structures, but also on circular structures. In fact, the general effect of this miniaturization method, which is increasing the line width in the middle section, can be extended to circular structures. In this section, the SIR method is applied on a three-turn circular spiral unit-cell and the resulting structure, which is called the crescent-shaped unit-cell, is investigated.

Fig. 5.13 shows the geometry of the proposed crescent-shaped unit-cell compared to a conventional three-turn circular spiral. Both structures are designed on a Rogers RT5880 substrate with the relative permittivity of ε_r=2.2 and a thickness of 1.575 mm. To maintain the unit-cell symmetry, the mirrored design of the structure compared to the Z axis is printed on the bottom side of the substrate. The dimensions of the structures in millimeter are *R=4.8*, *R'=3.3*, *R''=1.8*, *w=1*, R_1=4.8, R_2=3.6, R_3=1.8, L_1=10, L_2=3.6, L_3=4.6, a_1=1.5, b_1=0.3, b_2=0.3, b_3=0.3, d_1=0.1, d_2=1, d_3=1.5, d_4=0.5. These parameters are obtained considering our methodology and fabrication limitations and tuned using the HFSS optimization tools.

(a)   (b)
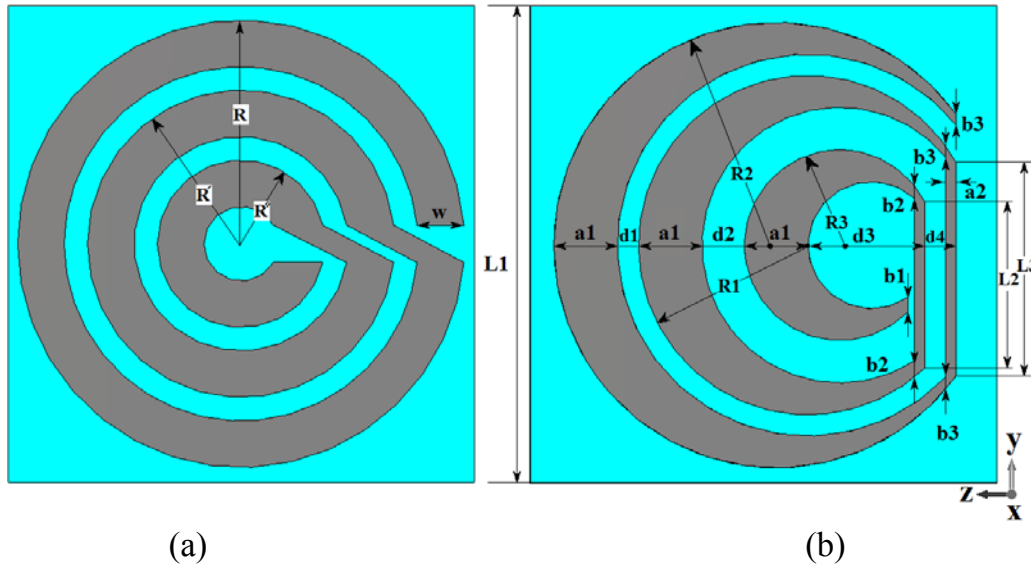
Fig. 5.13. Geometry of the conventional three-turn circular spiral resonator (a) compared to the proposed crescent-shaped unit-cell (b).

As seen in Fig. 5.13 (b), the new unit-cell linewidth is maximum in the middle and decreases at the edges, which leads to a crescent-shaped structure. As a result of this new geometry, we expect the overall induced current on the unit-cell and accordingly its equivalent capacitance to be increased. Therefore, because the resonance frequency is obtained using the equation $f=1/(2\pi\sqrt{LC})$, we can expect a lower resonance for this structure compared to the conventional spiral resonator. It is important to mention that the spiral unit-cell can be used as a high or near-zero refractive index if exploited slightly below or over the resonance, respectively. In the next section we prove that the crescent-shaped unit-cell can also serve both of these purposes providing a miniaturization factor compared to the spiral structure. Consequently, the presented design is a good candidate to be used in low-profile antenna applications such as gain enhancement and beam tilting [14], depending on the region of operation compared to the resonance frequency. To simulate the unit-cell, we used the HFSS software with PEC and PMC boundary conditions applied along XZ and YZ walls, respectively and two waveguide ports located along the Z direction. The parameters S_{11} and S_{12} for both conventional spiral and crescent-shaped unit-cell were calculated, as shown in Fig. 5.14.
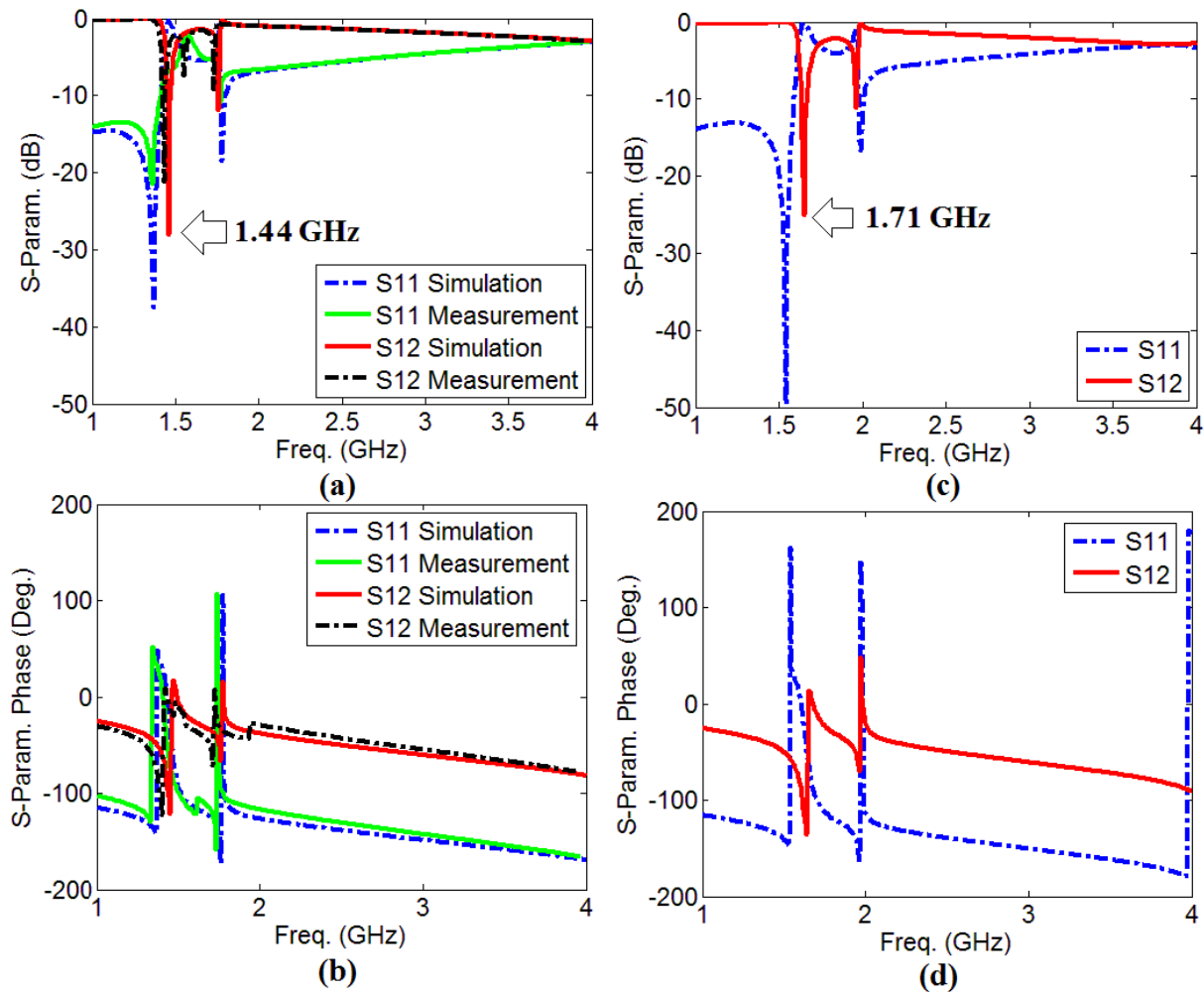
Fig. 5.14. The parameters S_{11} and S_{12} for crescent-shaped (a,b) and spiral unit-cell (c,d).

According to Fig. 5.14, we can see a downward shift with the ratio of 0.84 in the first resonance of S_{12} in the crescent-shaped structure compared to the spiral unit-cell. This means that the overall electrical size of the crescent-shaped structure is larger than the spiral while both of them have the same physical length. In other words, if we shrink down the crescent-shaped unit-cell by the ratio of 0.84 we will have equal electrical sizes but the crescent-shaped structure is physically smaller. Moreover, Fig. 5.14 also shows that the measurement results are in a very good agreement with the simulated data. It is important to mention that the proposed unit-cell is designed on a relatively low-permittivity substrate and if we increase the substrate dielectric constant, we can obtain more resonances as well as lower first resonance frequency. Table 1 shows the effect of this parameter.

Table 5.1. Effect of the substrate permittivity on the unit-cell.

Substrate permittivity	Number of resonances below 4 GHz	Frequency of first resonance in S_{12} (GHz)
2.2	2	1.71
6.15	2	1.12
10.2	3	0.89

To explain the reason behind this behavior from another point of view, we can refer to the current distribution of the spiral resonator presented in [8]. As shown in Fig. 5.15 (a), we can see that for the spiral, the current starts from zero at the outer gap and increases until reaches a maximum on the perimeter of the middle ring and then gradually goes to zero at the inner gap. As demonstrated in Fig. 5.15 (b), when the line width is increased, the maximum current on the middle ring increases significantly. The overall effect of this wider structure is to increase the current induced on the whole unit-cell and increase the equivalent capacitance of the crescent-shaped unit-cell compared to the conventional three-turn spiral.

(a)   (b)
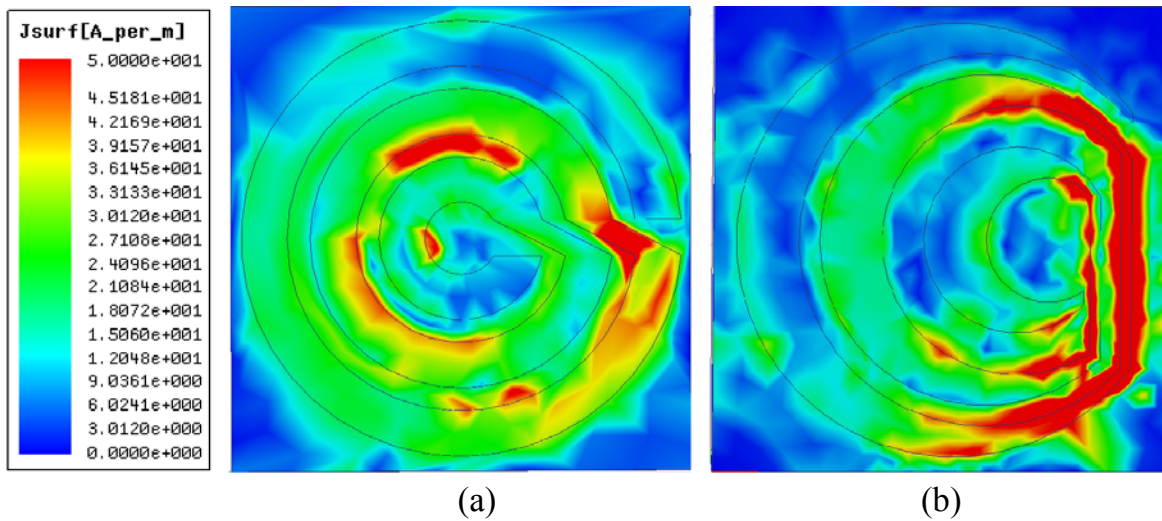
Fig. 5.15. The current distribution for spiral (a) and crescent-shaped unit-cell (b).

The S-parameters were used in a well-known algorithm to determine the effective constitutive parameters of the structure i.e. the permittivity and permeability [61]. In this algorithm, the parameters S_{11} and S_{12} are considered as the reflection and transmission coefficients and then, the impedance Z and refractive index n are calculated. Finally, from these results, the effective permittivity and permeability are calculated. Fig. 5.16 compares the extracted effective relative permittivity and permeability of the crescent-shaped unit-cell with the conventional spiral. According to these results, we can see the same downward frequency shift in the effective permittivity, and permeability and

refractive index of the unit-cell as expected. Additionally, the behavior of the extracted refractive index of the crescent-shaped unit-cell is the same as the conventional spiral resonator and provides a high-index and near-zero region before and after the resonance, respectively.
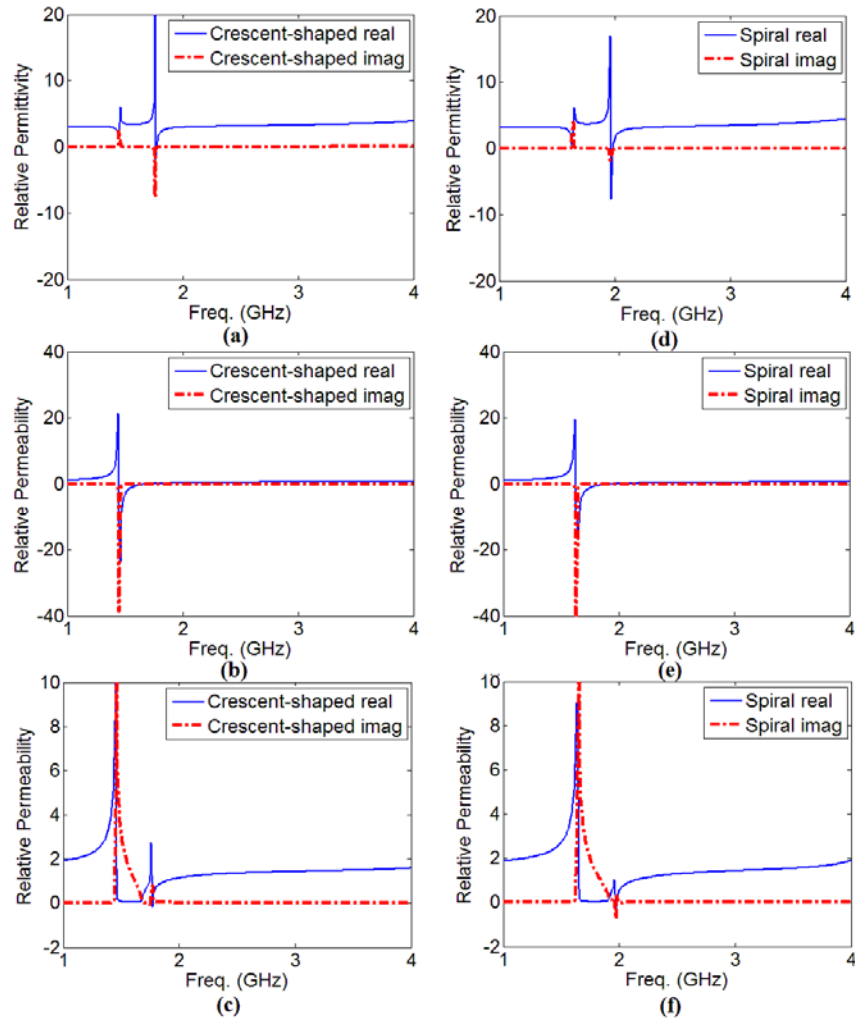
Fig. 5.16. The extracted constitutive parameters of the crescent-shaped (a,b,c) and spiral unit-cell (d,e,f).

As shown above, the imaginary part of the effective parameters is also depicted in Fig. 5.16 and we can see that the imaginary parameters are close to zero away from the resonance (as expected from the unit-cell behavior). To verify the simulation results, a 10×10 array of the unit-cell with the overall dimensions of 25×21 cm is fabricated as shown in Fig. 5.17.

Fig. 5.17. The fabricated crescent-shaped prototype.

5.5. Conclusion

In this chapter, the concept of stepped-impedance resonators has been used in the structure of metamaterial unit-cells and a novel miniaturization method called the SIR technique has been introduced. This method has been investigated for rectangular metamaterial unit-cells and its potentials and limitations have been studied. According to our research in this chapter, the most important advantage of this method is its geometrical nature that enables us to apply the SIR technique on any rectangular-shaped unit-cell and combine this method with other methods of size reduction. Of course this method is depended on the accuracy of fabrication technology and to avoid the effect of the higher modes, the thickness of the unit-cell substrate should be carefully selected. But in general, this method has been proved to present a very good solution for size reduction of metamaterial unit-cells which is a key factor in the homogeneous behavior of metamaterials. In the next chapter, this method will be used to design a novel unit-cell structure that plays an important role in the organization of this thesis and will be used in the structure of a novel reconfigurable antenna.

Chapter 6

The Unit-cell Structure

6.1. Introduction

Unit-cells are the building blocks of metamaterials with dimensions in the range of $\lambda/10$. From the first day of realization of metamaterials, many different types of unit-cells have been introduced [66,72,76]. However, there is still a need for design and implementation of reconfigurable unit-cells. Some reconfigurable unit-cells have been designed in [82]. In this chapter, first a novel reconfigurable unit-cell is presented which is capable of operating in three different modes. In each mode, the unit-cell shows a different refractive index. Then, the SIR technique is applied on the structure of the unit-cell to make it more compact. In fact, the final purpose of this unit-cell is to design a low-profile solution for providing radiation-pattern diversity in the current and future wireless LAN antenna systems. Hence the unit-cell is designed in two different frequency bands i.e. S-band and MMW band. It is noteworthy of mentioning that due to the frequency independent nature of both reconfiguration and miniaturization techniques, it is very easy to shift the operating frequency of the unit-cells as much as needed. Therefore, the same unit-cell is scaled to work at millimeter waves (60 GHz). However, because of some

practical issues, we do not provide measurement data for the reconfigurable unit-cell at 60 GHz. This unit-cell will be used for beam tilting applications for future millimeter-wave high data-rate indoor wireless networks.

6.2. The Unit-cell in S-band

The S-band (2-4 GHz) has been selected as the basic operating band of the unit-cell because of its application in the implementation of reconfigurable antennas for wireless LAN applications. The first step to fully comprehend the structure of our unit-cell is to have a look at the structure of the spiral resonator, which is introduced in [75]. Fig. 6.1(a) shows a schematic view of a two-turn spiral resonator. According to the work presented in [75], the current distribution of this unit-cell starts from zero at $\Phi=0$ at the outer ring and gradually ascends to reach a maximum on the conjunction of the two rings and then descends to reach zero again at the gap of the inner ring. This is clear that this distribution is different from a DSR configuration in Fig. 6.1 (b), where there is no connection between the rings and therefore the maximum of the current is much lower than the spiral.
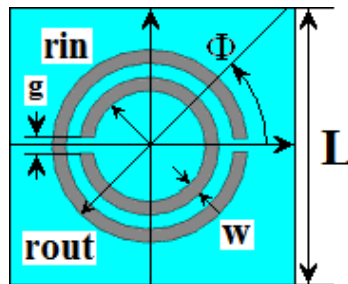
(a)
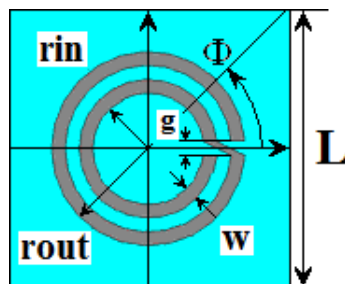
(b)

Fig. 6.1. A sample circular unit-cell in (a) DSR and (b) Spiral format (dimensions in mm: L=10, rout=4.5, rin=3.5, w=0.5, 5=0.5).

The larger maximum current in the spiral resonator leads to larger capacitance and therefore lower resonance frequency (because $f=1/(2\pi\sqrt{LC})$). Consequently, there is a downward frequency shift in the response of a spiral resonator compared to a conventional DSR, which can be treated as a miniaturization factor. Fig. 6.2 shows such a miniaturization factor for a special case of Figs. 6.1 (a) and (b).

(a)   (b)
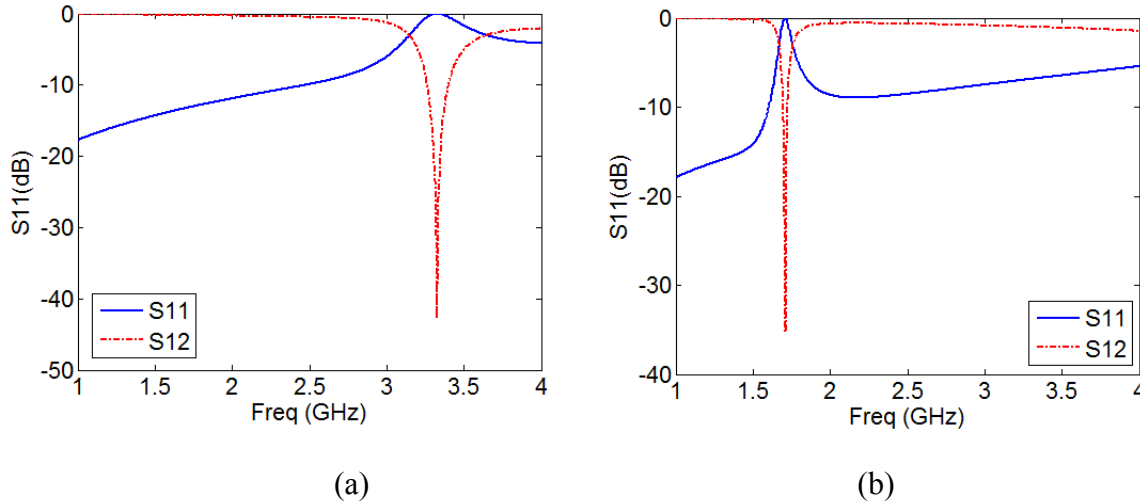
Fig. 6.2. The Simulated S-parameters of DSR (a) and Spiral (b) unit-cells.

This difference in the performance of the two unit-cells is used to design a reconfigurable unit-cell in the following section. The presented Spiral-DSR unit-cell is an ideal candidate for providing two different frequency responses while the overall topology is not changed by much.

6.2.1. The Reconfigurable Unit-cell

As previously mentioned, apart from the different current distribution and different frequency response of the spiral and DSR structures, the geometry of these two unit-cells are quite the same. In other words, we can convert these unit-cells to each other, only by controlling three PIN-diodes embedded in the structure of the unit-cell. The result of this design is that we can easily shift the frequency response of the unit-cell by switching the diodes.

6.2.1.1. Design

Fig. 6.3 shows a schematic view of unit-cell and the dimensions are listed in Table 6.1.
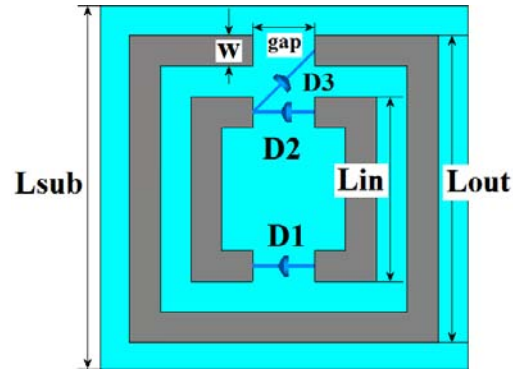
Fig. 6.3. The structure of the presented reconfigurable unit-cell.

Table. 6.1. The unit-cell dimensions.

Parameter	Lsub	Lout	Lin	gap	w	hsub
Value (mm)	11.02	9.70	6.67	1.5	1	1.575

As shown in Fig. 6.3, the unit-cell is composed of two concentric split-rings with three PIN-diodes D1, D2 and D3 embedded in the structure of the unit-cell. D1 and D3 have the same direction, which means they show the same state at the same time while the direction of D2 is in opposite of the other diodes. Having the so-called configuration for the diodes, we can infer that the unit-cell operates in three different configurations that are depicted in Fig. 6.4.
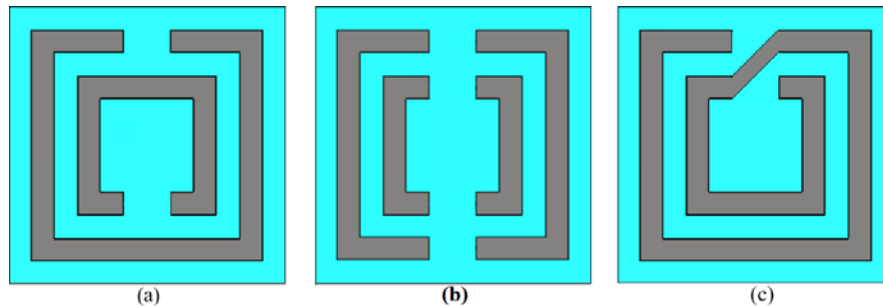
Fig. 6.4. Three configurations of the presented unit-cell.

According to Fig. 6.4, when D1 and D3 are ON, the unit-cell operates as a two-turn spiral (Fig. 6.4 c). When D2 is ON, the unit-cell is in fact a conventional DSR (double split-ring resonator in Fig. 6.4 a). The third state of the unit-cell is when all the diodes are OFF which is called quasi-DSR.

6.2.1.2. Simulation

In this section, the frequency response of the unit-cell is simulated using a standard procedure in the HFSS software. The unit-cell is placed inside a virtual waveguide with the PEC and PMC boundary conditions applied on the walls along Y and X directions, respectively while the two ports are placed along the Z direction. The simulated S_{11} and S_{12} (phase and magnitude) are used in the extraction algorithm to calculate the effective constitutive parameters i.e. the refractive index n, and the relative permittivity and permeability. We do the simulations in two steps, first when the diodes are in the ideal case and then when a lumped-element model is used for the diodes.

A) Simulation without the diodes
First for proof of the concept, the diodes are replaced by metallic strips with the dimensions of (1×1) mm in the ON state and empty space in the OFF state. The unit-cell is printed on both sides of a Rogers RT/Duroid 5880 substrate with the relative permittivity of ε_r=2.2 and the thickness of h=1.575 mm. The simulation results for each configuration of the unit-cell i.e. DSR, quasi-DSR and Spiral are shown in Figs 6.5, 6.6 and 6.7, respectively.
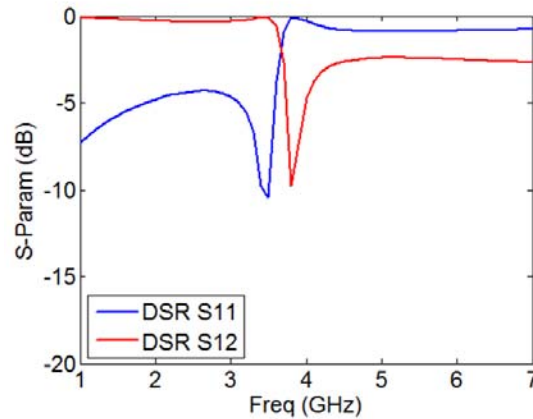
(a)
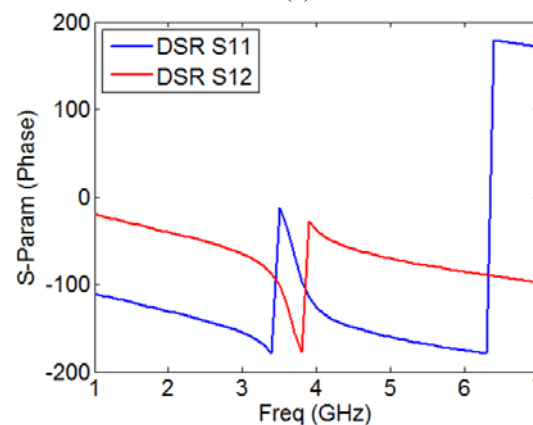
(b)
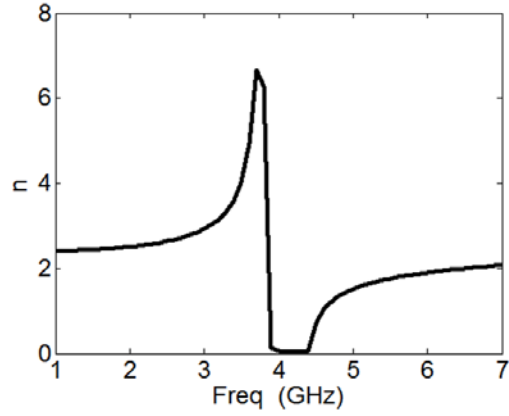
(c)

Fig. 6.5. The S-parameters magnitude (a), phase (b) and effective refractive index (c) for DSR.
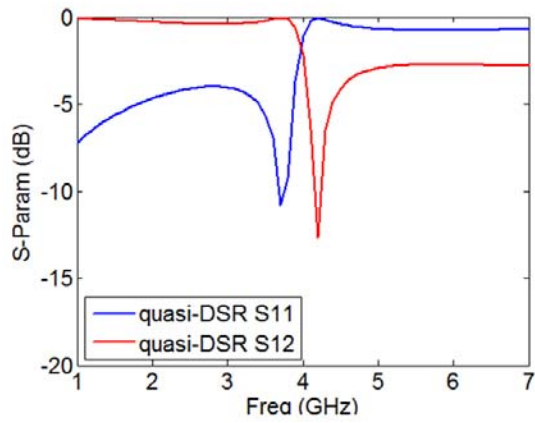
(a)
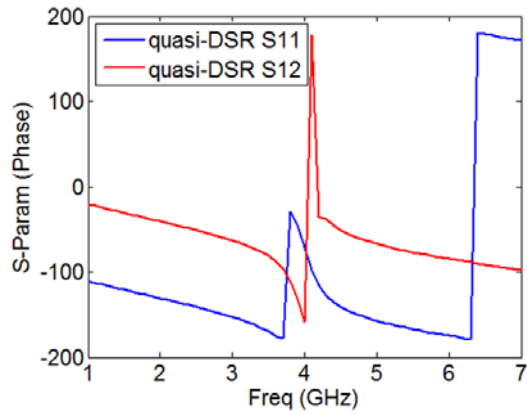
(b)
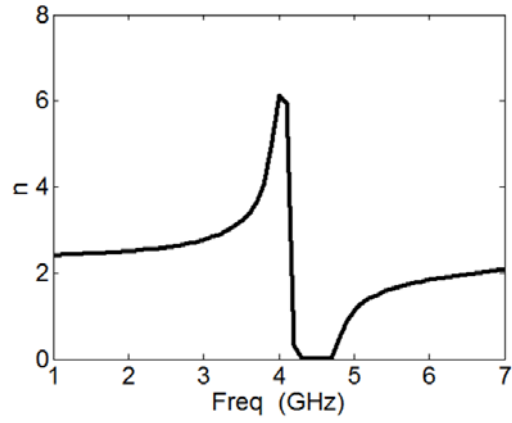
(c)

Fig. 6.6. The S-parameters magnitude (a), phase (b) and effective refractive index (c) for quasi-DSR.

(a)

(b)

(c)
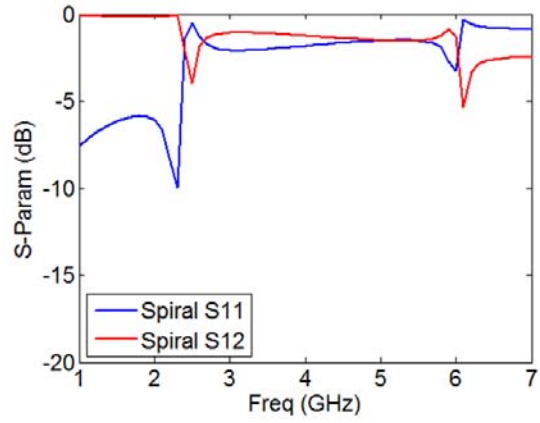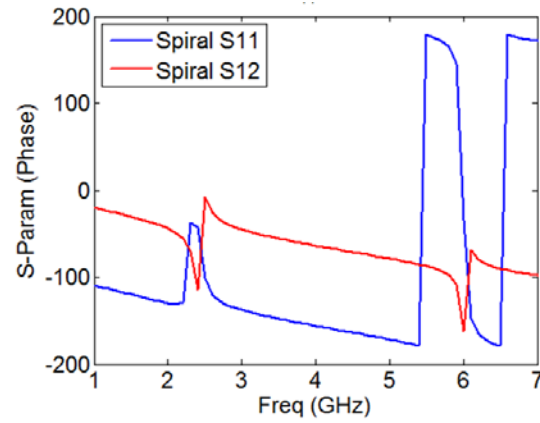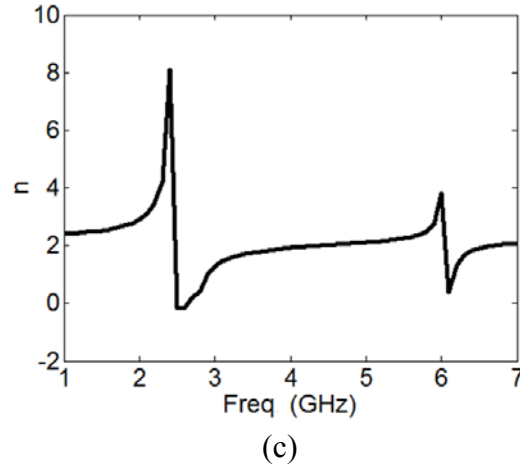
Fig. 6.7. The S-parameters magnitude (a), phase (b) and effective refractive index (c) for spiral.

According to the Figs 6.5 to 6.7, there is an abrupt change in the refractive index of the DSR unit-cell around 3.8 GHz followed by a near-zero region around 4.5 GHz. This behavior is shifted down in the spiral structure and it can be observed that the first resonance in the refractive index of the spiral occurs at 2.4 GHz and after a narrow-band near-zero region around 2.5 GHz, we have an effective refractive index of around 2 GHz up to the next resonance that happens around 6 GHz (which is out of our region of interest). As a consequence, there is a region around 2.4 GHz where a huge difference between the refractive index of the spiral and DSR structures is observed (spiral shows the higher n). Moreover, in another frequency range starting around 3.5 GHz up to 4.2 GHz, the refractive index of the DSR structure is higher than the spiral. It is important to mention that these differences will be used in the next chapter to switch the antenna beam in the desired direction and in the rest of this chapter we focus out study only on the implementation of the presented unit-cells.

As another conclusion of Figs 6.5 to 6.7, the refractive index of the unit-cell in the DSR and quasi-DSR case follow the same rule, and the only difference is a slight downward frequency shift in the DSR compared to the quasi-DSR structure. But, in the Spiral configuration, we have two resonances in the refractive index and the frequency shift is almost two times more than the two previous configurations. The distinction between the different responses of the unit-cell configurations can be attributed to the surface current induced on each configuration due to the incident wave.

<div align="center">(a)   (b)   (c)</div>
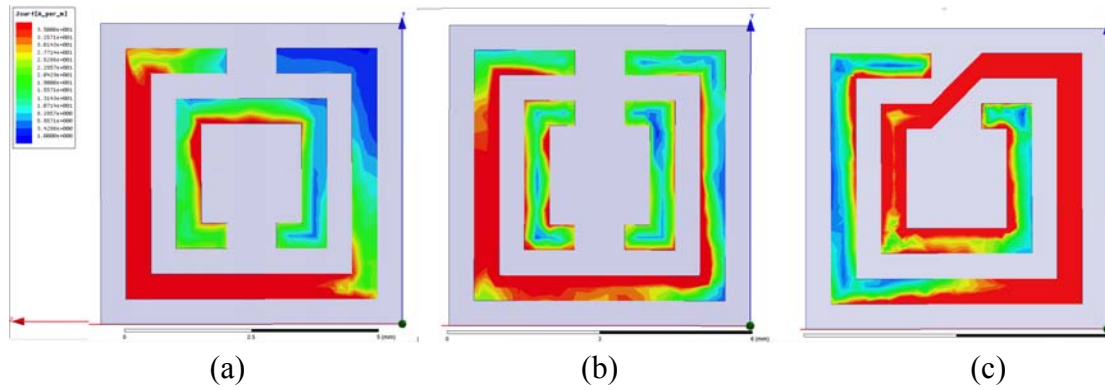
Fig. 6.8. The current distribution on different configurations of unit-cell at 3 GHz.

According to Fig. 6.8, at 3 GHz, in the DSR configuration, the maximum current is induced in the middle section of both inner and outer rings. This current is changed in the quasi-DSR configuration. However, the middle part of the outer ring still has the maximum current density but the inner ring is divided into two sections and each section has almost the same current density. Finally, in the Spiral configuration, the current density becomes much different from the other cases, because here, both of the rings are connected and we have just one conductor. In this case, the current density starts at zero in the inner gap, then increases until it reaches a maximum on the perimeter of the outer ring and then again becomes decreases until it reaches the other gap in the second ring.

In the following sections, we just concentrate our studies on the two cases of Spiral and DSR configurations, because the quasi-DSR shows a response similar to the DSR structure.

B) Simulation with the diodes

In order to investigate the real behavior of our structure, we need to use actual PIN-diodes. The GMP4201 diode has been selected for this application [25]. The lumped-element model shown in Fig. 6.9 has been used for this diode, with the parameters shown in Table 6.2.
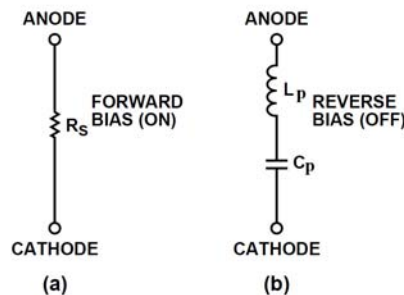
Fig. 6.9. The lumped-element model for the diodes [25].

Table 6.2. The parameters for the diode GMP4201.

Parameter	Rs	Lp	Cp
Value	1.8 Ω	0.05 nH	0.09 pF

In the real scenario, for switching the diodes, we need an actual external DC biasing network. To design this network, we need to ensure that the effect of the feeding lines on the unit-cell performance is minimum. As we already know, the proper way for a metamaterial unit-cell to be biased in the external field is that the lines of the unit-cell should be parallel to the electric field and the magnetic field should be perpendicular to the ring's planes. Therefore, in order to make the effect of the bias network minimum, we should ensure that the bias lines are not parallel with the unit-cell lines. A possible solution is show in Fig. 6.10. (The unit-cells on different sides of the substrate are connected to each other with vias as shown in Fig. 6.10.)
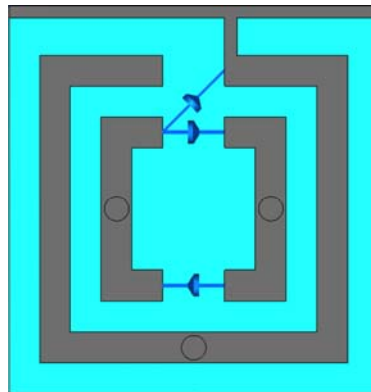
Fig. 6.10. The unit-cell with bias network.

Although we tried to design the bias circuit with the minimum effect on the unit-cell, it is evident that the proposed network is relatively complicated, and we expect the behavior of this unit-cell to be different from the ideal case. To better investigate the real scenario of using the diodes, new bias network is merged with the unit-cell, and the resulting structure is simulated as a new unit-cell. The S-parameters and the extracted effective refractive index of this unit-cell in different configurations are demonstrated in Figs 6.11 and 6.12.
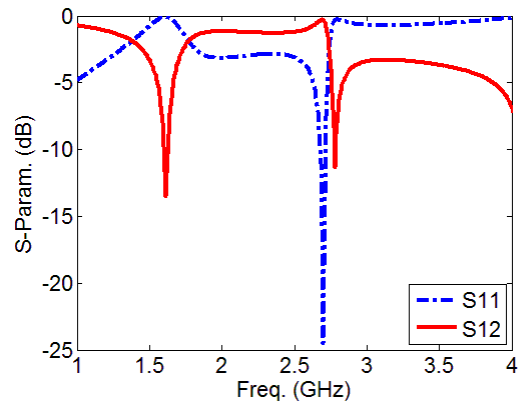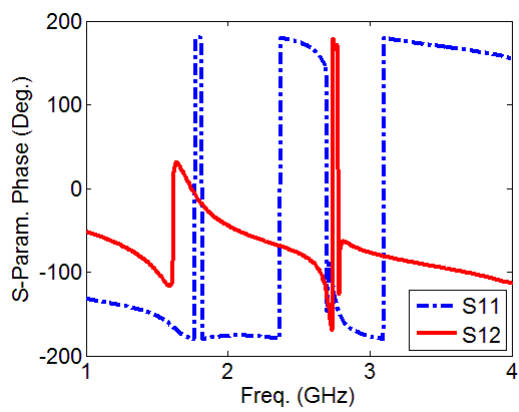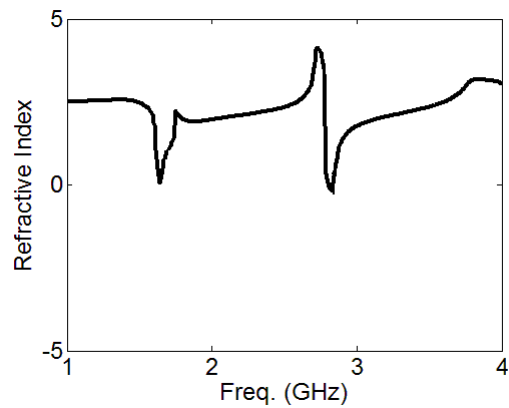
Fig. 6.11. The S-parameters magnitude (a), phase (b) and effective refractive index (c) for unit-cell in DSR configuration.
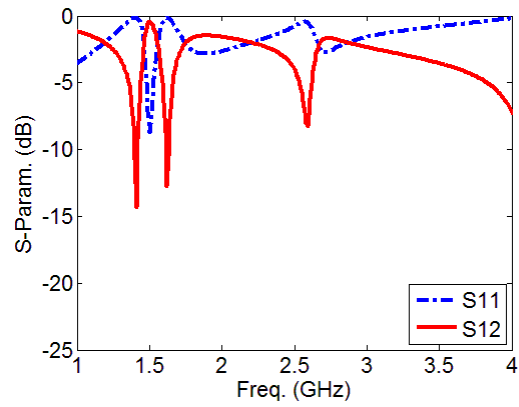
(a)
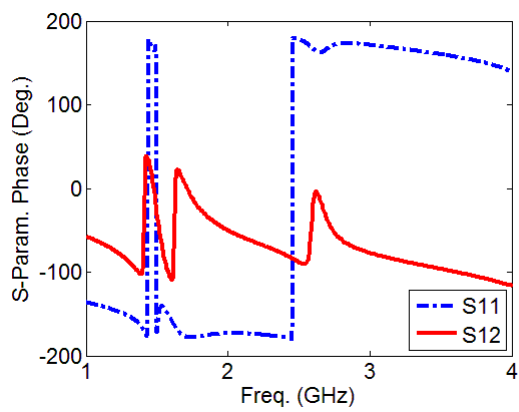
(b)
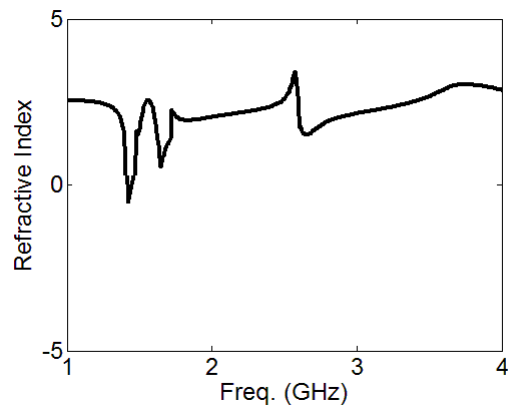
(c)

Fig. 6.12. The S-parameters magnitude (a), phase (b) and effective refractive index (c) for unit-cell in spiral configuration.

According to the results of Figs 6.11 and 6.12, the biasing circuit has an inevitable influence on the DSR and spiral configurations. The overall effect of this network is a downward frequency shift in the performance of both unit-cells, and as observed in Figs 6.11 (c) and 6.12 (c), the first resonances of DSR and spiral occur at 1.61 GHz and 1.41 GHz, respectively. This behavior can be easily attributed to the additional capacitance of the feed strips and also the inductance of the vias. The second resonance of the DSR is around 2.8 GHz, which produces an abrupt change starting from 2.6 GHz (where n is around 2) up to 2.75 GHz (where n is around 3.8), then falls down to a near-zero region around 2.85 GHz and the refractive index gradually increases and goes up to 2 around 3.4 GHz. For the spiral unit-cell, there is a resonance with the exact same behavior but shifted around 0.6 GHz toward lower frequencies. As a consequence, at the frequency range of 2.8 to 3.2 GHz, the spiral provides a higher refractive index compared to the DSR structure. In simple words in this region n_{spiral}-$n_{DSR} \approx 1.3$. To summarize our investigations on the presented unit-cell and DC bias network, it has to be emphasized that we can still use the structure to provide the desired difference in the refractive index by switching the diodes.

6.2.1.3. Experiment

A) Experiment without the diodes

Various methods have been used to measure the S-parameters of metamaterial unit-cells. These methods can be categorized into three groups: measurement methods involving a single unit-cell, waveguide methods and finally, the free space measurement (FSM) method that uses a large prototype of unit-cells placed between two standard horn antennas. This method is suitable for wideband applications and is used in this thesis. Single unit-cell methods are the easiest way to measure the metamaterial S-parameters. However, these methods cannot be considered as accurate methods, because to achieve an accurate approximation for the effective parameters, at least 5 unit-cells are needed. In the waveguide method, the unit-cell is placed in to a waveguide the same as the simulation. This method is accurate but expensive and also the unit-cell should be tightly fit to the waveguide. In the FSM method, an array of the unit-cell is placed between two horn antennas and the S-parameters are measured using a network analyzer. This method is widely used for measurement of the S-parameters of metamaterial structures due to its accurate, wideband and non-expensive nature. In this thesis, to validate the simulation results, a 3D array of the unit-cell is fabricated in each of its possible configurations i.e. DSR and spiral. More details on the measurement method is provided in chapter 8. Fig. 6.13 shows the picture of the fabricated single element and array for DSR and spiral unit-cells.
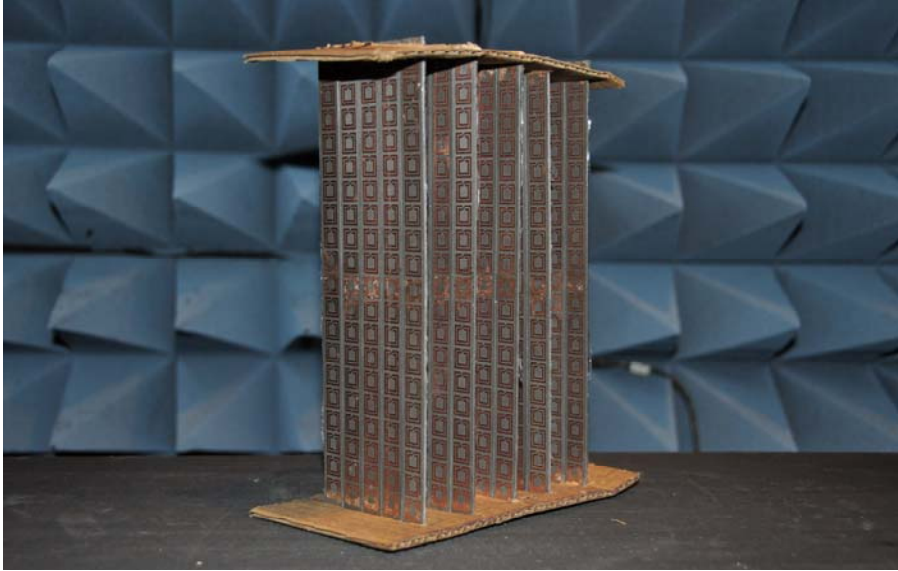
(a)
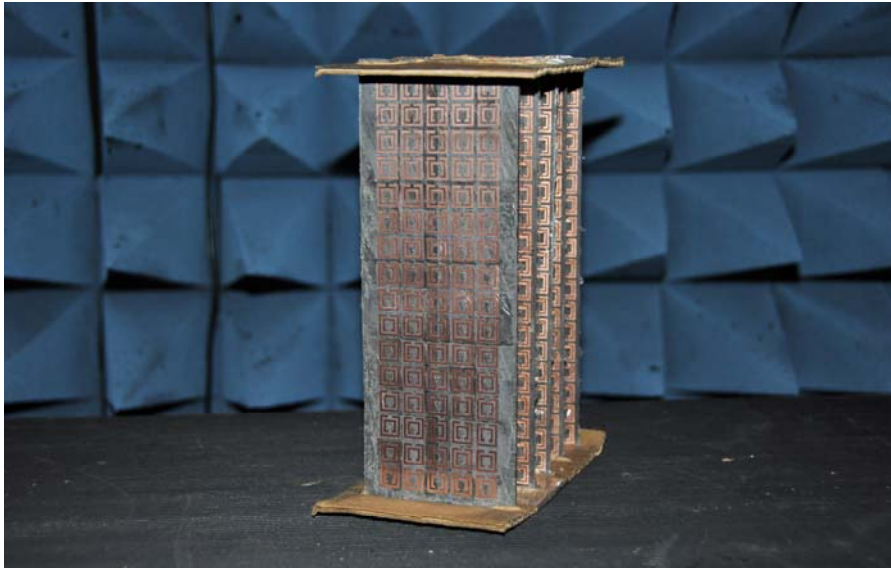
(b)

(c)   (d)

Fig. 6.13. The fabricated prototype for measurement of S-parameters.

The measurement results are shown in Fig. 6.14 (a), (b) and (c), respectively.

(a)

(b)

(c)

(d)
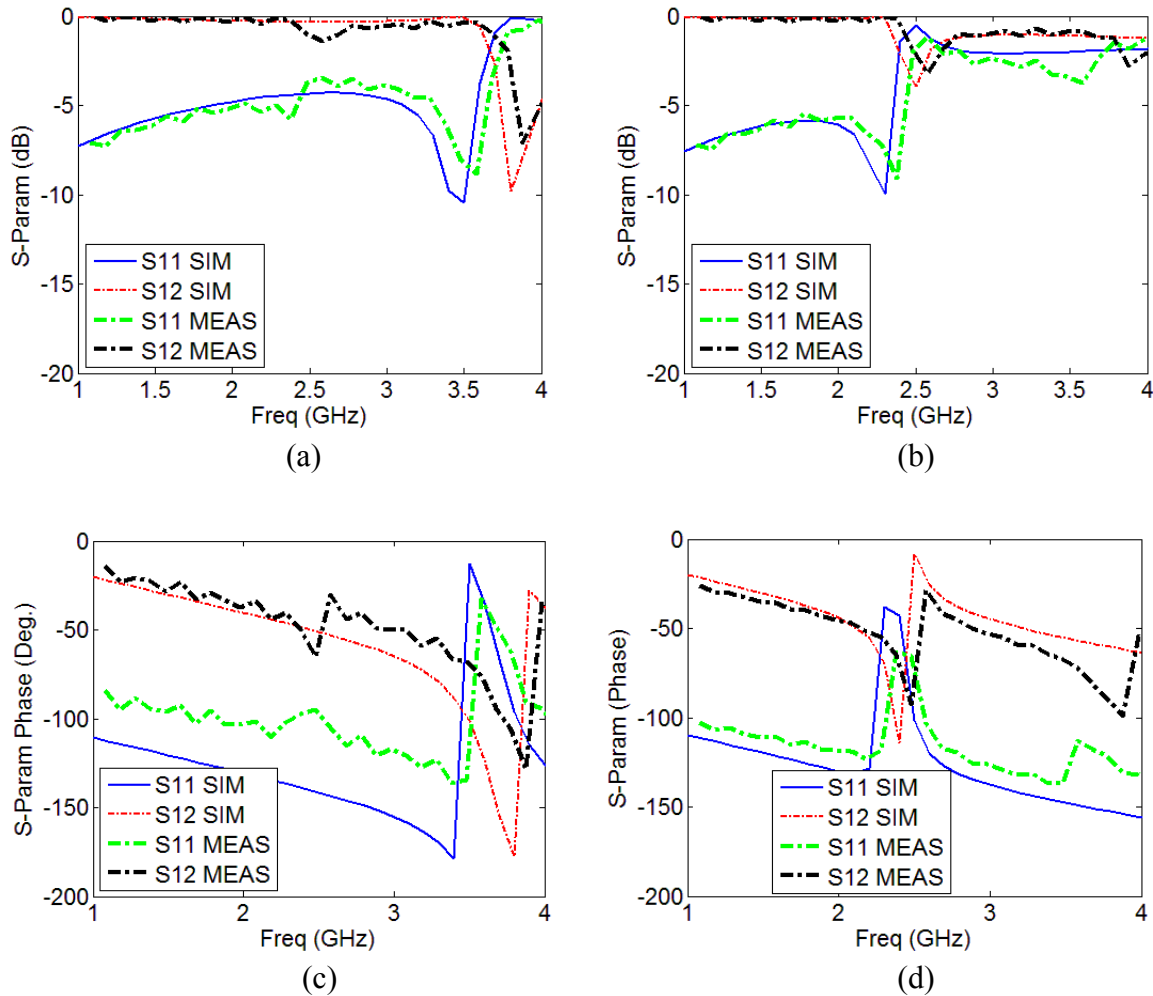
Fig. 6.14. The Measurement Results.

According to the results, there is a very good agreement between simulation and experiment in both spiral and DSR configurations. As a reason for this accuracy, we can mention the three dimensional structure with numerous unit-cells that provides a smooth effective medium. The other important factor is the special lens structure that we used in the FSM method which provides a very effective way of measuring the S-parameters.

B) Experiment with diodes

To measure the unit-cell parameters with the diodes, a 3D (5×5×4) array of the unit-cells is fabricated as shown in Fig. 6.15.
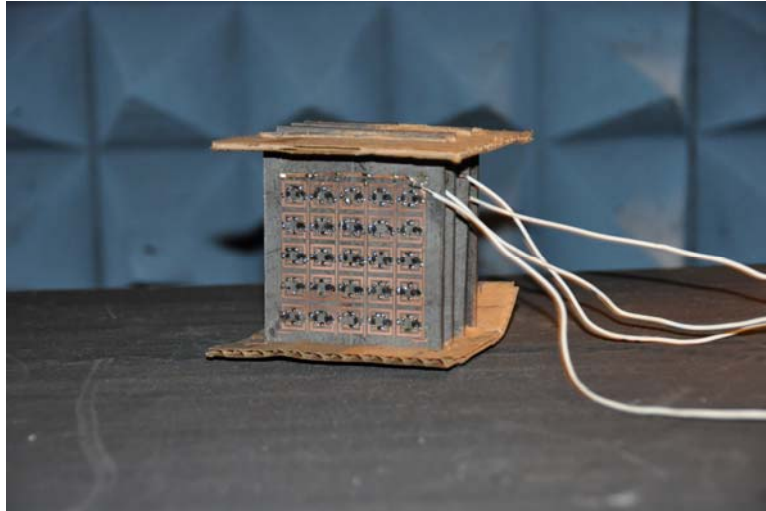
Fig. 6.15. The fabricated reconfigurable unit-cell array.

It is important to mention that we reduced the number of the unit-cells (and accordingly the size of the prototype) so a reduced number of diodes could be used. We used the free-space method as well as a dielectric lens structure to assure that the beam waist from the horn antenna is correctly concentrated on the prototype. The measurement results in each configuration of the unit-cell are plotted in Fig. 6.16. The slight mismatch between the simulation and measurement can be attributed to the fact that the number of unit-cells are limited (obviously because of practical limitations) and also because of the diodes. In fact, some of the diodes might not work well and affect the structure in a random complicated way, and there is no practical way to avoid that. Nevertheless, the overall performance of the measurement method is acceptable and the measurement results show a good agreement with the simulation.
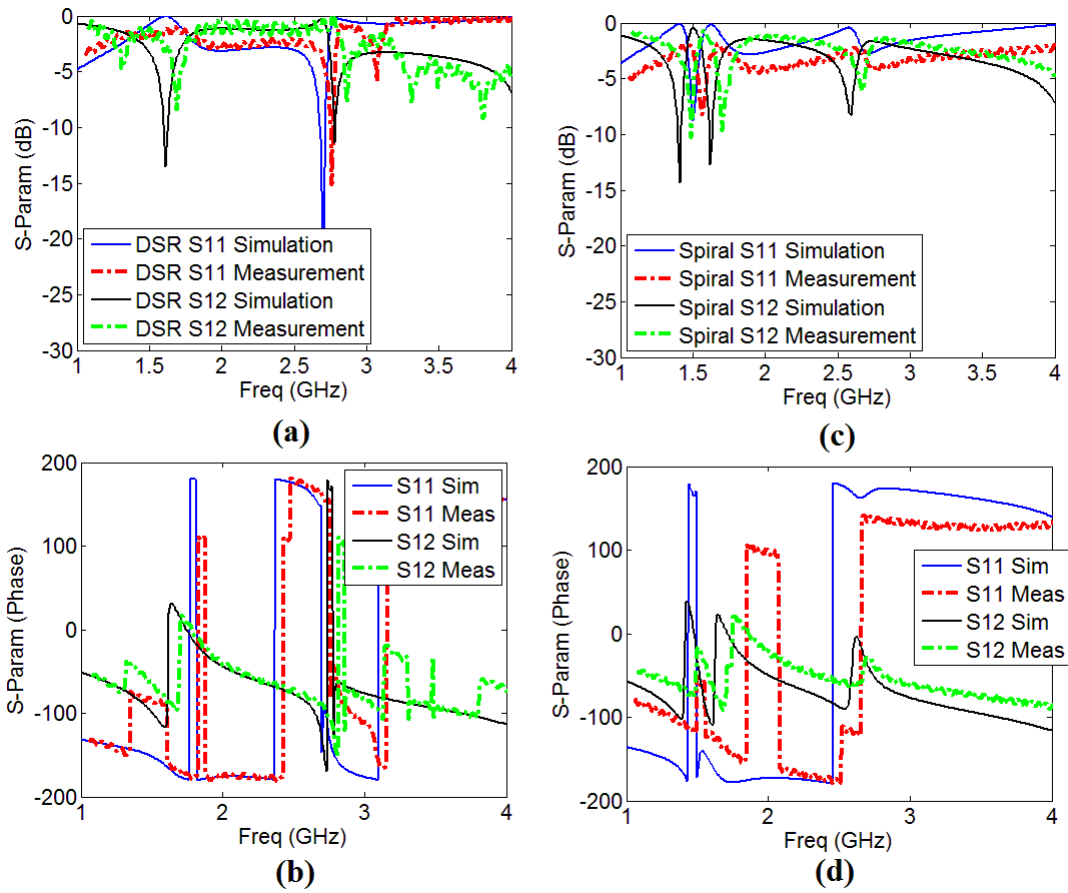
Fig. 6.16. Measured parameters of the reconfigurable unit-cells in DSR (a,b) and Spiral (c,d) configurations.

6.2.2. SIR-based Unit-cells

In this section, we study the SIR transformation effect on each of the unit-cells presented in the previous section. The purpose of the SIR technique is to reduce the size of the unit-cell and therefore, we expect a downward frequency shift in the unit-cell response when the method is applied while maintaining the overall cell size. It is important to mention that in this work only the non-reconfigurable SIR structures is realized at the S-band. The main objective here is the size reduction. In other words, we put more SIR unit-cells in the same physical length compared to regular unit-cells. This can help us provide a metamaterial medium with more uniform structure and consequently better results in terms of antenna radiation pattern as will be shown in the next chapter.

6.2.2.1. Design

To apply the SIR miniaturization technique, we refer to Fig. 5.4 from the previous chapter. For more convenience, the same picture is repeated as below.
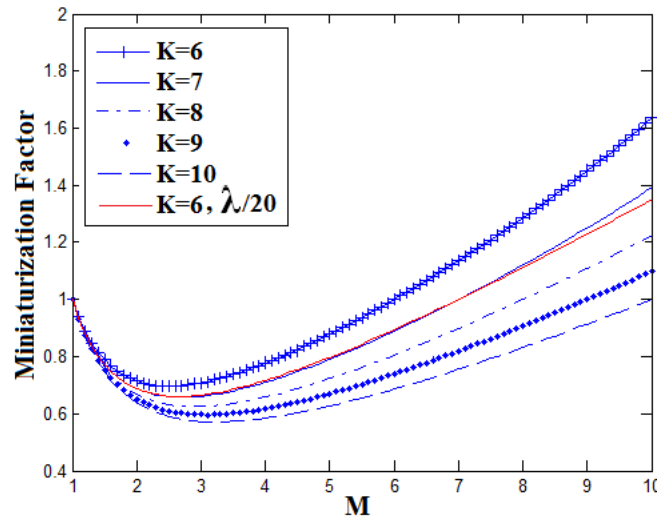
Fig. 6.17. SIR design curves.

According to Fig. 6.17, there is an optimum value for the parameter *M,* which is in fact the ratio of the original to the transformed linewidth. For the parameter *K* (the ratio between the wider section to the narrow part), there is no theoretical limit and we obtain better miniaturization factor by increasing *K.* However in reality, we cannot increase *K* as much as we want, because the geometry of the structure falls apart. On the other hand, the fabrication technology limits us to the maximum accuracy of 6 mils or 0.15 mm, therefore, *K=6* and *M=7* are determined to be the best parameters that we can reach.

Fig. 6.18 shows the effect of the SIR transform on different configurations of the unit-cell.
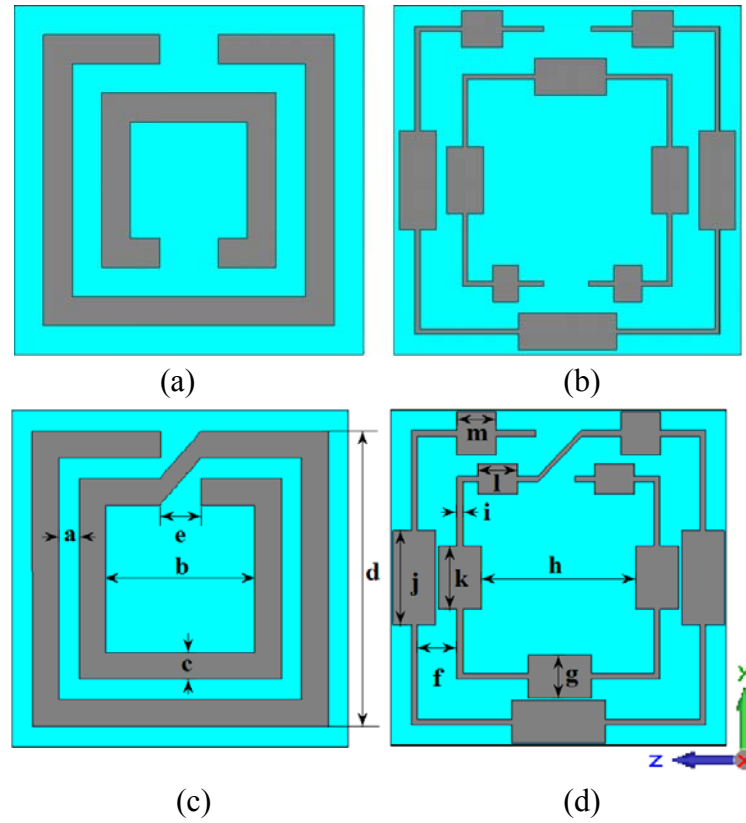
Fig. 6.18. The SIR-DSR and SIR-spiral Structures.

The dimensions of all structures are shown in Table 6.3.

Table 6.3. Dimensions of SIR structures.

Parameter	Value (mm)
a	0.5
b	4.7
c	1
d	9.7
e	1
f	0.84
g	1.17
h	4.53
i	0.17
j	3.12
k	2.11
l	0.80
m	1.30

6.2.2.2. Simulation

In this section the simulation results for each SIR-based structure i.e. SIR-DSR and SIR-Spiral are discussed. It has to be mentioned that we just designed the non-reconfigurable SIR unit-cells to prove the application of this technique in miniaturization. The simulation results are shown in Figs 6.19 and 6.20, respectively.
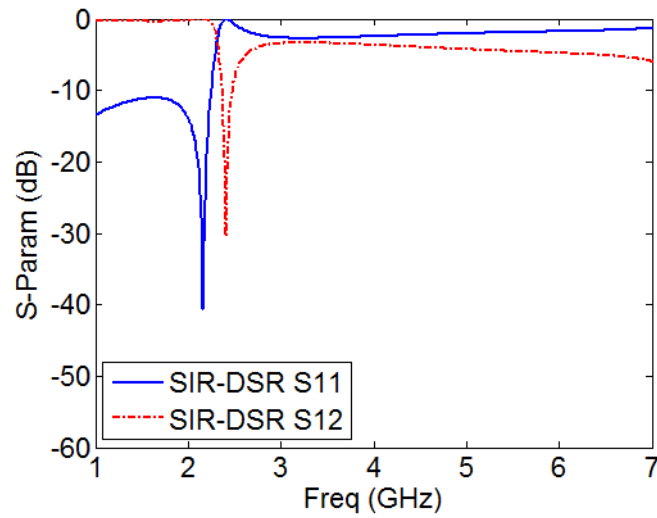
(a)
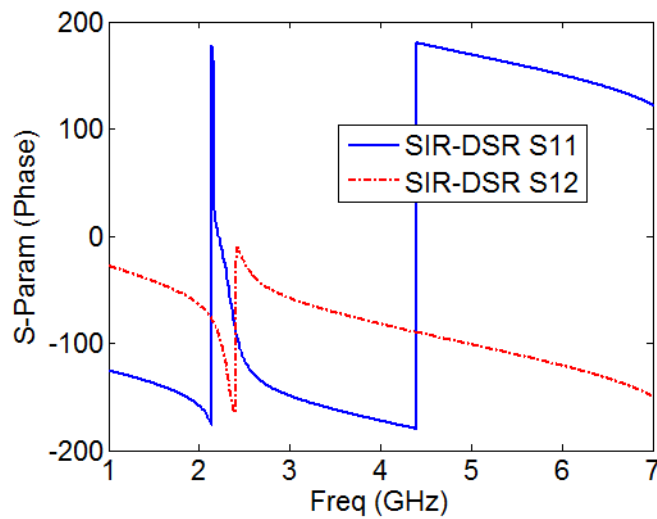
(b)
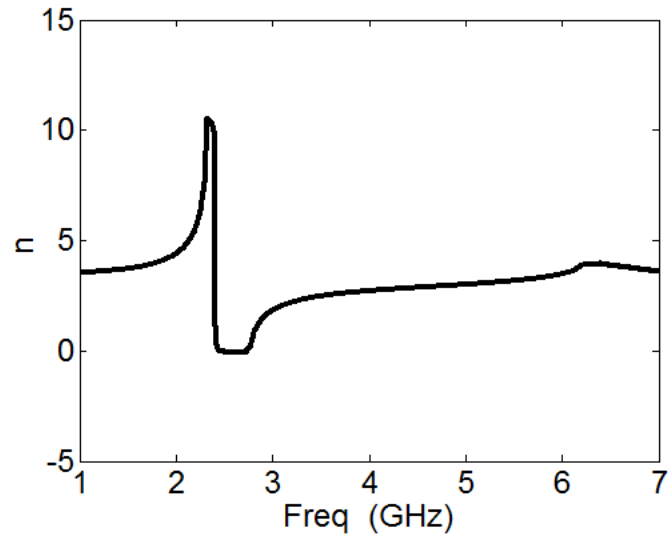
(c)

Fig. 6.19. The S-parameters (a,b) and effective refractive index (c) for the SIR-DSR unit-cell.
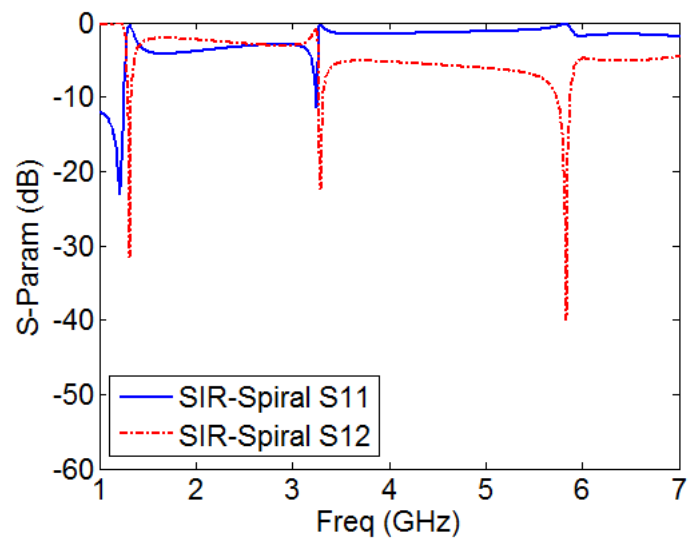
(a)
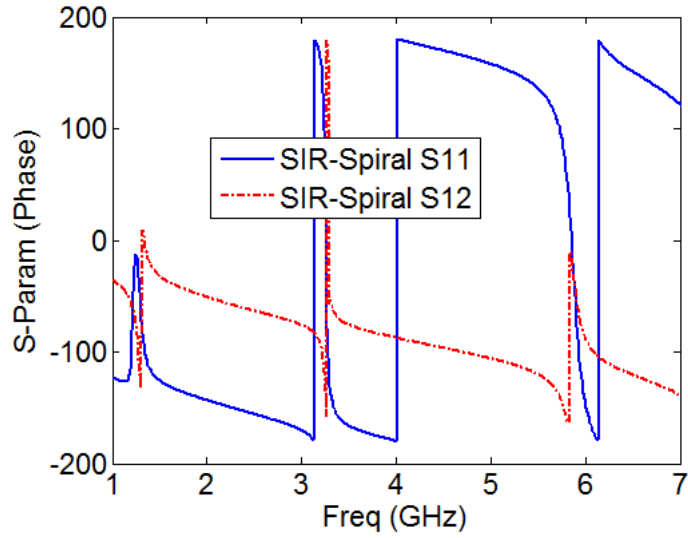
(b)
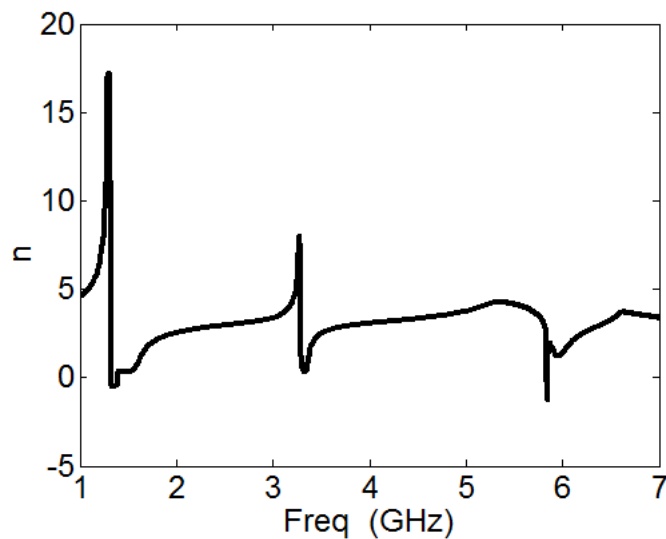
(c)

Fig. 6.20. The S-parameters (a,b) and effective refractive index (c) for the SIR-Spiral unit-cell.

According to the results of Figs 6.19 and 6.20, the first resonance of the S_{12} parameter for the SIR-DSR unit-cell occurs around 2.5 GHz, which shows a miniaturization factor of 0.71 compared to the DSR configuration (resonance at 3.5 GHz). For the SIR-spiral structure, the first resonance of S_{12} is located around 1.4 GHz which shows a miniaturization factor of around 0.65 compared to the conventional spiral. Both of the downward shifts and the resulting miniaturization factors comply with the SIR theory developed in chapter 5.

6.2.2.3. Experiment

Like previously deducted experiments, the FSM method is used to measure the S-parameters of a three dimensional (5×5×20) prototype of the fabricated SIR unit-cells (shown in Fig. 6.21) and the results are shown in Fig. 6.22.
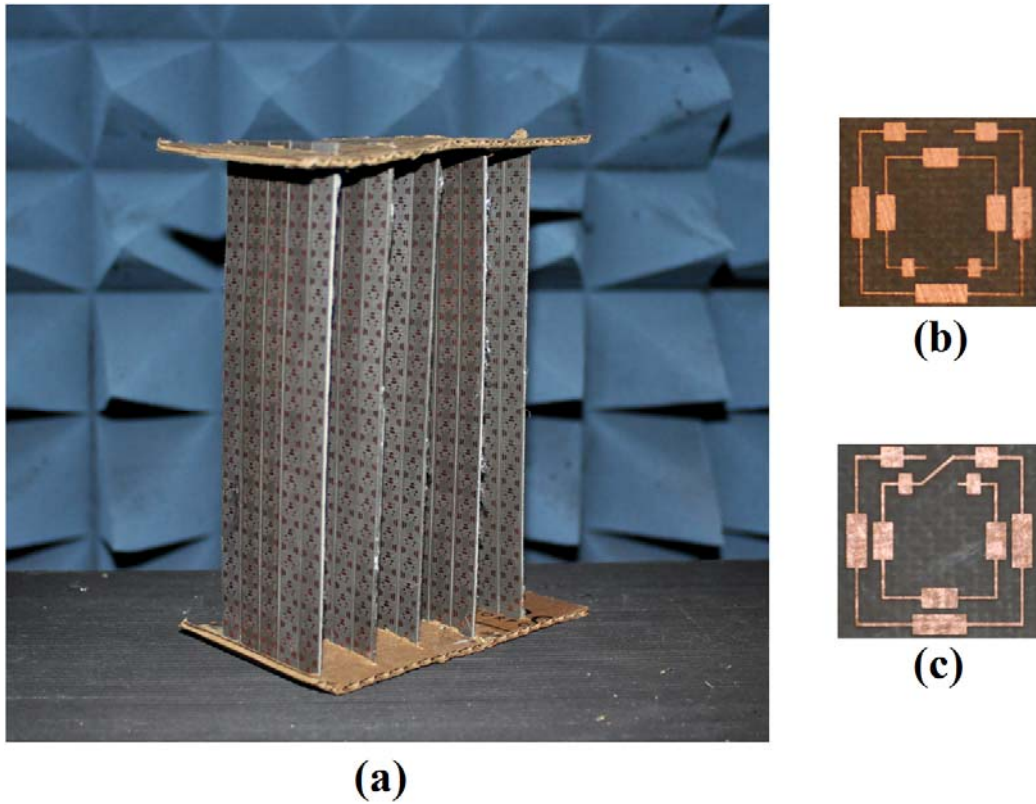
Fig. 6.21. The fabricated SIR-based unit-cell.

(a)   (b)

(c)   (d)
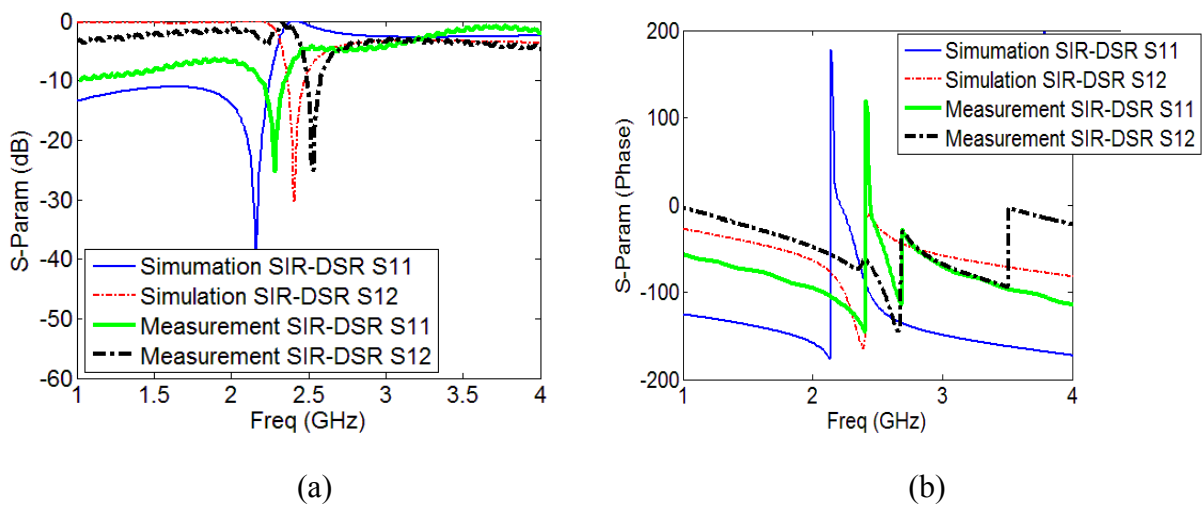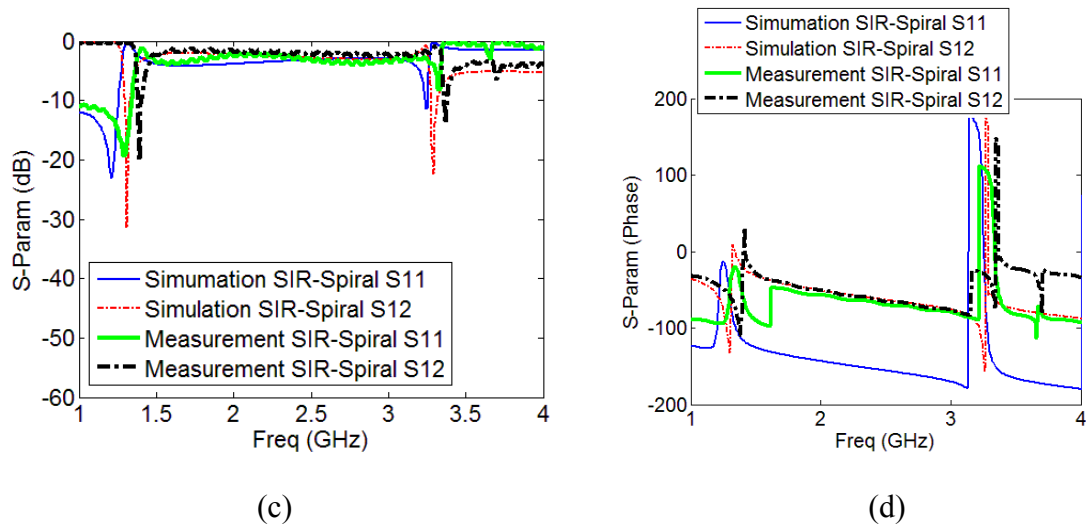
Fig. 6.22. The measurement results for SIR Structures.

The measurement results show a very good agreement with simulation (in terms of the general behavior) due to this fact that the SIR technique provides a miniaturization factor and therefore, a smoother effective medium is formed. The other factors such as the large number of unit-cells and also the dielectric lens play an important role in providing such close-to-simulation results. The slight frequency shift between the simulation and experiment can be attributed to the fabrication error, because this prototype was fabricated on a substrate with high copper cladding (35 μm) and therefore the thin lines of the SIR configurations are made with inaccuracy.

6.3. Conclusion

In this chapter, a novel reconfigurable and compact unit-cell was presented. The reconfigurability feature of the unit-cell originates from the similarity in the geometry of the DSR (double split-ring resonator) and the two-turn spiral unit-cells. According to our investigations, a small change to the geometrical structure of one of these unit-cells can lead to a relatively large frequency shift and consequently modify the frequency response of the unit-cell. This fact has been used to control the refractive index of the proposed unit-cell using the externally controlled PIN diodes. Moreover, a special miniaturization method called the SIR technique has been introduced and used to reduce the size of the structure. The unit-cell has been simulated in the S-band with the HFSS software and its S-parameters have been used in a standard procedure to extract the constitutive parameters of the metamaterial structure. To validate the results, first the non-reconfigurable three dimensional prototypes of DSR and spiral unit-cell have been fabricated and measured using the free-space measurement method and then a smaller 3D

array of the reconfigurable unit-cells with the embedded DC biased PIN diodes is fabricated. Additionally, to show the application of the SIR method in miniaturization, modified SIR-based DSR and spiral unit-cells have been designed, fabricated and measured, and it has been shown these structures are capable of providing a better effective medium as well as a compact structure. To correctly implement the free-space method, a custom-made dielectric lens is fabricated using a molding process from the paraffin wax, which is explained in details in chapter 8. The reconfigurable unit-cell is used as a beam-switching unit in front of a planar antenna in the next chapter. Moreover, in chapter 7, the same geometrical concept is used to design a unit-cell at millimeter-wave frequency band. However, for this structure, the SIR miniaturization method has not been applied and also the diodes are replaced by metallic strips and open circuits at ON and OFF states respectively. Both of these structures will be used in the structure of reconfigurable planar antennas in the next chapter.

Chapter 7

The Antenna Structure

7.1. Introduction

In the previous chapter, the potential of the planar RMDS unit-cell in providing a reconfigurable refractive index was investigated. It was theoretically and experimentally proved that by embedding externally controlled PIN-diodes in the structure of the unit-cell, the desired behavior in switching the refractive index from a low-index to a relatively high-index can be achieved. It has to be emphasized that unlike the conventional point of view regarding metamaterials, our goal was not to provide a negative index of refraction; the main objective of our design was to provide a feasible method to generate a difference between the refractive index of the two states of the unit-cell. This method, incorporated with a reconfigurable unit-cell, is proposed to be a promising solution to control the refractive index of a limited portion of the substrate, which is in turn a very efficient approach to tilt the antenna beam in a desired direction in the Eplane. In this chapter, first we explain the theoretical approach of beam tilting using a controllable two-sectioned medium in front of the antenna. Then, we introduce our unit-cell as a feasible solution to implement this technique and use it in front of an end-fire

antenna operating at the S-band frequency range. Finally, to show the frequency-independent nature of our solution, we design another antenna in the MMW frequency band, and use our proposed approach to switch the antenna beam. The main application of the resulting S-band reconfigurable antenna is in high-speed wireless LAN networks, while the MMW antenna can be used in the future generation of Gigabit indoor wireless networks.

In the following sections, first the structure of the antenna at S-band is presented and then the effect of different configurations of the unit-cell in front of the antenna is investigated by presenting the simulation and experimental results. Finally, the antenna at millimeter waves is designed and the theoretical and experimental results will be provided for different configurations of the unit-cell. However, because of the practical limitations, in the MMW antenna, only the experimental results for the proof-of-concept structure (with the diodes replaced by open circuit and short circuit in the OFF and ON states) are presented.

7.2. Beam tilting Mechanism using a double-sectioned metamaterial medium in front of the antenna

In this section, the theory behind the concept of beam tilting using a double-sectioned medium embedded in the antenna substrate is explained. This approach is used to develop a low-profile antenna with a tilted main beam. In fact, by using metamaterials, we form an artificial dielectric on the surface of the substrate in front of the antenna. Then by incorporating reconfigurable elements (PIN-diodes) in the unit-cells, we can control the refractive index of the dielectric medium and turn the tilting technique into an efficient beam-switching method. The main advantage of this method over the conventional beam-tilting is the very low-profile structure resulting from the metamaterial unit-cells. Furthermore, because the metallic unit-cells can behave like passive directors for the main antenna, we can avoid the gain drop when the beam is tilted.

To investigate the beam-tilting theory in more details, we place an electromagnetic point source, as shown in Fig. 7.1, in the vicinity of a two-layered medium with two different refractive indexes. The electromagnetic wave that exits from each layer undergoes a different phase shift due to the different refractive index and length of the medium.
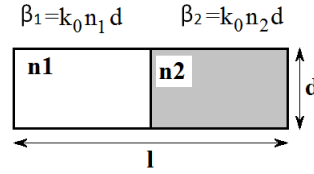
Fig. 7.1. Mechanism of beam tilting using two layered dielectric media [14].

In other words, the scenario depicted in Fig. 7.1 is analogous to a two-element antenna array with a phase shift of β between the elements, which is given by:

$$\beta = k_o \, (n_2 - n_1) \, d \qquad (7.1)$$

The relation between β and the radiation angle φ is given by [14]:

$$\beta = k_o \, l \sin\varphi \qquad (7.2)$$

Therefore, from Eqns. (7.1) and (7.2) the tilt angle is given by:

$$\varphi = \sin^{-1}[d \, (n_2 - n_1)]/l \qquad (7.3)$$

According to Eqn. (7.3) the tilt angle is determined by the difference between the refractive index of the two media and also their dimensions. As we intend to use this technique for an end-fire planar antenna, the above two layered media must to be located on the substrate of the antenna. The best possible solution for changing the refractive index of a limited region of the antenna's substrate is to load the antenna with a properly designed metamaterial unit-cell. On the other hand, because we look for a switching technique, this unit-cell must be reconfigurable and the difference between the refractive index of the modes should be as much as possible. As it has been shown in the previous chapter (Figs 6.11 (c) and 6.12 (c)), there is difference of $n_{Spiral} - n_{DSR} = 1.3$ in the frequency range of 2.8 to 3 GHz. This difference will be used along with Eqn. (7.3) to explain the beam deflection of the designed antenna.

7.3. The S-band antenna loaded with two-sectioned metamaterial medium

7.3.1 Antenna with non-SIR unit-cells

7.3.1.1 Antenna Design

The antenna that we used here as a reference is a wideband printed dipole, which is in fact a modified version of the antenna presented in [83]. A schematic view of the antenna is depicted Fig. 7.2. This antenna consists of a microstrip line to slot line transition and a printed dipole, which is connected to the slot line using a coplanar stripline (CPS) structure. A stepped connection has been used between the stripline and the slot-line to improve the antenna matching. The reason that we chose this antenna is the large bandwidth that enables us to work on the unit-cell resonance without any concern about the matching.

(a)   (b)
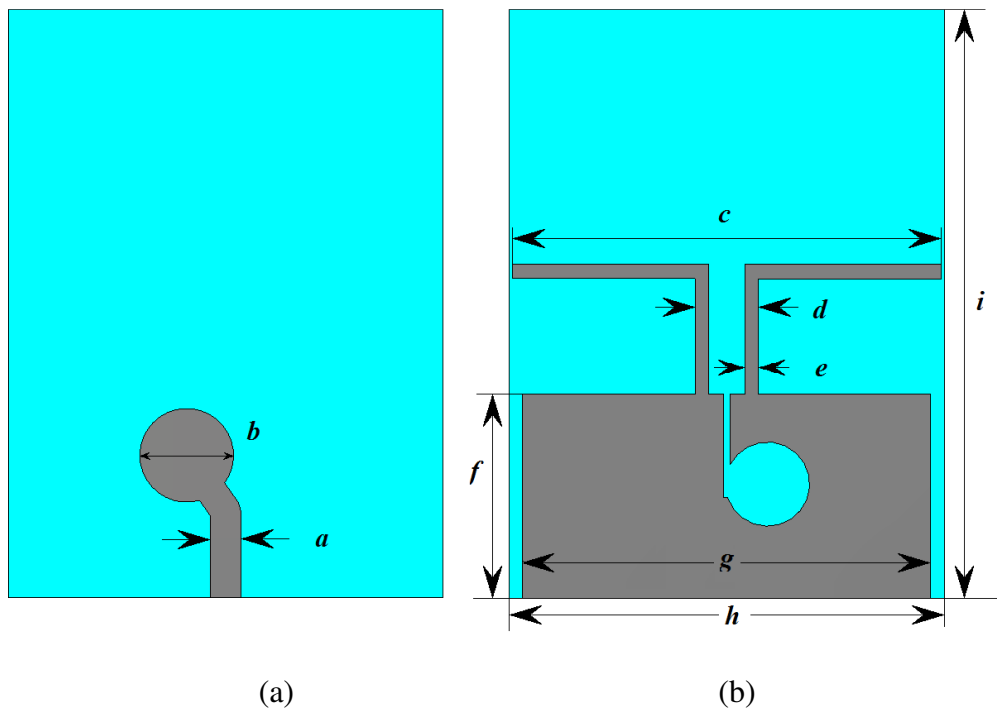
Fig. 7.2. Schematic view of the antenna top (a) and bottom (b).

The dimensions in millimeter are: a=4.5, b=14, c=63, d=9.4, e=2, f=30, g=60, h=64, i=77.

To design a pattern-reconfigurable antenna in the E-plane, a 13×4 array of the reconfigurable unit-cells is printed as a beam-switching unit on the antenna substrate in front of the dipole radiator. It is important to mention that this metamaterial medium can

be considered as a separate block in the whole antenna system, which is specially used for beam-switching purposes and unlike the other conventional methods (such as phased arrays) this block is totally detachable from the main antenna. The DC bias network is also printed as a part of the unit-cells along with 2 kΩ resistors for feeding and RF chokes to separate the DC network from the unit-cells and also unit-cells from each other. A schematic view of this antenna is shown in Fig. 7.3.
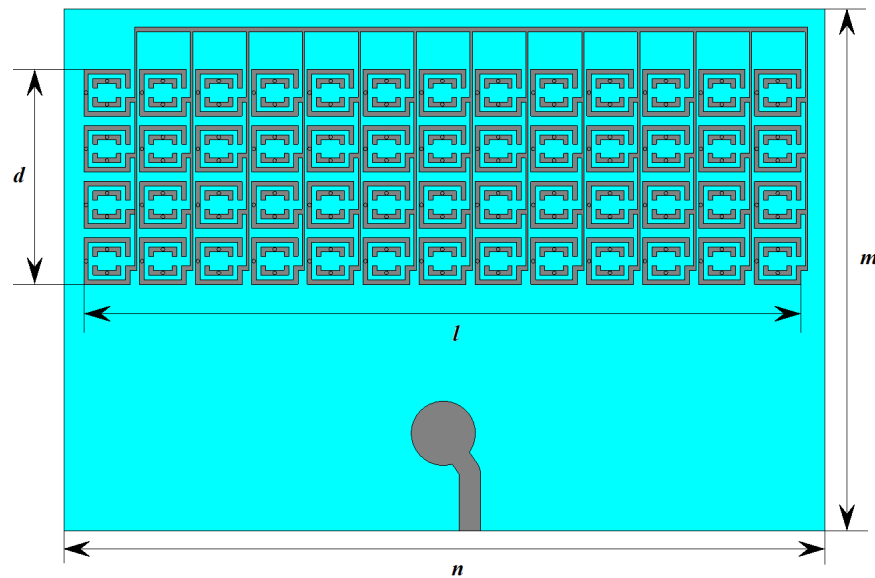
(a)
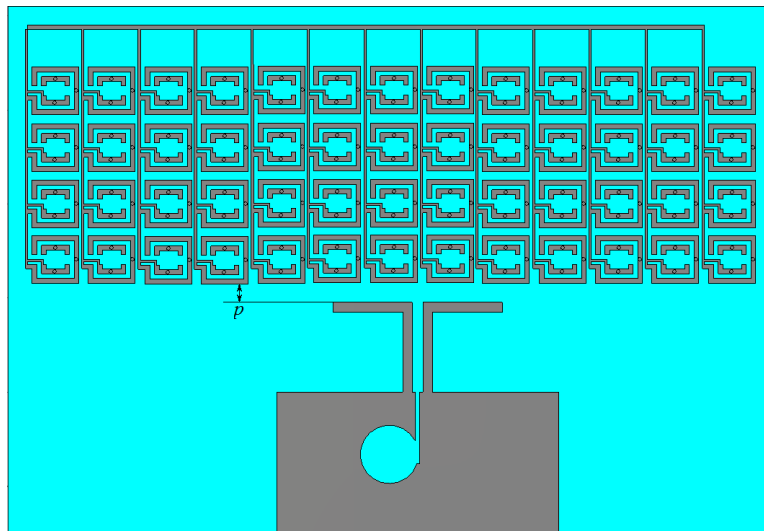
(b)

Fig. 7.3. Antenna with metamaterial unit-cells, (a) top and (b) bottom.

(The dimensions in millimeter are: *d=46, l=154, m=112, n=163, p=4.*)

The final purpose of this metamaterial medium is to control the radiation pattern in the E-plane by controlling the diodes. To do this, first the nine columns on the left side of the substrate are switched to spirals and the other four columns to conventional DSRs. The effect of this configuration on the radiation pattern is shown in Fig. 7.4.

(a)   (b)
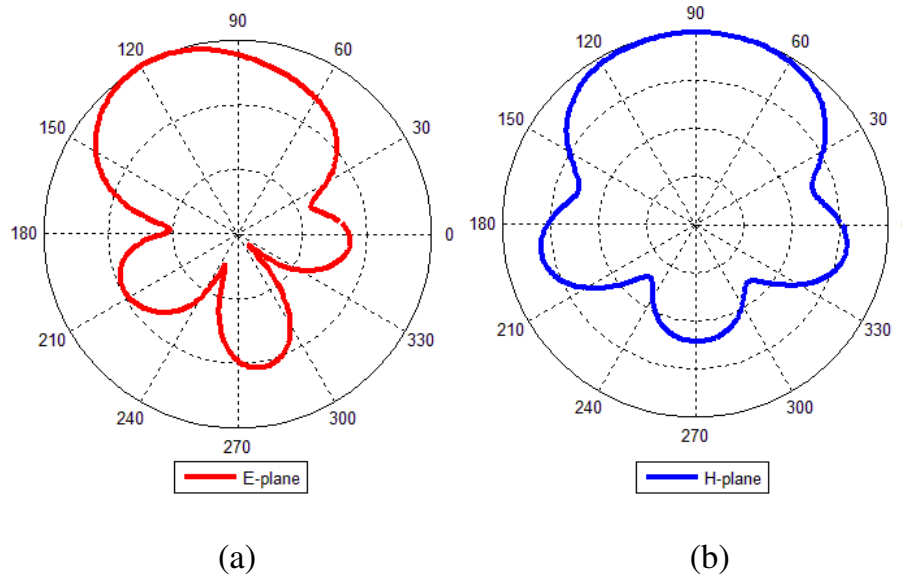
Fig. 7.4. The radiation pattern of the antenna loaded with metamaterial unit-cells at 3 GHz.

The simulation results reveal that the difference between the refractive indices of these two regions leads to a beam tilting of 30° in the E-plane while there is no deflection in the H-plane. The same scenario can be considered when the four right columns are switched to spirals and the rest are DSRs. As a result, by switching the diodes, the antenna beam can be switched from -30° to $+30^o$ in the azimuth plane of the antenna. Using a reconfigurable metamaterial medium, this method of beam tilting not only provides a very low-profile antenna, but unlike most of the tilting mechanisms there is no gain drop observed. In fact, there is even a gain enhancement of 2.1 dB as shown in Table 1. This phenomenon can be easily attributed to the effect of the unit-cells. Because they produce a region with a higher refractive index in front of the EM wave emanating from the antenna, before the wave goes to the air. Therefore according to the Snell's law (Fig. 4.9), the antenna aperture size is increased and the gain is enhanced.

Table 1. Simulated antenna peak gain at S band

Freq. (GHz)	2.8	3.0	3.2
With MTM	7.1 dB	7.2 dB	7.2 dB
Without MTM	5 dB	5.1 dB	5.1 dB

To validate the results, a prototype of antenna with metamaterial loading is fabricated as shown in Fig. 7.5, and the measured radiation pattern of the antenna is plotted in Fig. 7.6.
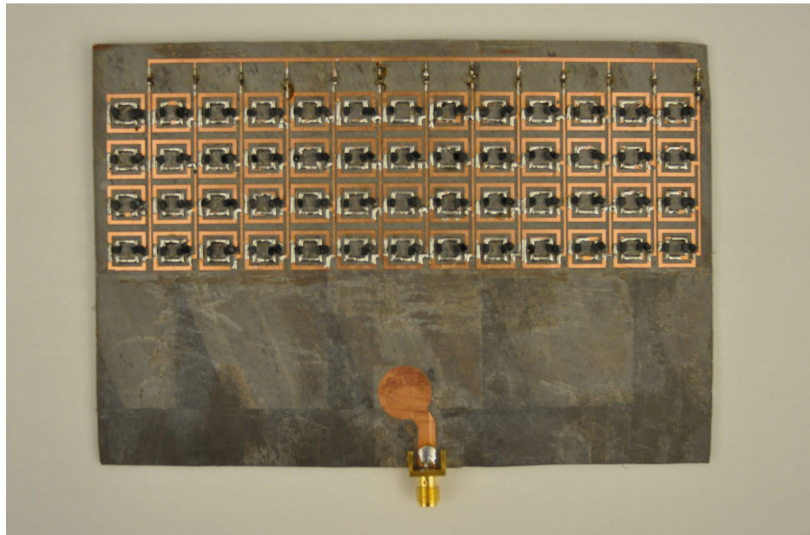
Fig. 7.5. Photograph of the antenna with metamaterial loading.
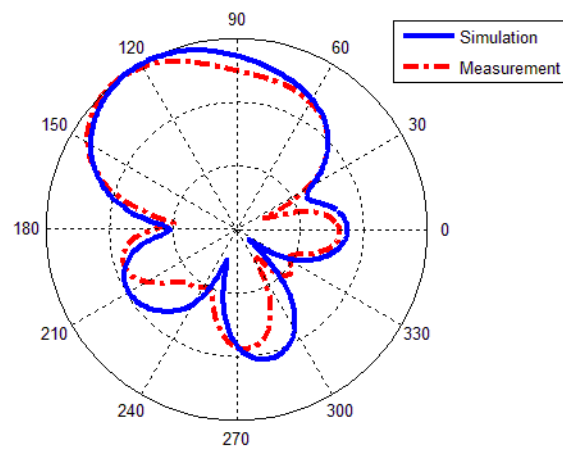
(a)
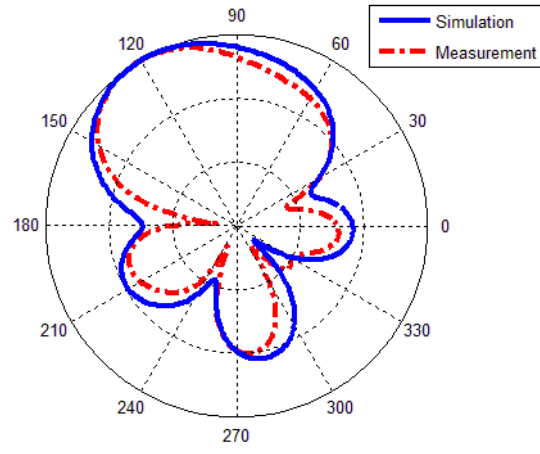
(b)
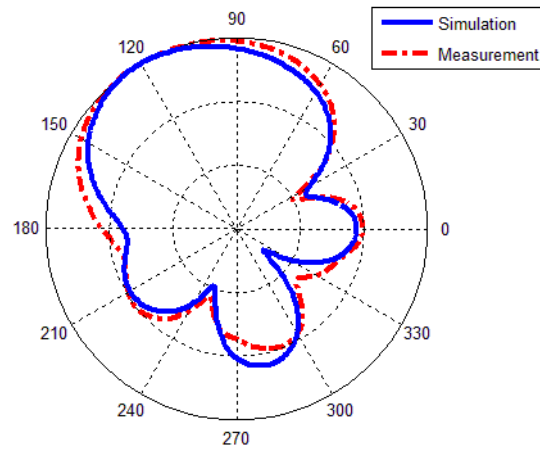
(c)
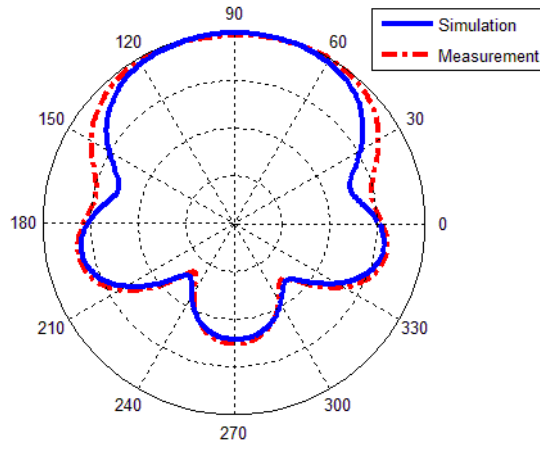
(d)

Fig. 7.6. Normalized Radiation pattern of antenna E-plane at: (a) 2.8 GHz, (b) 3 GHz, and (c) 3.2 GHz, and (d) H-plane at 3 GHz.

According to the results of Fig. 7.6, the radiation pattern of the antenna at 2.8 GHz to 3 GHz is deflected toward the portion of the substrate covered with spiral unit-cells. It is important to mention that according to our investigations on this unit-cell in Chapter 6, in this frequency range, the spiral unit-cell possesses a higher refractive index compared to the DSR structure.

Table 2 compares the measured and simulation peak gains of the antenna with and without the metamaterial loading.

Table 7.2. Measured antenna gain at S band

	With metamaterial	Without metamaterial
Gain (Sim.)	7.2 dB	5.1 dB
Gain (Meas.)	6.4 dB	5 dB

The measured reflection coefficient of the antenna with and without metamaterial is shown in Fig. 7.7, and we can see that there is still a good matching when the antenna is loaded with unit-cells.
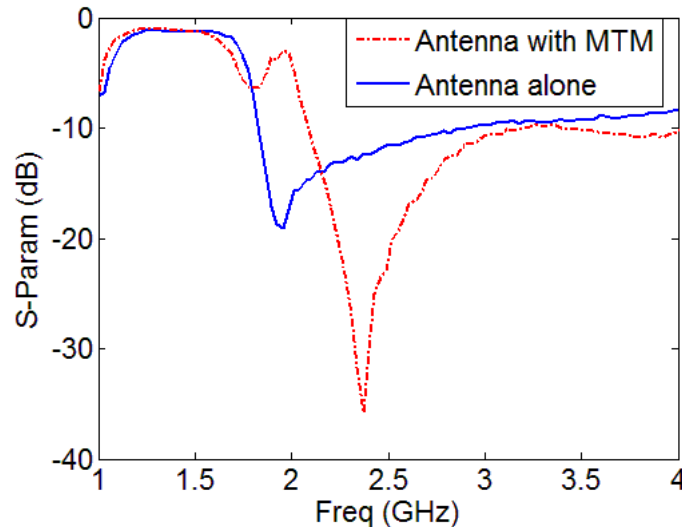
Fig. 7.7. Measured reflection coefficient of the antenna with and without metamaterial.

7.3.1.2 Parametric Study

This section explains the results of a parametric investigation to see the effect of different number of unit-cell rows and also the distance between the antenna radiator and the metamaterial medium on the performance of the antenna in different modes. In this study,

the antenna was simulated having a metamaterial medium with 1 to 4 rows of unit-cells in front of the antenna and the results are shown in Fig. 7.8.
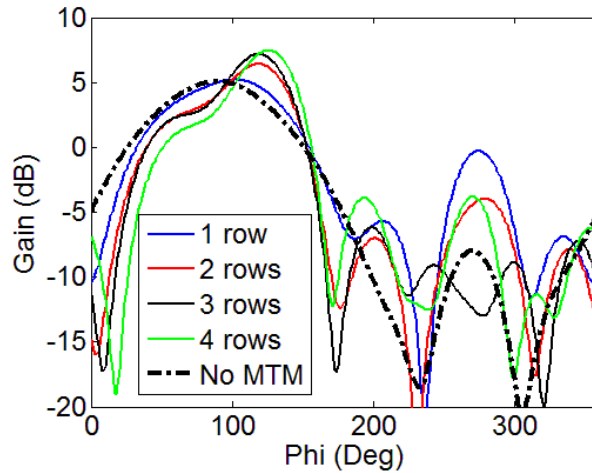
Fig.7.8. Parametric study on number of rows.

Referring to Fig. 7.8, adding the rows, results in a slight gain enhancement in the end-fire direction. However, the side lobe level (SLL) is increased when the number of rows is increased. Therefore, for having an optimized performance, four rows have been added in front of the antenna. The effect of the distance d between the metamaterial medium and the antenna is shown in Fig. 7.9.
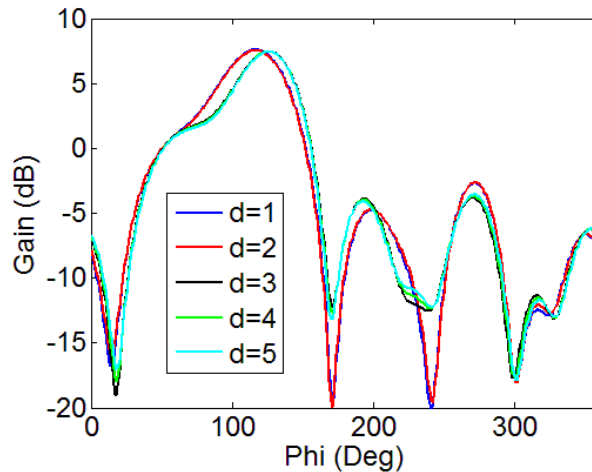
Fig. 7.9. Parametric study on distance between the antenna and unit-cells.

According to Fig. 7.9, when d (the distance between the unit-cell and the antenna radiator) is increased, we have a slight decrease in the gain and at the same time a more visible decrease in the SLL of the antenna. Therefore, the optimized distance of $d=3$ mm has been chosen for all three structures.

7.3.2 Antenna with SIR unit-cells

As we noted in the previous chapter, the SIR method results in a size reduction of the unit-cell. In other words, we can put more SIR unit-cells compared to regular unit-cells in the same physical length. This will result in having a medium with smoother effective parameters, which in turn can improve the antenna parameters. To investigate the effect of SIR-based unit-cells, a 13×4 array of these cells is placed in front of antenna as shown in Fig. 7.10. It is evident that the area that these miniaturized cells occupy is roughly half of the case with non-SIR unit-cells, while the number of the cells is kept the same.
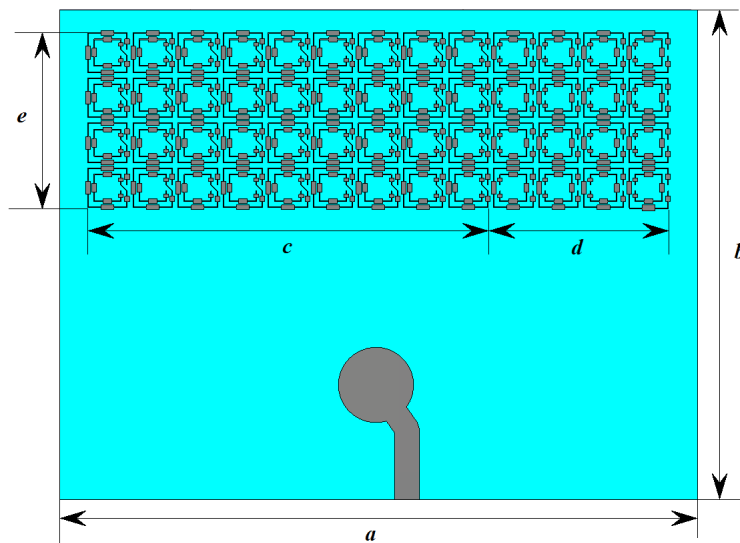
(a)

(b)

Fig. 7.10. The schematic view of the antenna with SIR unit-cells.

(*a=116, b=89, c=*65, d=40, e=32 *mm*)

The radiation pattern of this new design in the E-plane is plotted in Fig. 7.11.
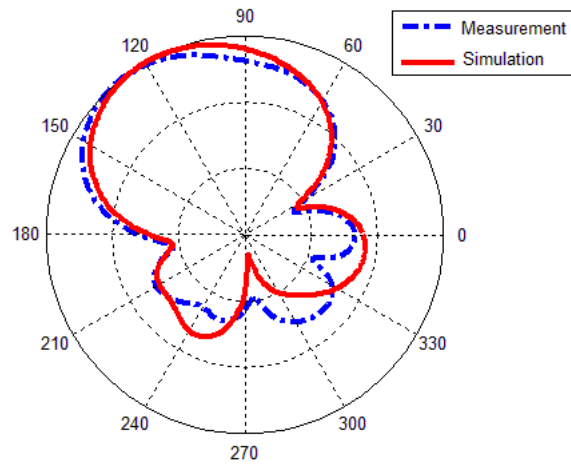
(a)
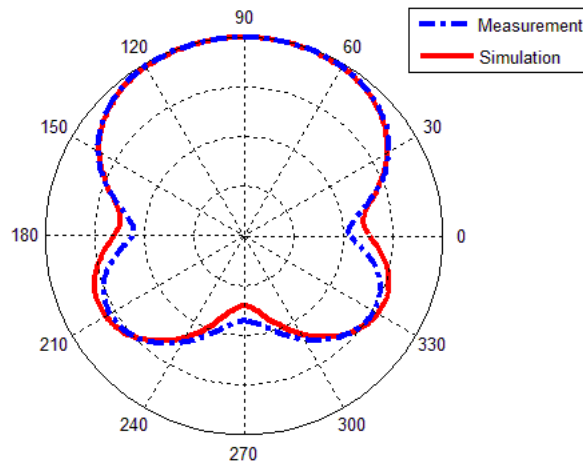
(b)

Fig. 7.11. Radiation pattern of antenna loaded with SIR unit-cells in (a) E-plane and (b) H-plane, at 2.8 GHz.

The reflection coefficient of the antenna with the SIR-based medium is measured and plotted in Fig. 7.12, which clearly shows that it doesn't affect the antenna matching over the working frequency range.
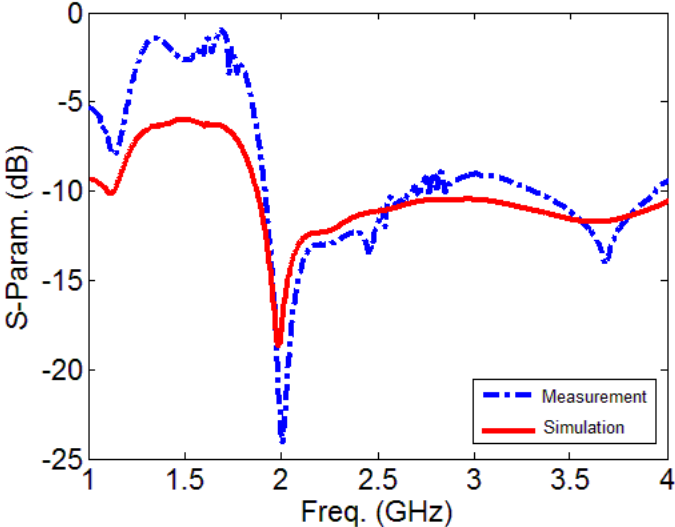
Fig. 7.12. Reflection coefficient of the antenna with two-sectioned SIR metamaterial unit-cells.

7.4. The Millimeter-Wave Antenna Design

As mentioned in the previous sections, design and implementation of a beam tilting technique at the millimeter wave frequencies is one of the main objectives of this thesis. On the other hand, the S-band reconfigurable antenna based on the application of RMDS unit-cell demonstrates a very easy and low-profile solution for beam switching applications. It is important to mention that the unlicensed ISM band from 57-64 GHz has attracted a lot of attention due to its great potential for a variety of indoor high-speed applications [84-85]. However, this frequency range suffers from high path loss because of the high free-space propagation following the Friis' formula [86]. The solution to this problem is to utilize directional high-gain antennas [87] and to ensure that the antenna has the proper spatial coverage, it is necessary to use beam-deflection and pattern reconfiguration techniques [88]. Various methods have been proposed for millimeter-wave reconfigurable-pattern antennas including liquid crystal phased arrays [89] and Butler matrix [90]. However, all of these methods have their own problems such as gain drop, complexity of implementation and increasing the overall size of the antenna. But the method that we used in this thesis has much potential to be used on the structure of MMW antennas for future indoor Gigabit WiFi applications.

To fabricate the antenna, we use LPKF laser machine that has the maximum accuracy of 0.05 mm. This means that with this technology we are able to implement the RMDS unit-cell without any problem. However, it is not possible to fabricate the SIR-RMDS unit-cell because it requires the maximum accuracy of 0.005, which is beyond the range of our machine. But because for the MMW band miniaturization is not a crucial factor, we can simply focus on the design of RMDS unit-cell at the millimeter-wave band. It has to be mentioned that in this thesis, we only present the proof-of-concept structure for the MMW antenna and the reconfigurable antenna with reconfigurable unit-cell remains as a possible future subject where radio frequency micro electromechanical switches (RF MEMS) can be used to implement the structure in an active format.

Fig. 7.13 shows the schematic view of the antenna used as a reference at 60 GHz. The antenna is designed on a Rogers Duroid/RT 5870 substrate with the relative permittivity of ε_r=2.33 and the thickness of h=10 mils or 0.254 mm. The structural parameters of the antenna in millimeter are as follow: a=14, b=16.25, c=0.65, d=0.46, e=0.30, f=0.2, g=0.95, h=7, i=8.85, j=2.20, k=1.45.
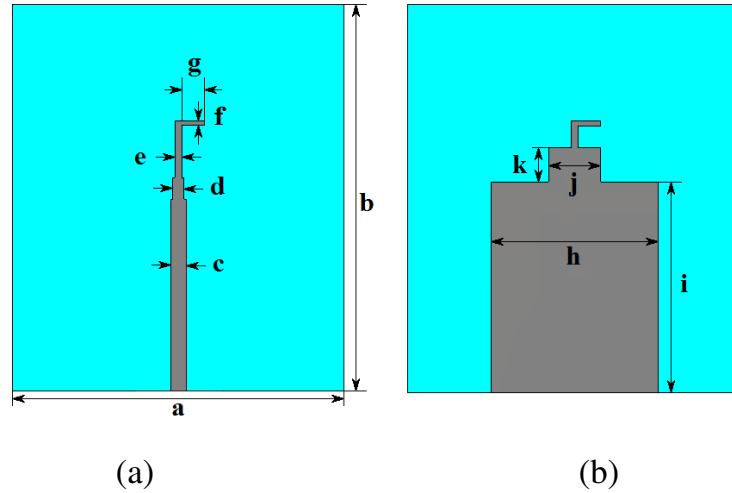
Fig. 7.13. The reference antenna at millimeter waves.

The metamaterial that we used in front of this antenna is composed of a two-sectioned medium each with different unit-cells as shown in Fig. 7.14.
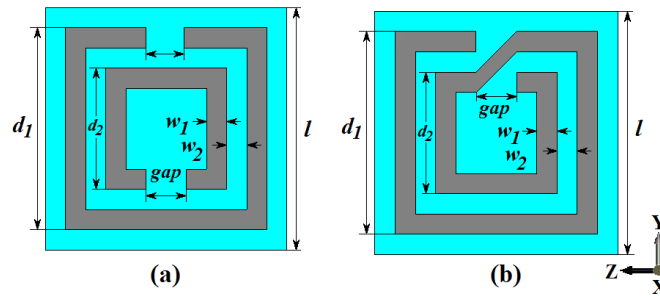
Fig. 7.14. The schematic view of the MMW unit-cells.

The dimensions of these unit-cells in millimeters are listed as follow: d_1=0.45, d_2=0.27, l=0.55, w_1=w_2=0.045, and gap=0.092. Both of the unit-cells are designed on a Rogers/RT 5870 substrate with ε_r=2.2, δ=0.0009 and the thickness of 10 mils or 0.254 mm. The HFSS software is used for simulation for an incident electromagnetic wave traveling along the Z direction and having a Y-polarized electric and an X-polarized magnetic field. The PEC and PMC boundary conditions are used along Y and X directions, respectively and two waveguide ports are located in the Z direction. The simulated S-parameters for each configuration is plotted in Fig. 7.15.
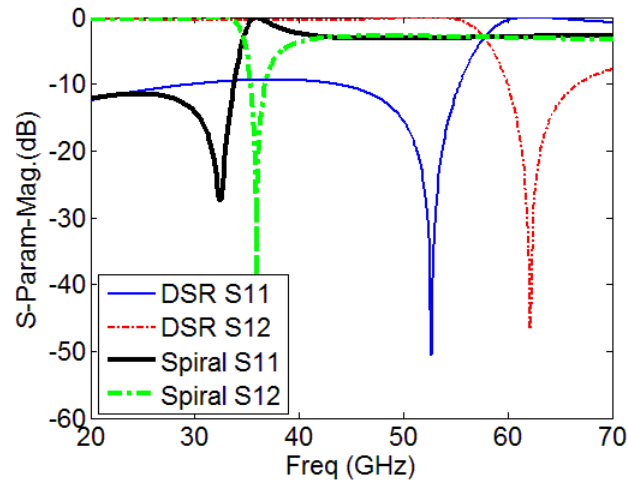
(a)
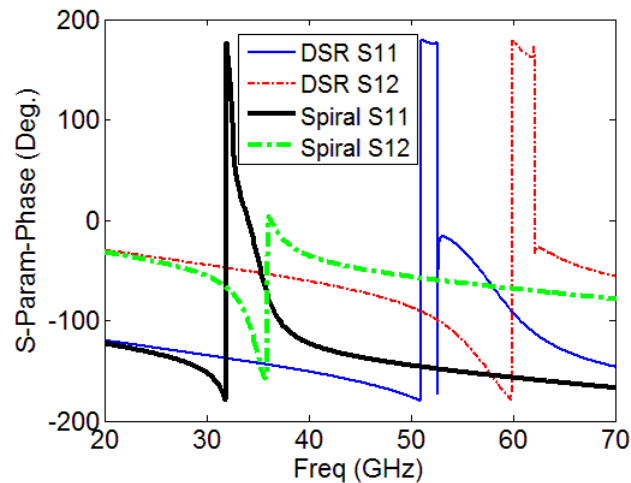
(b)

Fig. 7.15. The simulated S-parameters Magnitude (a) and phase (b).

According to Fig. 7.15, a downward frequency shift can be observed in the spiral unit-cell compared to the DSR structure. This behavior is due to the higher overall capacitance of the spiral compared to DSR, which is in turn due to the higher surface current on the rings of spiral as explained in [75]. The results of Fig. 7.15 are used to extract the effective refractive index of the structure and the calculated parameters are shown in Fig. 7.16.

(a)

(b)
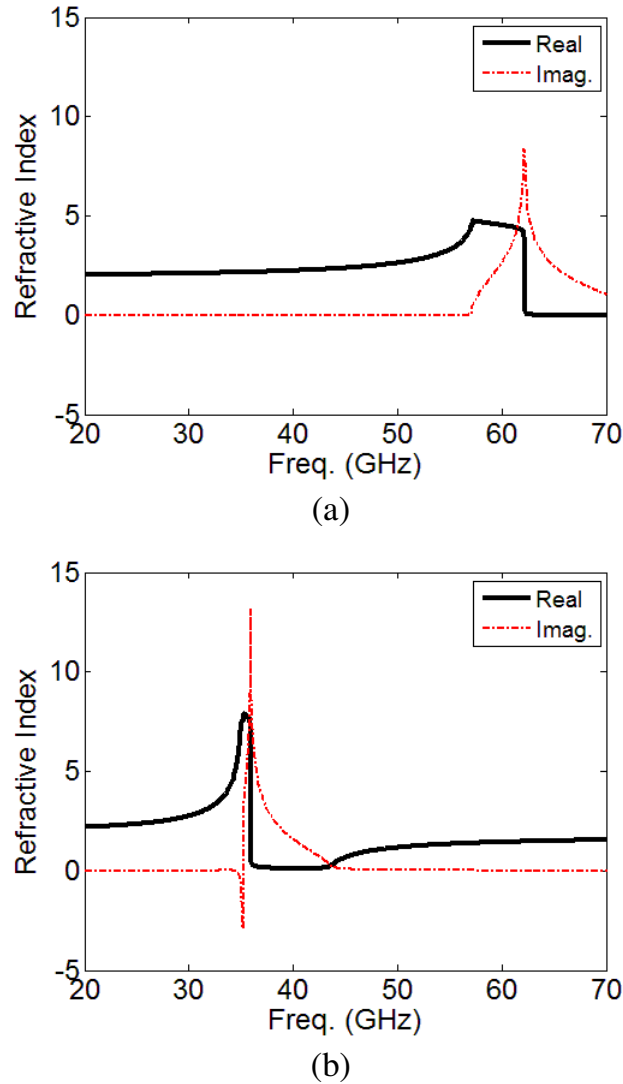
Fig. 7.16. Extracted effective parameters of the unit-cells.

Referring to Fig. 7.16, the DSR unit-cell provides a refractive index around n_{DSR}=5 at 60 GHz while the spiral unit-cell provides n_{Spiral}=3 at the same frequency. In fact the resonance frequency of the spiral unit-cell occurs around 35 GHz and consequently at 60 GHz we don't see any abrupt change in the refractive index of the structure and its refractive index is almost flat around 60 GHz. In other words, a small modification in the geometrical structure of the unit-cell can provide different refractive indices for the two sections of metamaterial medium. Because of this difference in the refractive index, the wave that enters the medium undergoes a different phase shift when it enters different sections of the metamaterial medium and according to [67] this different phase shift will result in the antenna beam tilting toward the spiral region.

To provide the tilt angle, a two-sectioned metamaterial medium as shown in Fig. 7.17 (a) is designed and placed in front of the dipole antenna of Fig. 7.13 and the resulting structure is shown in Fig. 7.17 (b) and (c).

(a)

(b)   (c)
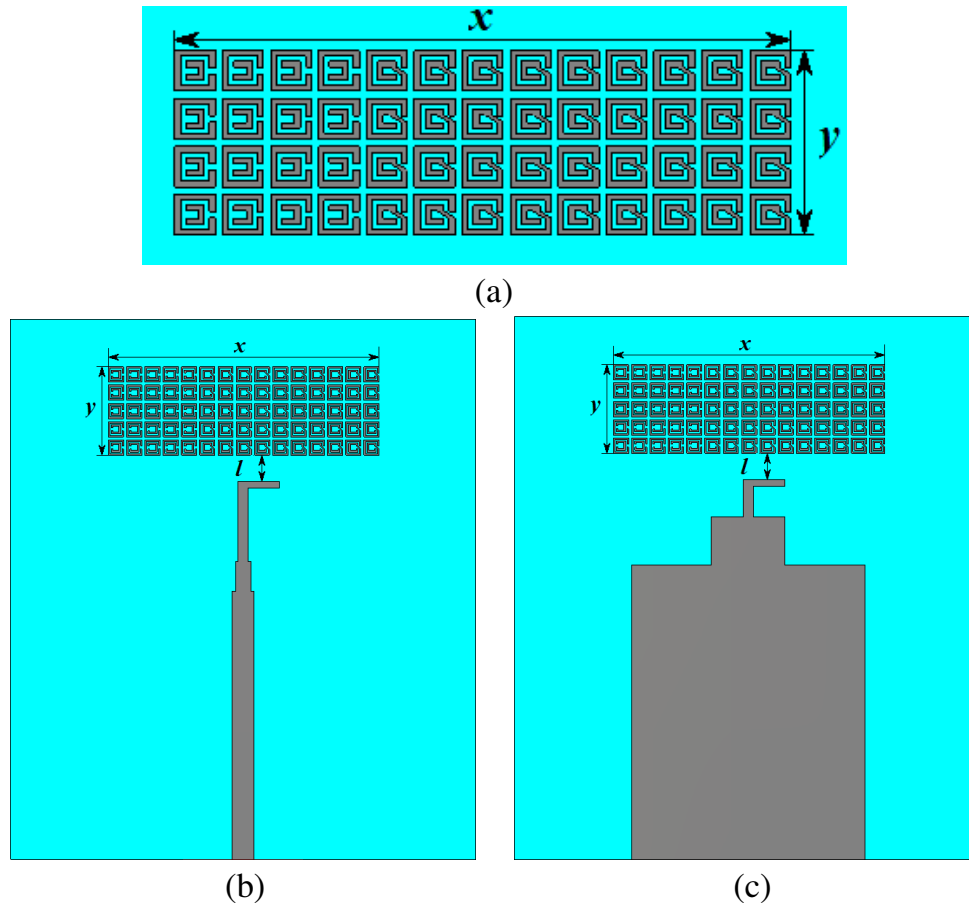
Fig. 7.17. The two-sectioned metamaterial medium (*x=9.07*, *y=2.71* and *l=0.85 mm*)

The normalized simulated and measured radiation pattern of the antenna with metamaterial unit-cells in the E-plane at 60, 61, 62 and 63 GHz are shown in Fig. 7.18. From this, it can be noted that the antenna beam is 32° tilted toward the place of spiral unit-cells. The radiation pattern in the H-plane is shown in Fig. 7.19 and it is without tilting as expected.
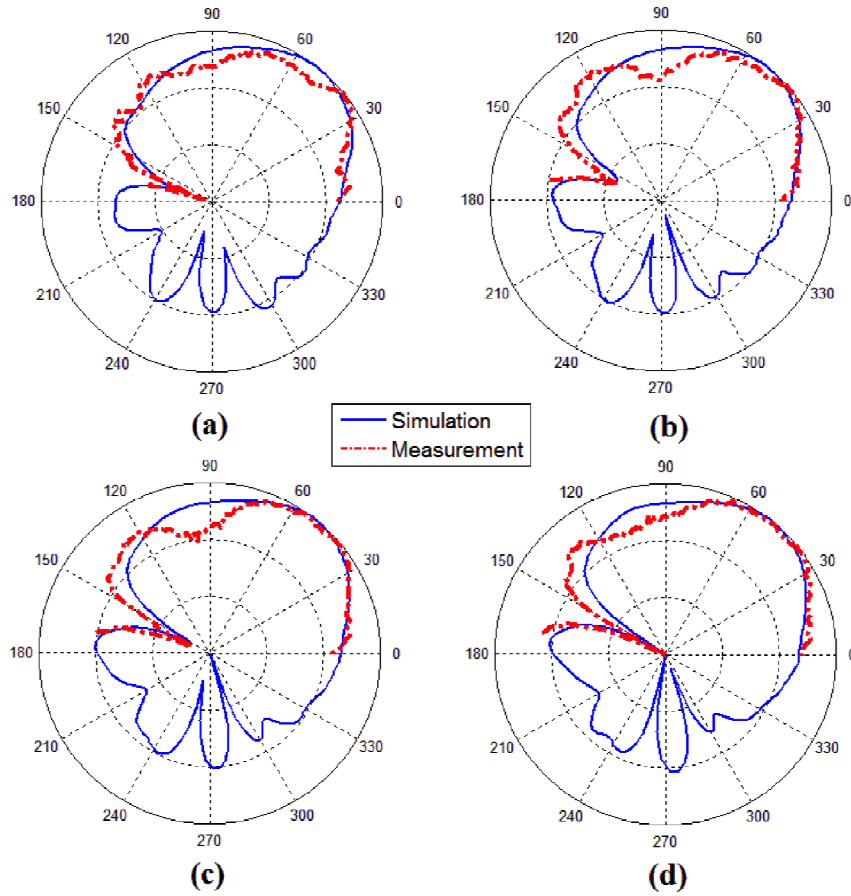
Fig. 7.18. Normalized Measured and Simulation radiation pattern in the E-plane.
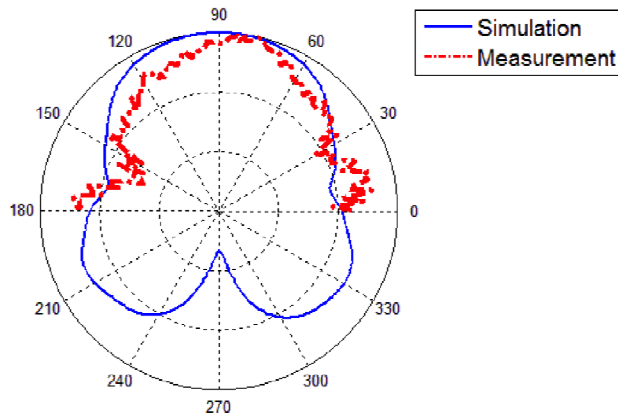
Fig. 7.19. Normalized radiation pattern in the H-plane.

The reflection coefficient of the antenna with and without metamaterial unit-cells are plotted in Fig. 7.20.
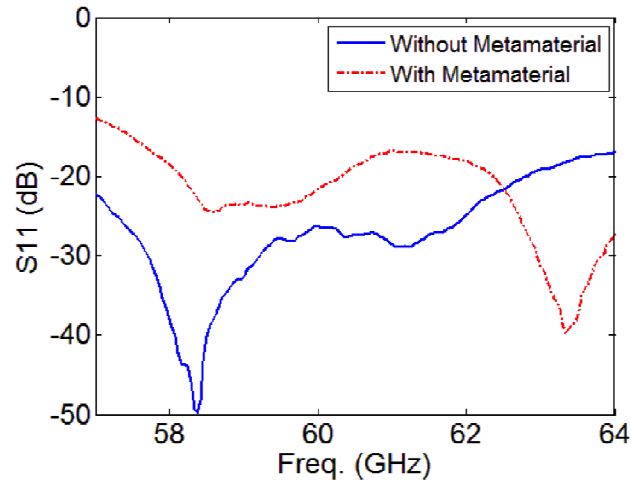
Fig. 7.20. Reflection coefficient of the antenna with and without metamaterial.

To investigate the effect of the unit-cells, the Poynting vector is plotted in Fig. 7.21 as below.
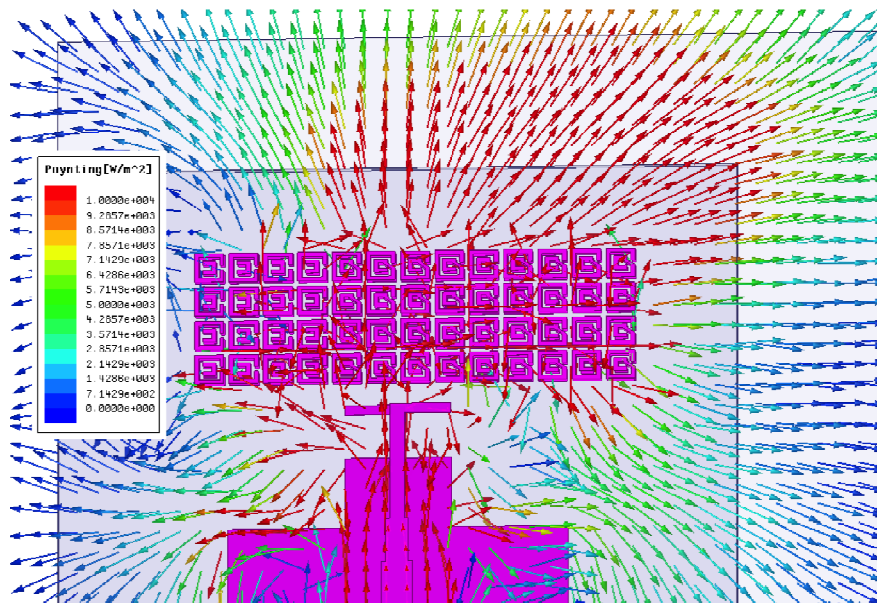
Fig. 7.21. Poynting vector of the antenna with metamaterial unit-cells.

It can be observed in Fig. 7.21 that the direction of the Poynting vector is rotated toward the spiral section of the metamaterial medium. The tilting mechanism is based on the difference of the refractive index in different sections in front of the radiator. The antenna gain is shown in Table 3 for 60-63 GHz and the measurement and simulation results show a good agreement. According to the results, in addition to the tilt angle, a gain

enhancement of 2.4 dB can be observed compared to the antenna without the metamaterial medium.

Table 7.3. MMW antenna gain at different frequencies.

Freq. (GHz)	60	61	62	63
Simulation Gain (dB)	9.4	9.6	9.7	9.8
Measurement Gain (dB)	8.9	9	9.2	9.6
Dipole gain (dB)	7.4	7.6	7.7	7.8

To validate the simulation results, the antenna was fabricated and measured. Fig. 7.22 shows a photograph of the fabricated prototype.

Fig. 7.22 The fabricated prototype at millimeter waves.

The peak gain measurement at different frequencies was performed using the comparison method with a known standard horn antenna, following the equation:

$$G_{AUT} = G_{GS} + 10\log(\frac{P_{AUT}}{P_{GS}}) \qquad (7.4)$$

where G_{AUT} is the antenna gain and G_{GS} is the standard horn antenna gain. The measured peak gain is obtained by calculating the power from the antenna under test and the standard horn in receiving mode (P_{GS} and P_{AUT}, respectively). The 1.85mm version of the V-type end-launch connector (model no.1893-03A-5) was used for the measurements.

7.5. Comparison With Phased Array Technique

In this section, we compare the dimensions of our structure with a MMW phased array antenna system developed in [91]. In this paper the authors proposed an angled-dipole structure and used it in an 8-element array. We have to emphasize that the objective of this comparison is only to show that our metamaterial-based method is capable of providing much smaller dimensions compared to conventional methods. Fig. 7.23, which is derived from [91] shows the structure of their 8-element array.
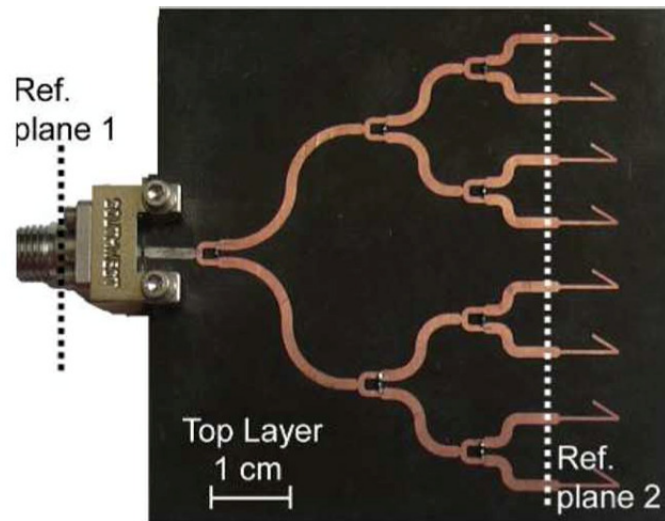
Fig. 7.23. The eight-element angled-dipole array derived from [91].

This antenna array operates at the frequency range of 20-28 GHz, and the dimensions of the antenna are around $5\lambda \times 5\lambda$, which makes it a very bulky prototype. In comparison, our MMW prototype (Fig. 7.24) is only $3.5\lambda \times 2\lambda$. The gain-enhancement of our method is 2 dB only with one single element, while the eight-element array provides a gain-enhancement of 7.5 dB, which is of course with eight elements. However, the metamaterial-based method can be easily combined with any conventional multi-element array (no need for a phased array) and provide beam switching without going through all the complications of designing a phased array.

7.5. Conclusion

In this chapter, all the metamaterial unit-cells introduced in the previous chapters, have been used to design a novel antenna structure. First of all, a planar antenna at the S-band has been designed and implemented with a reconfigurable metamaterial medium using DC-biased PIN diodes. The unit-cells of this medium can be set to work in DSR or Spiral configurations. According to our investigations, the effect of this medium is deflecting the antenna beam toward the section with the greater refractive index. To prove this idea, the tilting mechanism has been investigated in more details and a simple yet effective theory has been introduced to explain the deflection angle. In the proposed antenna, we can change the position of the spiral (the section with the greater refractive index) and consequently change the beam angle. To control the PIN diodes, a DC bias network has been designed and it has been shown that this network does not have a significant effect on the performance of the antenna. After this section, the SIR miniaturization technique has been applied on the unit-cells to be able to use more unit-cells in the same physicall dimensions. This technique results in a metamaterial medium with smoother effective parameters and consequently, the antenna radiation pattern is improved in terms of SLL compared to the previous design. Finally, the same concept has been used to design another antenna at the millimeter-wave frequency band. In this antenna, fixed or non-reconfigurable unit-cells have been used, but it has been shown that the antenna beam is deflected toward the Spiral unit-cells. Both of these antennas can be used in the structure of the future high-speed wireless LANs.

Chapter 8

The Paraffin Lens

8.1. Introduction

Various methods are used to carry out metamaterial measurement including the free-space method [92], waveguide method [93] and a series of single-cell methods [94]. The waveguide method might be theoretically considered as the ideal procedure for metamaterial S-parameter measurement, because it utilizes the exact setup as the simulation. In other words, in this method, a single unit-cell is placed in a waveguide and the S-parameters are measured using the ports placed at each end of the waveguide. However, in practical applications it is not easy to fit a single unit-cell tightly to a waveguide. Moreover, the bandwidth of this setup is limited and it is also very expensive. Because of these reasons, researchers try to use alternative methods. To avoid using the physical waveguide, and thus reducing the expense of the whole procedure, a series of methods are designed that use a single unit-cell but emulate the PEC and PMC boundary conditions by using conductor sheets and monopole antennas instead of the waveguide walls. One interesting application of this method in lower HF band is explained in [94].

The single unit-cell methods might be cheaper than the waveguide methods but they are still not ideal for the microwave regime, because they have accuracy problems. Another issue of these methods is that they just use only one single unit-cell (and not a real waveguide) which is not ideal because in the effective medium theory, enough number of unit-cells should be used to ensure that the fabricated prototype can be considered as an effective medium. As a consequence, the free-space measurement technique is vastly used for metamaterials, especially in university labs. This method can be used for wideband applications and produce accurate results at a very low expense compared to the waveguide method. However, to ensure the accuracy of the method, we need to properly concentrate the incident wave on the metamaterial prototype using a dielectric lens. Although design and fabrication of a dielectric lens might seem easy, but in low frequencies where the dimensions of the lens and the standard horn antenna used in the measurement procedure are large, the lens fabrication becomes very expensive. In this chapter, we present a solution to reduce the cost of the dielectric lens for the S-band measurements.

8.2. Lens Design and Simulation

The material that normally is used to fabricate a dielectric lens is Rexolite, which is a special polystyrene microwave plastic [95]. This material and the required machining process is very costly for dimensions associated with C and S band applications. Moreover, the density of Rexolite is 1.11 gr/cm^3, which is relatively high and make the fabricated lens very hard to handle. Here, we propose the paraffin wax and molding process as an alternative approach for the lens design and implementation. This material has the permittivity of 2.55 which is very close to Rexolite, while it's density is around 0.88 gr/cm^3 that makes the structure around 20% lighter.

Before going in to the details of the lens structure, it is necessary to explain some of the parameters of the free-space measurement method.
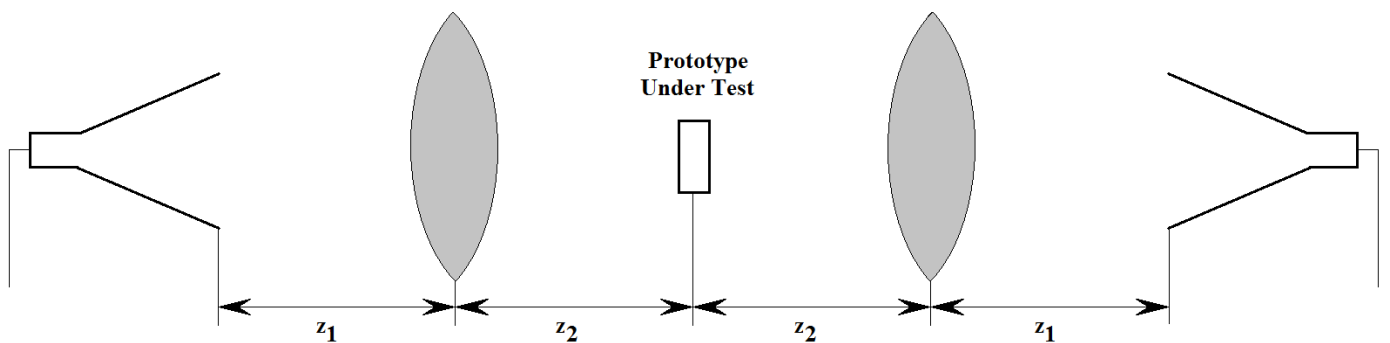
Fig. 8.1. Schematic view of the free-space measurement setup.

According to the Fig. 8.1, in this method the prototype under test is placed between two horn antennas facing each other and the S-parameters are measured using a network analyzer. In our setup we used two AH118 standard gain horn antennas and an Agilent 8722ES network analyzer. The dielectric lenses are used to concentrate the incident wave on the prototype. To do that, the parameters z_1 and z_2 should be chosen to make sure that the beam waist from the horn antenna reaches to the lens and then again the beam waist correctly illuminates the prototype under test. In other words, we have to ensure that the lenses are properly illuminated by the horn antennas. To do that we need to make sure that the lenses are located in the Rayleigh region [96]. But before everything, we need to decide on the diameter of the region on the dielectric lens which is illuminated by the horn antenna beam. We set this diameter equal to 600 mm for our setup, which is three times bigger than the dimension of the AH118 standard horn. According to the calculations carried out in [97-98], the distance z_1 at which a Gaussian beam with the Rayleigh range of z_0 and minimum waist of w_0 can illuminate a radius of w_i is calculated by

$$z_1 = z_0 \sqrt{\left(\frac{w_i}{w_0}\right)^2 - 1} \qquad (8\text{-}1)$$

In the abovementioned equation, w_0 is the minimum waist of the beam, w_i is the desired illuminated radius and z_0 is the Rayleigh range. All these parameters can be calculated from the physical dimensions of the horn antenna. For example the Rayleigh range z_0 can be obtained using the equation below

$$z_0 = \frac{\pi w_0^2}{\lambda} \qquad (8\text{-}2)$$

The same approach can be used to determine z_2 on the other side of the lens. However, in this part of the calculations the dimension of the prototype is used instead of the lens. Knowing all the specifications, the only thing is to shape a lens profile with the corresponding focal length. Normally the design and fabrication process of a dielectric lens starts with analyzing the measurement setup and then the required parameters of the lens is determined and finally according to those parameters, the lens profile is shaped using a machining process. A flowchart of this process is shown in Fig. 8.2 (a).

(a)

(b)
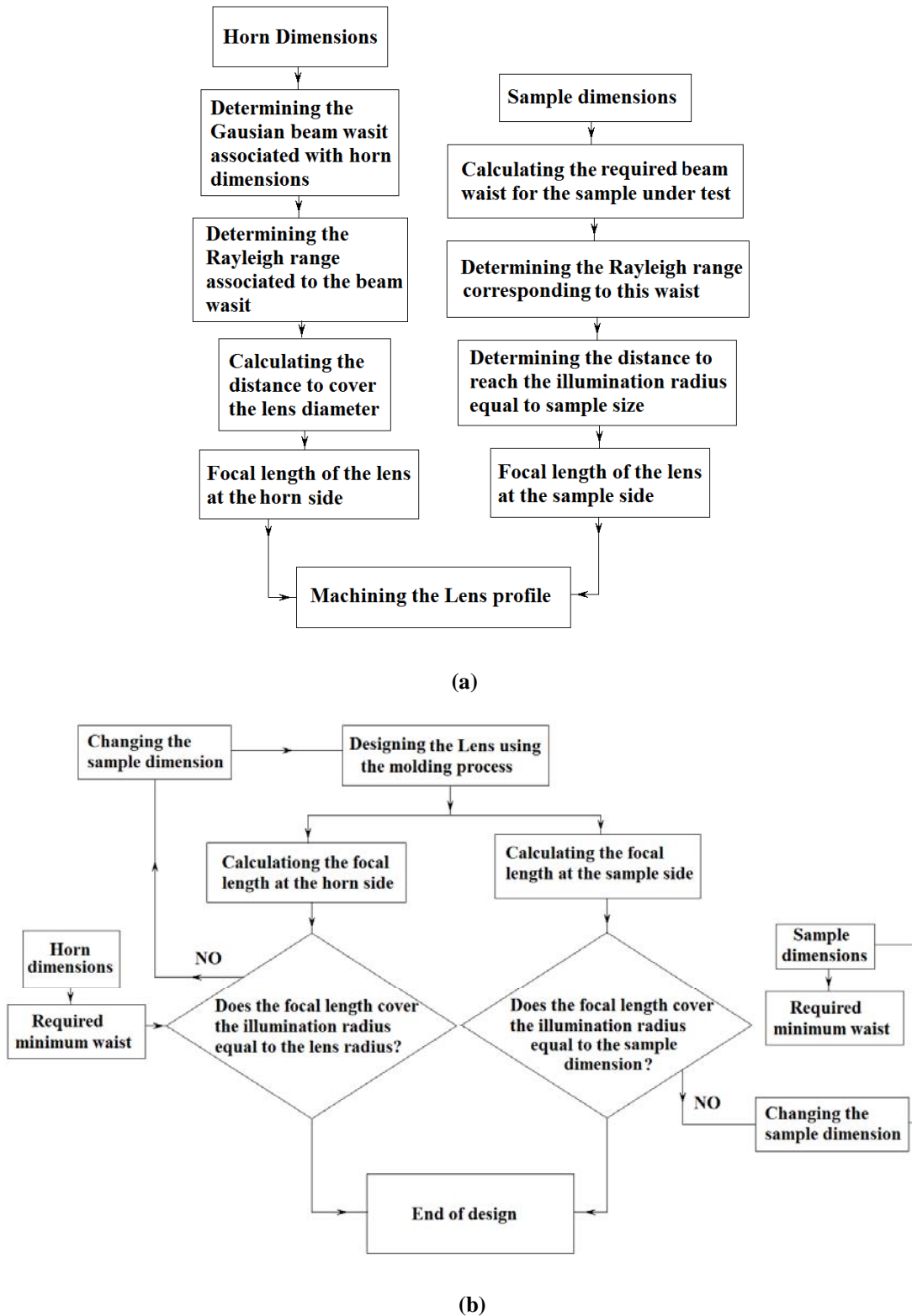
Fig. 8.2. Lens design flowchart conventional method (a) our method (b).
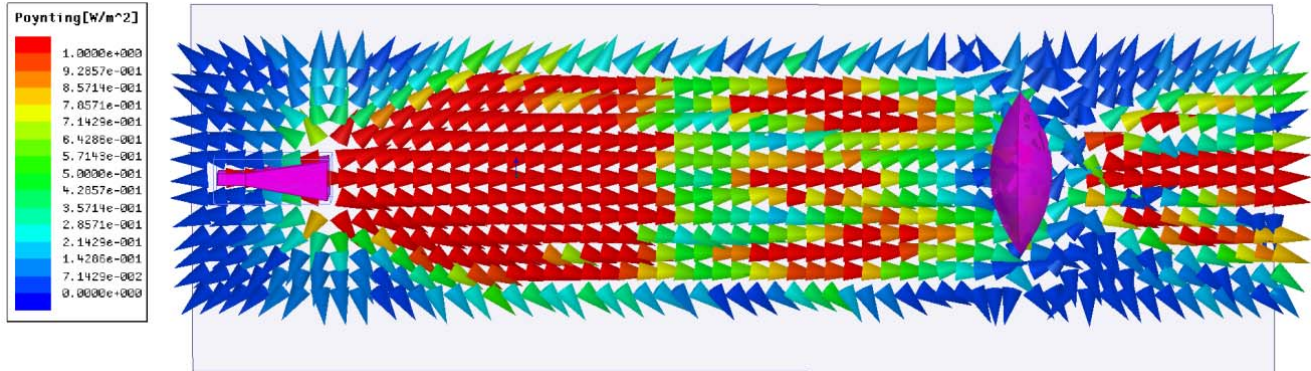
Fig. 8.3. The simulated Poynting vector of the lens.

However, because the main purpose of this chapter is to use molding instead of the machining process, we perform a different flowchart as shown in Fig. 8.2 (b). According to this process, the first step is to choose the lens profile or in other words the mold shape and then determine its focal length. Then, the dimensions and the focal length of the lens, and also the dimensions of the sample under test are used to check if the sample is correctly illuminated. At the end, two parabolic reflectors each with the diameter of 60 inches were chosen to be used as the mold and it is filled with the paraffin material with dielectric permittivity of ε_r=2.25. To determine the focal length of this structure, we simulated it in the HFSS software as shown in Fig. 8.3. In this simulation, a horn antenna with dimensions of 198×142 mm in the X and Y directions is placed at the optical infinity of the lens. The Poynting vector of the wave reaching to the lens is plotted as shown in Fig. 8.3 and according to the simulation results, the focal length is f=300 *mm*. Now according to the flowchart of Fig. 8.2 (b), the parameters z_1 and z_2 are determined as $z_1=z_2$=300 *mm.*

<div align="center">(a)   (b)</div>

Fig. 8.4. Photograph of the molding process used to fabricate the lens.

8.3. Implementation of the Lens

To provide a double convex shape, we used two parabolic reflectors as a mold and the melted wax (which is basically a hot liquid) was poured into the mold structure as shown in Fig. 8.4. To facilitate the process of molding, the wax was melted in small quantities of around one liter and poured into the mold and when each round is cooled down, the next round is added, and finally when the whole material is transformed into a solid structure, the reflectors were removed. It is important to mention that each lens weighs about 30 kg, which is lighter than the equivalent lens made of Rexolite. To properly position the lenses, a wooden fixture is used for each lens, which consists of a square-shaped wooden frame with the dimensions of 35 inches with a big hole for mounting the lens, and a wooden base that is attached to the frame at the bottom side to keep the whole structure balanced. A photo of the fabricated lens is shown in Fig. 8.5.
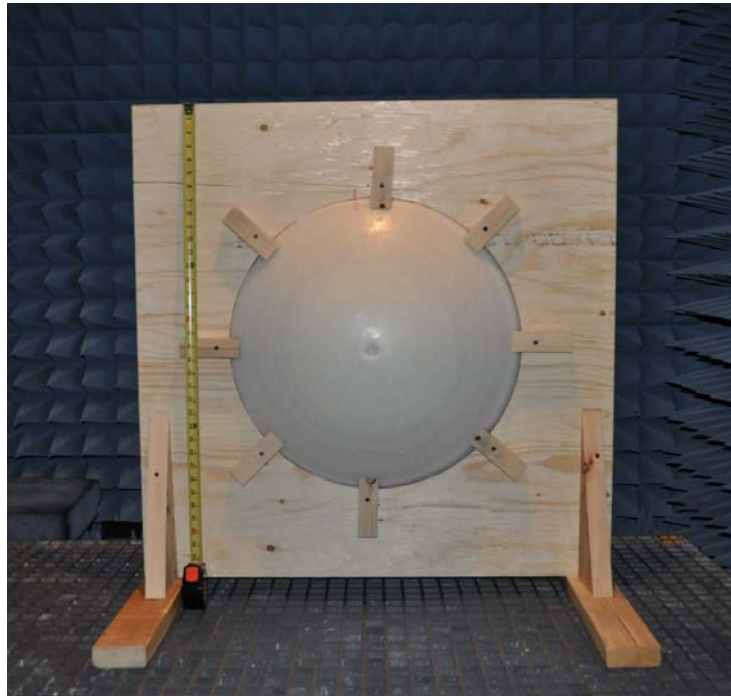
(a)
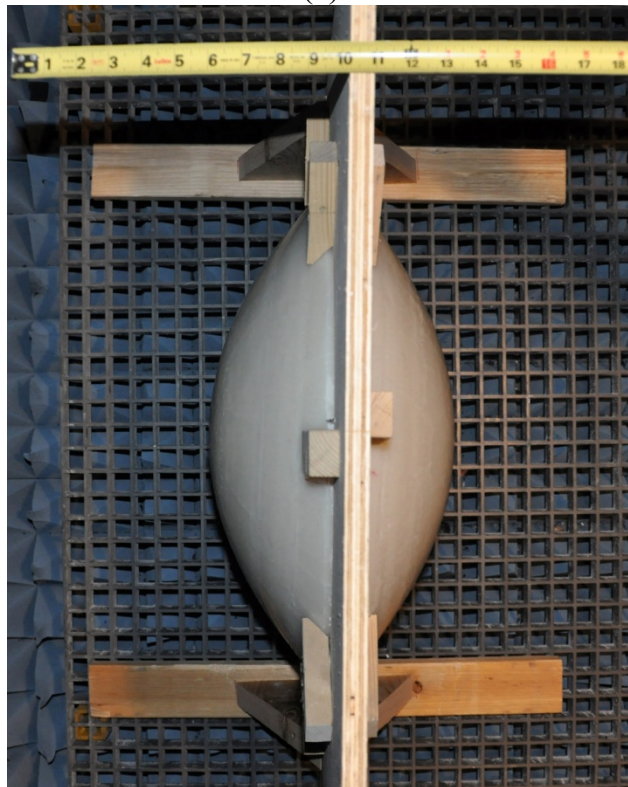
(b)
Fig. 8.5. The fabricated lens front view (a), and Top view (b).

Fig. 8.6. Paraffin dielectric lenses used in the measurement setup.

Finally, two horn antennas are mounted each on a tripod using a custom-made mounting bracket. Therefore, all the dimensions including the distance between the horn antenna and the lens and the lens and prototype can be carefully controlled.

8.4. Conclusion

In this chapter a new molding technique has been implemented to make two dielectric lenses for metamaterial measurement. With this approach, we can use paraffin wax, which is much lighter and less expensive than the Rexolite material. Moreover, we can avoid the machining process for shaping the lenses, which is very expensive for large dimensions. Two custom-made wooden fixtures have been used to install the lenses and they have been used in this thesis to concentrate the beam waist on the prototype under test and measure the S-parameters of the metamaterial unit-cells at the S-band.

Chapter 9

Conclusion and Future Research

9.1. Conclusion

In this work, the applications of metamaterials in radiation-pattern reconfigurable antennas have been investigated. First a novel reconfigurable and compact metamaterial unit-cell has been developed and then it has been used in front of a planar antenna in the S-band to provide beam-switching only by controlling the metamaterial medium. Moreover, to show the agility of this technique, the metamaterial unit-cell has been scaled and used in the millimeter wave band to design a reconfigurable MMW antenna. These two metamaterial antennas are proposed for future high-speed wireless LAN network applications. In order to accomplish the abovementioned goals, a carefully designed methodology has been done during this thesis that is concluded in the following paragraphs.

First and foremost, a comprehensive study has been done on metamaterial structures and their applications in the field of antenna and microwave devices. This study reveals the important role of reconfigurable metamaterial unit-cells in the future of metamaterial theory and also in low-profile reconfigurable applications. For this reason, a novel reconfigurable metamaterial unit-cell has been designed using controlled PIN diodes. As

the next step, we have introduced a new miniaturization technique based on the application of stepped-impedance resonators (SIRs) that can be applied to any rectangular metamaterial structure. In fact, the SIR method, which is one of the contributions of this work, can be used to overcome the size increment caused by embedding the reconfigurable elements such as diodes. Finally, a combination of these two techniques i.e. PIN diodes and SIR method has been used to design the RCSD unit-cell, which has been investigated and verified, by simulation and experimental results. The final unit-cell is capable of switching between two different refractive indexes over a particular frequency range. This unit-cell has also been designed and simulated in the millimeter-wave frequency band. In the final part of this work, the most important objective of the thesis, which is a metamaterial-based reconfigurable antenna that provides beam-switching capability in its azimuth plane, has been realized. To accomplish this objective, the aforementioned reconfigurable metamaterial unit-cell has been used in the form of a two-dimensional array in the structure of a controllable medium in front of the antenna radiator in its E-plane. Using this artificial medium, we can divide the substrate in front of the antenna into two sections and control the refractive index of each section separately. This segmented medium has been proved to deflect the antenna beam. Another interesting fact about the segmented medium is that we can move the high-index section from one end to another by controlling the reconfigurable unit-cells. As a result, the antenna beam can be switched from one end to the other in the E-plane. The same technique has been used to design a beam-switching millimeter-wave antenna. However, because of some technical limitations, the diodes have not been used in the antenna structure and only the tilting effects of the high-index unit-cells have been implemented. The presented beam switching/tilting technique not only provides a very low-profile approach, but also is free of gain drop when the beam is tilted. Moreover, this method can be regarded as a modular technique which separate the tilting block from the antenna block.

The free-space measurement method is used to measure the S-parameters of the presented metamaterial unit-cells. To properly implement this method, two custom-made dielectric lenses are designed and fabricated using a molding process which is much cheaper and easier than the conventional machining process. This method is considered as another contribution of this work.

9.2. Future Research

The work that has been carried out in this thesis opens the area of planar reconfigurable metamaterial unit-cells and proposes their interesting applications in the realization of reconfigurable beam-switching antennas. But it is evident that there are still many other subjects in this area to be investigated. The following paragraphs present some ideas for the future research in this area.

Based on our investigations in this thesis, five main guidelines are proposed for the future research that three of them are directly involved in the unit-cell design, and the rest focus on the antenna structure. The first direction relies on the other types of metamaterial unit-cells that can be used to provide a controllable refractive index. As a particular example, reconfigurable gradient-index unit-cells can be used to deliver a smoother refractive index and thus present a better frequency response. The second recommendation is related to the technology used to provide the reconfiguration feature. Using more advanced tunable elements in the structure of the unit-cells, such as RF-MEMS, can help us to design a fully controllable metamaterial medium where we can tune the refractive index of each unit-cell independent of other unit-cells. Finally, by improving the fabrication technology we can reach better levels of miniaturization in the SIR method. On the other hand, on the antenna level, the beam-switching technology can be extended to the elevation plane by incorporating the unit-cells in a 3D structure. This concept has a lot of potential and can be used to deflect the antenna beam in any arbitrary direction in the space. Furthermore, the possibility of gain enhancement at the same time as the tilting can be considered as the most interesting aspect of the metamaterial beam deflection technique. This can be regarded as and one of the important research axis for the extension of this thesis. In other words, design and implementation of a 3D metamaterial medium, which is capable of providing, customized beam-deflection and controllable gain-enhancement effect can be the most important topic in future of this research work.

Chapitre 10

Résumé

10.1. Introduction

Le résumé des travaux effectués dans le cadre de ma thèse de doctorat est présenté dans ce chapitre. Tout d'abord, les motivations du project de recherche et le problème que je veux résoudre sont expliqués. Ensuite, mes solutions pour ce problème et aussi les objectifs de la thèse sont discutés. Enfin, une conclusion du projet de rechrche est présentée, et mes contributions sont également expliquées. De plus, quelques suggestions et lignes directrices pour un travail futur qui peut éventuellement être ajouté à ce projet sont présentées.

10.1.1. Motivation

Aujourd'hui, les systèmes de télécommunication sans fil utilisent diverses fonctions comme la transmission haute vitesse, la transmission multibande et aussi les caractéristiques comme la possibilité d'avoir un diagramme de rayonnement reconfigurable et autres sortes de diversité comme la diversité spatiale, diversité de fréquence et celle de polarisation. De plus, les dispositifs RF doivent être économiques,

compacts et robustes. Selon tous les points mentionnés ci-dessus, on peut dire que si un seul système peut exécuter toutes les fonctionnalités désirées, la complexité et le coût peuvent être réduits de manière significative. C'est pourquoi les systèmes intelligents sont déployés dans plusieurs d'applications.

La conception de l'antenne est une partie inséparable de tous les dispositifs du système de communication, et l'amélioration de ce dispositif a un effet important sur la performance globale du système. Par conséquent, le domaine de recherche d'antennes reconfigurables a reçu beaucoup d'attention depuis longtemps. En fait, il y a beaucoup de recherches menées sur les différents aspects de reconfiguration du diagramme de rayonnement, de la directivité, de la polarisation et de la fréquence. Pour atteindre ces objectifs, plusieurs méthodes ont été utilisées comme les réseaux d'antennes contrôlés par des outils mécaniques et électroniques. Cependant, toutes les méthodes conventionnelles ont leurs propres inconvénients comme ayant une grande taille ou une conception complexe. Par ailleurs, une antenne individuelle à commande électronique peut ajouter un niveau élevé d'agilité au système. Donc une des motivations de cette thèse est de présenter une nouvelle méthode pour concevoir des antennes agiles.

La bande d'ondes millimétriques ou la bande MMW (30-300 GHz) a attiré beaucoup d'attention au cours des dernières années. grâce à son grand potentiel pour répondre aux exigences modernes de systèmes de télécommunication. Dans la bande MMW, en plus de la haute vitesse et la grande largeur de bande, l'intégration d'antenne avec les autres dispositifs du système est très facile. Pour ces raisons, la bande d'ondes millimétriques est idéal pour plusieurs systèmes: communication sans fil Gigabit, capteurs imageurs, radars automobiles et la communication dans l'espace lointain [1-3]. Tous ces systèmes ont besoin d'antennes à diagramme de rayonnement reconfigurable pour obtenir un balayage électronique du faisceau. Cependant, la bande MMW souffre des hautes atténuations associées à l'évanouissement par trajets multiples, des pertes de conduction et des problèmes de couplage mutuelle. Pour surmonter ces problèmes et améliorer le rapport signal sur bruit (SNR), les différents aspects de la reconfiguration tels que, la reconfiguration de fréquence, de polarisation et du diagramme de rayonnement peuvent être utilisés.

Dans la dernière décennie, les métamatériaux ont fourni de nouvelles solutions pour surmonter les limites et les difficultés des matériaux conventionnels dans le domaine de micro-ondes et antennes [4]. Aujourd'hui, divers types de ces matériaux comme métamatériaux à indice zéro (ZIM), indice élevé et bas indice, sont utilisés dans différentes applications [5]. Cependant, il reste toujours plus pour atteindre dans le domaine des métamatériaux et les concepts comme métamatériaux nonlinéaires et reconfigurables sont encore dans l'etat preliminaire [6]. Les métamatériaux

reconfigurables ont montré un grand potentiel en offrant des fonctionnalités requises dans les antennes intelligentes.

Les concepts mentionnés ci-dessus sur les antennes reconfigurables et les ondes millimétriques ainsi que les applications étendues de métamatériaux nous ont motivés à mener une recherche dans le domaine de la conception d'antennes reconfigurables utilisant des structures en métamatériaux. En conséquence, ce projet vise concevoir, fabriquer, et tester une cellule métamatérial miniaturisée et reconfigurable dans la bande S. Ensuite, on utilisera cette cellule dans une structure intégrée avec une antenne planaire individuelle pour concevoir un balayage électronique du faisceau d'antenne. En plus de l'antenne à bande S, le même concept est mis en œuvre sur une antenne aux ondes millimétriques. Cette méthode présente plusieurs avantages par rapport aux procédés classiques, comme avoir une taille très compacte et assurer gain contract lorsque le faisceau est orienté vers divers angles.

10.1.2. Identification du problème et objectifs de recherche

Des travaux récents dans la littérature ont présenté différentes techniques pour des applications de balayage de faisceau dans les différentes bandes de fréquences [7]. En utilisant des cellules métamatériaux contrôlables, on peut présenter une solution prometteuse pour la commutation de faisceaux et en même temps l'augmentation de gain de l'antenne [8-9]. Par ailleurs, pour intégrer les cellules métamatériaux avec les antennes compactes des systèmes de télécommunication modernes, la taille de cellule doit être réduite autant que possible. Diverses méthodes ont été utilisées pour réduire la taille d'une cellule métamatérial comme l'utilisation de structures fractales ou Greek-key [15]. Cependant, aucune méthode contrôlable n'a été développé jusqu'à aujourd'hui. La conception d'une cellule reconfigurable est un autre défi qui peut nous aider à obtenir plus d'agilité et aussi une meilleure largeur de bande [10]. De plus, les cellules reconfigurables offrent la possibilité de concevoir un bloc indépendant (qui peut être attaché ou séparé de l'antenne principale) pour fournir la reconfiguration dans un système modulaire comme montré dans la Fig. 10.1.
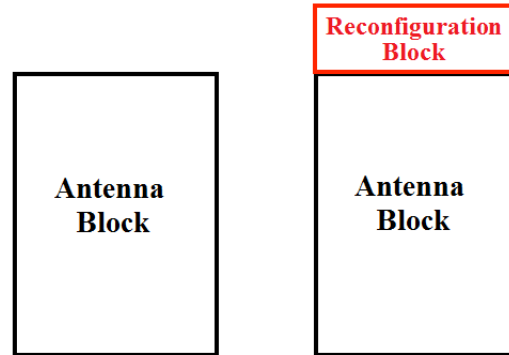
Fig. 10.1. Bloc de reconfiguration dans un système modulaire.

Dans ce travail, une nouvelle classe de cellules métamatériaux compactes et reconfigurables est introduit. L'abréviation RMDS est choisie pour cette classe qui signifie Reconfigurable Miniaturized DSR-Spiral. En fait, cette cellule peut basculer entre une structure spirale compacte et un résonateur à double anneau (DSR). Ces deux configurations sont miniaturisées en utilisant un nouvel algorithme (développé dans cette thèse) sur la base des résonateurs à impédance échelonnée (SIRs). Un réseau de cette cellule est utilisé comme une charge intégrée, qui peut être contrôlé indépendamment en face d'une antenne planaire. Ce mécanisme fournit une méthode très efficace pour contrôler le faisceau de l'antenne dans son plan d'azimut. Il est important de mentionner que contrairement à d'autres méthodes classiques de basculement du faisceau, il n'y a aucune baisse de gain dans notre technique et en fait même une légère amélioration de gain est observé.

Comme les objectifs spécifiques de notre projet, les deux systèmes d'antennes conçus doivent fonctionner à 2.45 GHz et 60 GHz, respectivement. Les deux antennes fournissent un balayage sur tout le plan d'azimut avec l'étape de 60° sur une bande passante de 15% tandis que le gain réalisé est conservé plus de 6 dB et 9 dB pour les prototypes dans la bande S et MMW, respectivement.

10.2. Technique de résonateur à impédance échelonnée pour la miniaturisation d'une cellule métamatérial

10.2.1. Effet de la technique sur une cellule

Dans cette section, on présente une nouvelle technique pour la miniaturisation des cellules métamatériaux. Cette technique est basée sur la structure des résonateurs à impédance échelonnée et elle permet d'atteindre un certain facteur de miniaturisation en contrôlant les paramètres géométriques de la structure. Comme mentionné dans la littérature, la taille d'une cellule métamatérial est dans l'ordre de λ/10 [78-80]. Mais, quand on utilise une conception spéciale pour réaliser un comportement multibande ou reconfigurable, la taille de la cellule est augmentée [81-83]. Cependant, pour considérer le métamatérial comme un milieu homogène, il est crucial d'avoir de petites cellules par rapport à la longueur d'onde. Avec des cellules plus petites, on peut obtenir des performances plus lisses en termes de paramètres S [84].

La structure de résonateur à impédance échelonnée a été mise en œuvre il y a près de trois décennies et maintenant elle est utilisée dans les filtres, duplexeurs et diviseurs. Fig. 9.2 montre la structure échelonnée d'une ligne microruban.
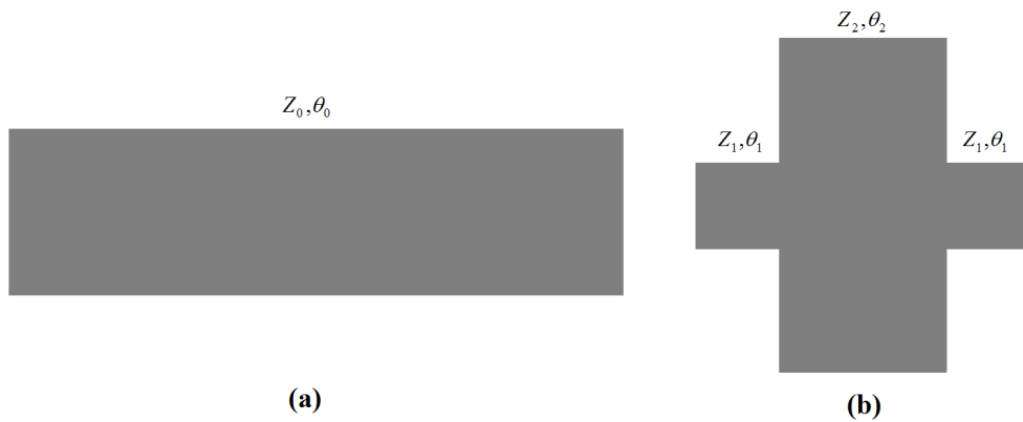
Fig. 10.2. Une ligne microruban classique (a) et sa structure échelonnée (b).

Pour que les deux structures indiqués dans Fig. 10.2 (a) et (b) soient égales, leur matrices ABCD doivent être égales. La matrice ABCD de la ligne conventionnelle peut être écrite comme suit.

$$\begin{bmatrix} A & B \\ C & D \end{bmatrix} = \begin{bmatrix} \cos(\theta_0) & jZ_0\sin(\theta_0) \\ j\dfrac{1}{Z_0}\sin(\theta_0) & \cos(\theta_0) \end{bmatrix} \qquad (10\text{-}1)$$

où Z_0 et θ_0 sont impédance caractéristique et longueur électrique de la ligne microruban conventionnelle (Fig. 10.2 a).

Puis, on peut obtenir la matrice ABCD de la structure échelonnée en multipliant la matrice de chaque section comme expliqué ci-dessous:

$$\begin{bmatrix} A & B \\ C & D \end{bmatrix} = $$
$$\begin{bmatrix} \cos(\theta_1) & jZ_0\sin(\theta_1) \\ j\dfrac{1}{Z_0}\sin(\theta_1) & \cos(\theta_1) \end{bmatrix}\begin{bmatrix} \cos(\theta_2) & jZ_0\sin(\theta_2) \\ j\dfrac{1}{Z_0}\sin(\theta_2) & \cos(\theta_2) \end{bmatrix}\begin{bmatrix} \cos(\theta_1) & jZ_0\sin(\theta_1) \\ j\dfrac{1}{Z_0}\sin(\theta_1) & \cos(\theta_1) \end{bmatrix} \tag{10-2}$$

En utilisant des équations (9-1) et (9-2), on peut obtenir la relation entre θ_0, θ_1 and θ_2 comme suit

$$\cos(\theta_2) = \frac{\cos(\theta_0)(1-K^2\tan^2(\theta_1)) + \dfrac{1}{M}\sin(\theta_0)(1+K^2)\tan(\theta_1)}{1+K^2\tan^2(\theta_1)} \tag{10-3}$$

où M et K sont définies comme suit

$$M = \frac{Z_1}{Z_0}, K = \frac{Z_1}{Z_2} \tag{10-4}$$

En fin, on peut définir le rapport de $(\theta_1+\theta_2)/\theta_0$ comme le facteur de miniaturisation

$$\gamma = \frac{2\theta_1 + \theta_2}{\theta} \tag{10-5}$$

Fig. 10.3 présente trace le facteur de miniaturisation pour différentes valeurs de M et K (pour $\theta_0 = \lambda/10$).
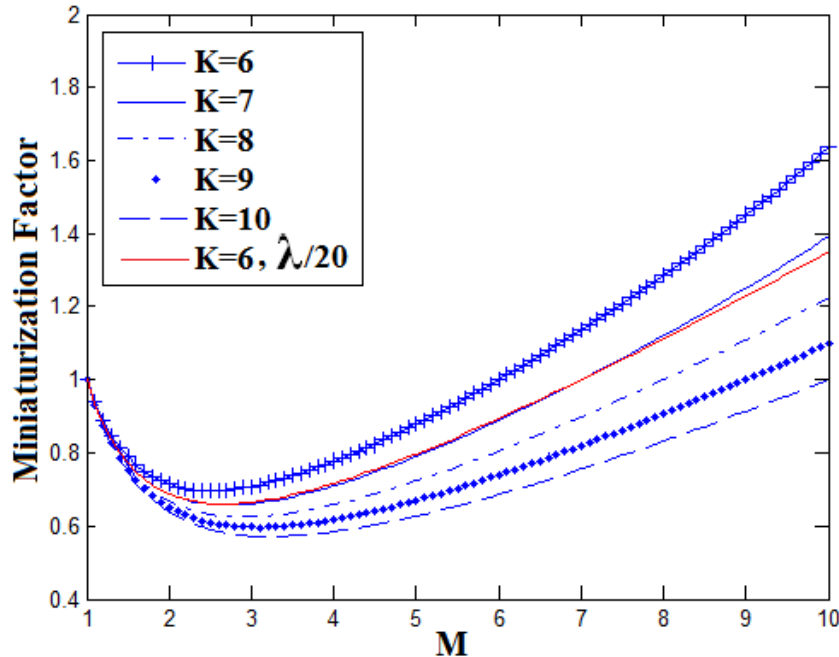
Fig. 10.3. Facteur de miniaturisation pour les différentes valeurs de M et K.

10.2.2. Le rôle de l'impédance caractéristique

Dans les calculs effectués dans la section précédente, on a utilisé l'impédance caractéristique d'une ligne microruban pour une petite section d'une cellule métamatérial. Mais, il faut faire attention qu'on a besoin de deux conducteurs pour definir l'impédance caractéristique. Par conséquent, on peut utiliser cette méthode pour une cellule qui est composée de deux conducteurs imprimés sur les couches supérieure et inférieure d'un substrat. Ce cas est similaire à un type de ligne de transmission appelé ruban-jumelé (paired-strip) qui est montré en Fig. 10.4.
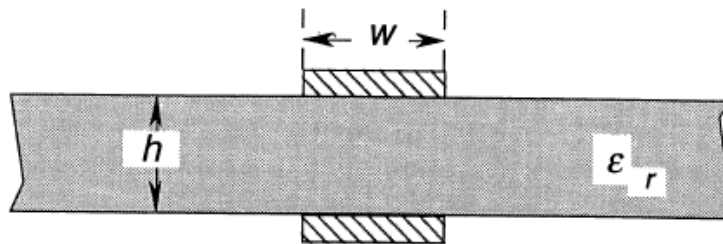
Fig. 10.4. Ligne de transmission ruban-jumelé (paired-strip).

L'impédance caractéristique d'une ligne ruban-jumellée est exprimée par la formule suivante:

$$Z_0 = \begin{cases} \dfrac{\eta_0}{\sqrt{\varepsilon_r}}\{\dfrac{a}{b}+\dfrac{1}{\pi}\ln 4+\dfrac{\varepsilon_r+1}{2\pi\varepsilon_r}\ln[\dfrac{\pi e(\dfrac{a}{b}+0.94)}{2}]+\dfrac{\varepsilon_r-1}{2\pi\varepsilon_r^2}\ln\dfrac{e\pi^2}{16}\}^{-1} & (a/b)>1 \\[4mm] \dfrac{\eta_0}{\pi\sqrt{\varepsilon_r}}\{\ln\dfrac{4b}{a}+\dfrac{1}{8}(\dfrac{a}{b})^2-\dfrac{\varepsilon_r-1}{2(\varepsilon_r+1)}(\ln\dfrac{\pi}{2}+\dfrac{\ln\dfrac{4}{\pi}}{\varepsilon_r})\} & (a/b)<1 \end{cases} \quad (10\text{-}6)$$

où $\eta 0$ est l'impédance caractérist la permittivité du substrat ique de l'air ($\approx 377\ \Omega$), εr est la permittivité du substrat, le paramètre *a* est égal à largeur du conducteur divisée par deux ($a=w/2$) et le paramètre *b* est égal à l'épaisseur de substrat divisée par deux ($b=h/2$).

Pour utiliser la ligne ruban-jumelé pour calculer l'impédance caractéristique d'une section d'une cellule métamatérial, il faut assurer que le comportement de son impédance caractéristique est identique à une ligne microruban.
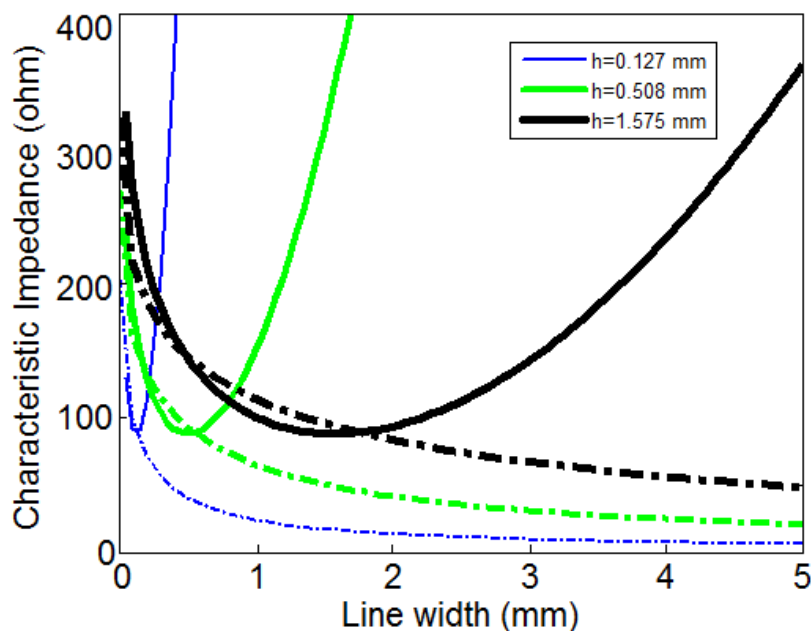
Fig. 10.5. Impédance caractéristique de la ligne ruban-jumellée (ligne continue) par rapport à microruban (ligne pointillée).

Fig. 10.5 compare l'impédance caractéristique d'une ligne ruban-jumellée à une ligne microruban. Selon cette figure, on peut dire que pour les lignes très étroites les deux structures ont la même impédance caractéristique, mais quand l'épaisseur du substrat est augmenté on peut voir que les lignes de transmission ont les mêmes impédances caractéristiques même à des largeurs de ligne plus élevées. Par exemple, lorsque l'épaisseur du substrat est de h = 1.575 mm, l'impédance caractéristique est presque la

même pour les deux structures jusqu'à la largeur de 2 mm. En d'autres termes, on peut conclure de la Fig. 10.5 que si un substrat assez épais et une ligne assez étroite sont utilisés, les deux courbes sont presque la même.

10.2.3. Effet des modes supérieurs

Un autre problème qui doit être pris en compte est l'effet des modes d'ordre supérieur. En fait, le modèle de matrice de ABCD pour une ligne de transmission est basée sur l'approximation mono-mode. Dans cette section, on étudie les conditions qui devaient être remplies sur le rapport d'impédance (le paramètre K) pour que l'approximation mono-mode soit valide.
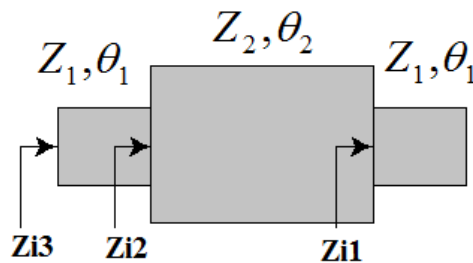
Fig. 10.6. Résonateur à impédance échelonnée.

L'effet de la technique de l'impédance échelonnée sur une structure rectangulaire est montré dans Fig. 10.6 où on peut trouver deux résonances vues de Z_{i1} et Z_{i2}. Deux cas peuvent être imaginés pour la structure de Fig. 10.6, qui sont un stub en court-circuit et un stub en circuit ouvert. Chaque cas est étudié en écrivant la condition de résonance comme suit.

10.2.3.1. Le stub à court-circuit

Quand le stub de la Fig. 9.6 est terminé par un court-circuit, on a

$$Z_{i1} = jZ_1 \tan(\theta_1) \qquad (10\text{-}7)$$

La première résonance se produit à Z_{i2} comme

$$Z_{i2} = Z_2 \frac{Z_{i1} + jZ_2 \tan(\theta_2)}{Z_2 + jZ_{i1} \tan(\theta_2)} \qquad (10\text{-}8)$$

On peut substituer Z_{i1} de l'équation (10-7) dans l'équation (10-8) et avoir

$$Z_{i2} = Z_2 \frac{[jZ_1 \tan(\theta_1)] + jZ_2 \tan(\theta_2)}{Z_2 + j[jZ_1 \tan(\theta_1)] \tan(\theta_2)} \qquad (10\text{-}9)$$

où

$$Z_{i2} = Z_2 \frac{[jZ_1 \tan(\theta_1)] + jZ_2 \tan(\theta_2)}{Z_2 - Z_1 \tan(\theta_1) \tan(\theta_2)} \tag{10-10}$$

En mettant le dénominateur de (10-10) égal à zéro, on peut avoir la condition pour la première résonance comme suit

$$\frac{Z_2}{Z_1} = \tan(\theta_1) \tan(\theta_2) \tag{10-11}$$

Pour la deuxième résonance, on a

$$Z_{i3} = Z_1 \frac{Z_{i2} + jZ_1 \tan(\theta_1)}{Z_1 + jZ_{i2} \tan(\theta_1)} \tag{10-12}$$

En substituant Z_{i2} de l'équation (10-10), on va obtenir

$$Z_{i3} = Z_1 \frac{Z_1 \dfrac{j[Z_1 \tan(\theta_1) + Z_2 \tan(\theta_2)]}{Z_2 - Z_1 \tan(\theta_1) \tan(\theta_2)} + jZ_1 \tan(\theta_1)}{Z_1 + j \times Z_1 \dfrac{j[Z_1 \tan(\theta_1) + Z_2 \tan(\theta_2)]}{Z_2 - Z_1 \tan(\theta_1) \tan(\theta_2)} \times \tan(\theta_1)} \tag{10-13}$$

La condition pour la deuxième résonance peut être calculée en mettant le dénominateur de l'équation (10-13) égale à zéro comme suit

$$Z_1 Z_2 - Z_1^2 \tan(\theta_1) \tan(\theta_2) = Z_1^2 \tan^2(\theta_1) + Z_1 Z_2 \tan(\theta_1) \tan(\theta_2) \tag{10-14}$$

L'équation (10-14) peut être simplifiée comme

$$\frac{Z_2}{Z_1} = \frac{\tan(\theta_1)[\tan(\theta_1) + \tan(\theta_2)]}{1 - \tan(\theta_1) \tan(\theta_2)} \tag{10-15}$$

En mettant toutes les longueurs égales dans l'équation. (10-11) et (10-15), la condition finale pour la première résonance est

$$\frac{1}{K} = \frac{Z_2}{Z_1} = \tan^2(\theta) \tag{10-16}$$

Pour mieux décider la distance entre le mode principal et le premier mode supérieur, on trace la fonction θ=atan(√1/K) par rapport à *K* (en échelle logarithmique) dans la Fig. 10. 7. Le premier mode est produit à $\theta_A=\theta-\pi$.
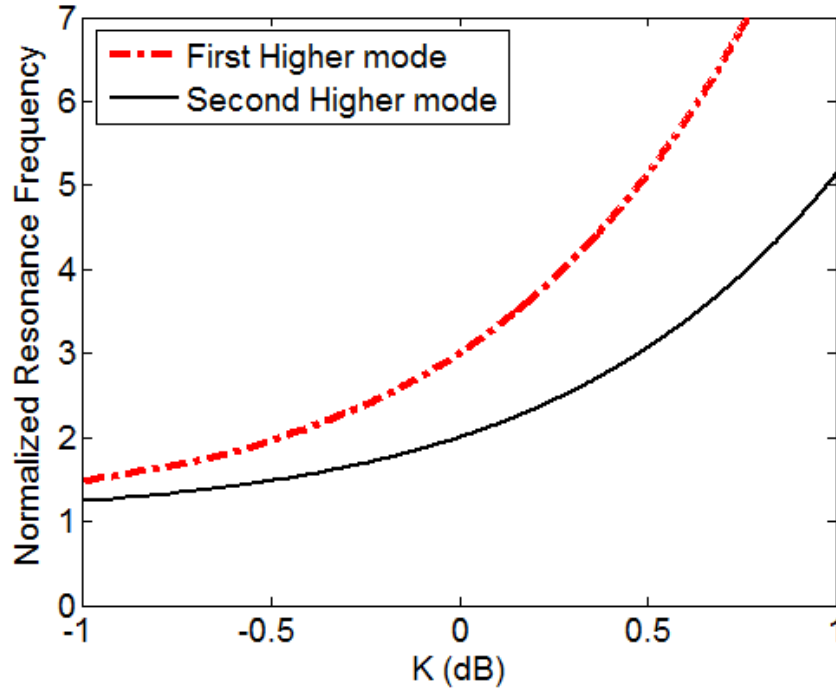
Fig. 10.7. Fréquence de résonance normalisée par rapport à *K* dans le cas de court circuit.

Selon Fig. 10.7, on peut dire que si *K*>1, la distance entre le mode principal et le mode supérieur est plus que 1 dans l'échelle de la fréquence normalisée, et l'approximation mono-mode est valide pour utiliser la technique de résonateur à impédance échelonnée. Pour calculer la deuxième condition de résonance, on peut utiliser équation (10-15) avec les mêmes θ.

$$\frac{1}{K}=\frac{Z_2}{Z_1}=\frac{2\tan^2(\theta)}{1-\tan^2(\theta)} \tag{10-17}$$

Comme le cas précédent, pour déterminer la distanse entre les mode, on trace θ par rapport à *K* dans la Fig. 10.8.
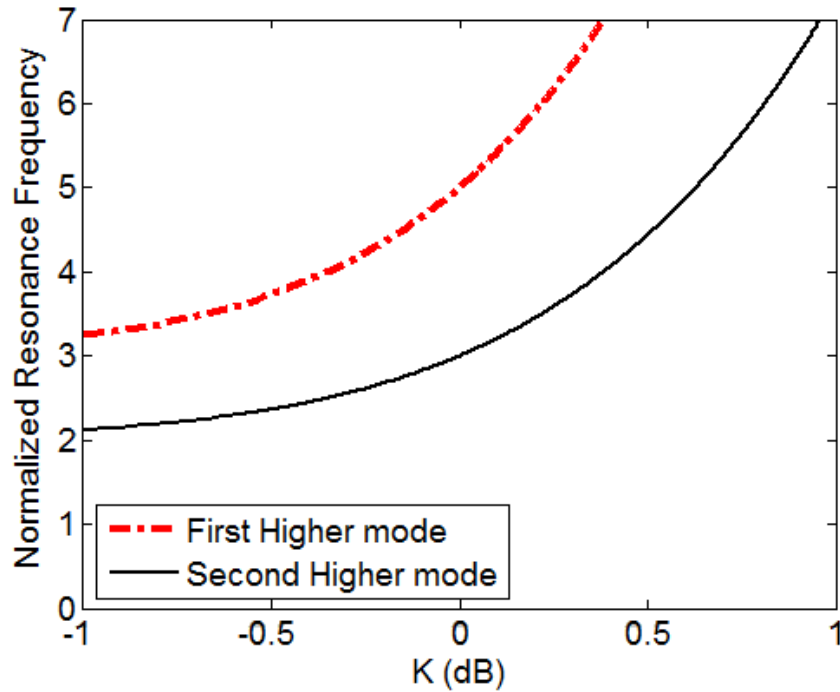
Fig. 10.8. Fréquence de résonance normalisée par rapport à *K* dans le cas courte circuit.

10.2.3.2. Le stub à circuit ouvert

Dans cette section, on étudie le deuxième cas possible (circuit ouvert) pour le stub montré dans la Fig. 10.6. Quand le stub se termine par un circuit ouvert, on peut écrire Z_{i1} comme

$$Z_{i1} = \frac{Z_1}{j\tan(\theta_1)} \qquad (10\text{-}18)$$

et pour la première résonance à Z_{i2}

$$Z_{i2} = \frac{Z_2}{j}\frac{Z_1 - Z_2\tan(\theta_2)\tan(\theta_1)}{Z_2\tan(\theta_1) + Z_1\tan(\theta_2)} \qquad (10\text{-}19)$$

En mettant le dénominateur de (10-19) égal à zéro pour $\theta_1 = \theta_2 = \theta$, on obtient

$$(Z_1 + Z_2)\tan(\theta) = 0 \qquad (10\text{-}20)$$

Selon l'équation (10-20), la condition pour avoir la première résonance est $\tan(\theta) = 0$, ce qui n'est bien sûr pas acceptable. Pour la deuxième résonance vue de Z_{i3}, on peut écrire

$$Z_{i3} = \frac{Z_1}{j} \frac{Z_1 Z_2 - Z_2^2 \tan(\theta_1)\tan(\theta_2) - Z_1 Z_2 \tan^2(\theta_1) - Z_1^2 \tan(\theta_1)\tan(\theta_2)}{2 Z_1 Z_2 \tan(\theta_1) + Z_1^2 \tan(\theta_2) - Z_2^2 \tan(\theta_2)\tan^2(\theta_1)} \qquad (10\text{-}21)$$

Encore en mettant le dénominateur égal à zéro, on va avoir

$$(2Z_1 Z_2 + Z_1^2)\tan(\theta) - Z_2^2 \tan^3(\theta) = 0 \qquad (10\text{-}22)$$

ou

$$\theta = \tan^{-1}(\sqrt{2K + K^2}) \qquad (10\text{-}23)$$

Les deux premiers modes proches de la résonance principale sont représentés dans la Fig. 10.9 comme ci-dessous
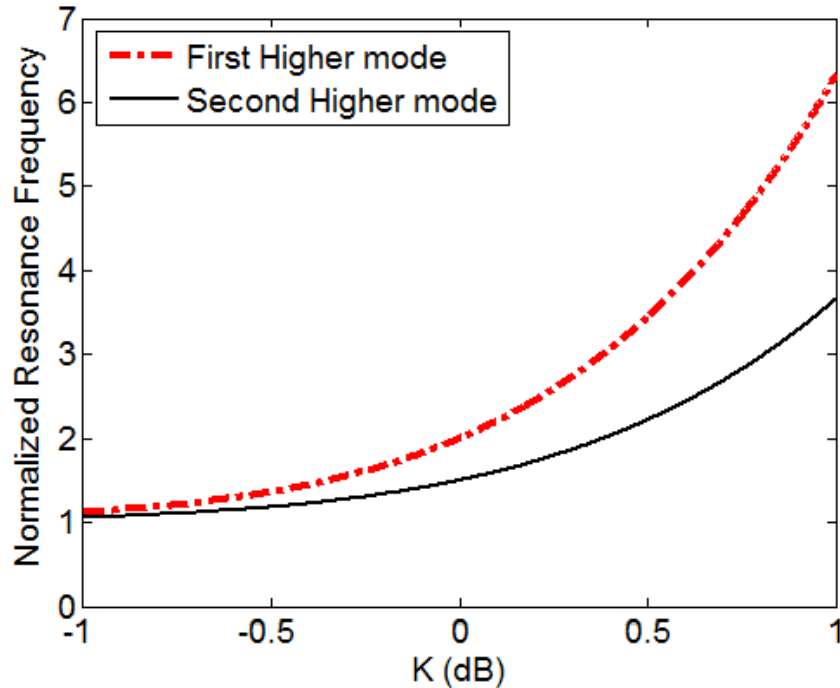
Fig. 10.9. Fréquence de résonance normalisée par rapport à K dans le cas circuit ouvert.

Selon la Fig. 10.9, le paramètre *K* doit être plus grand que 0.5 pour avoir assez de distance (1 dans l'échelle normalisée) entre les deux modes.

10.3. Conception de la cellule métamatériau

10.3.1. Les cellules avec des diodes idéales

La conception de la cellule est basée sur la similarité entre les structures DSR et spirale. En fait, comme représenté dans la Fig. 10.10, si on met les diodes DC-contrôlées dans la structure d'un DSR, on peut obtenir une spirale et aussi une autre structure que l'on appelle quasi-DSR.
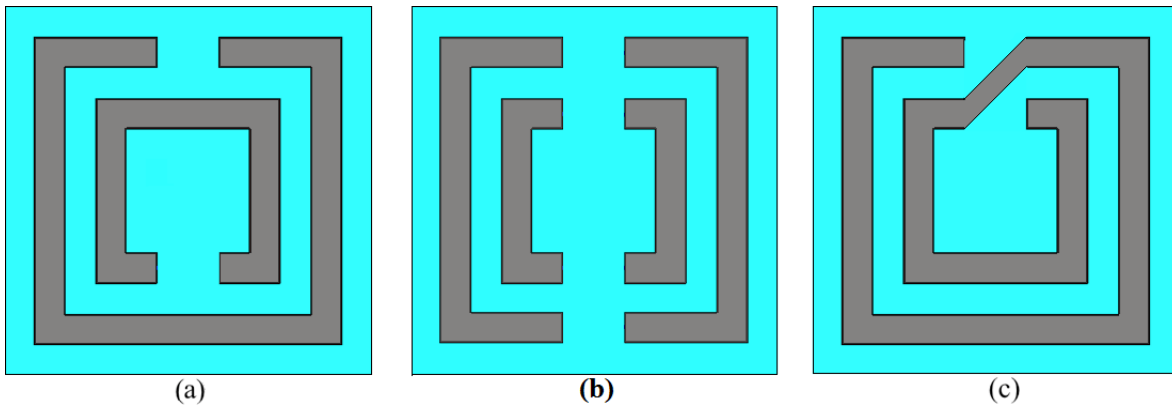
Fig. 10.10. Trois configurations possibles pour la cellule

Pour mieux comprendre le comportement de ces structures, ils sont d'abord simulées dans les conditions idéales où les diodes sont remplacées par des bandes métalliques quand elles sont ON, et par des circuits ouverts dans l'état OFF. Les résultats de simulation pour chaque configuration de cellule sont présentés dans les Figs 10.11-10.13.
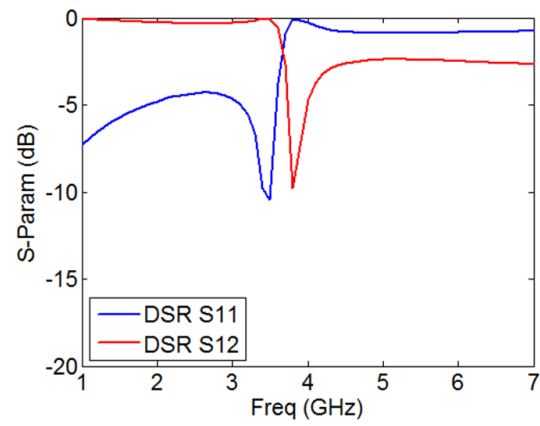
(a)
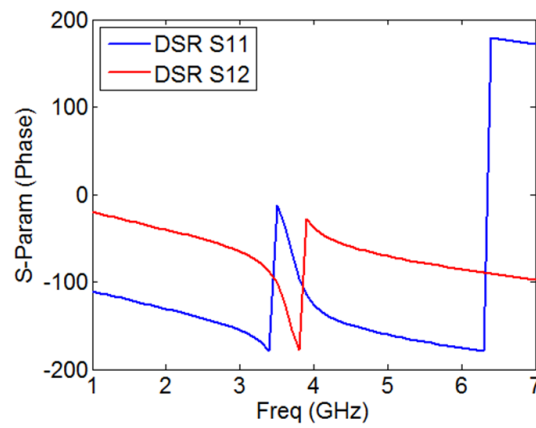
(b)
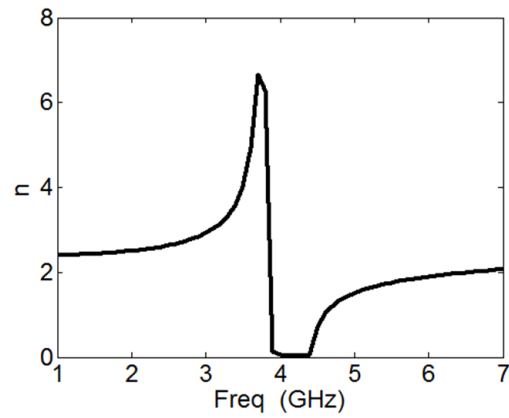
(c)

Fig. 10.11. Paramètres simulés pour la cellule DSR idéale.
(a,b) Paramètres S, (c) indice de réfraction.
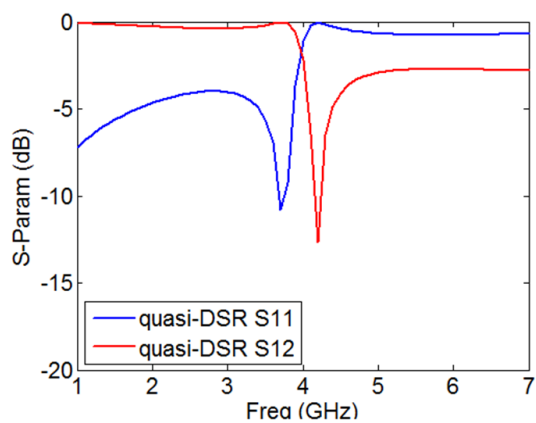
(a)
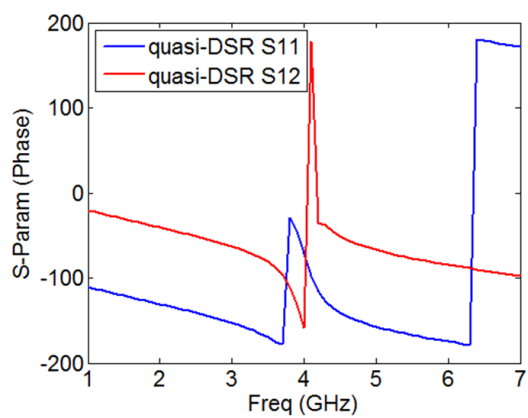
(b)
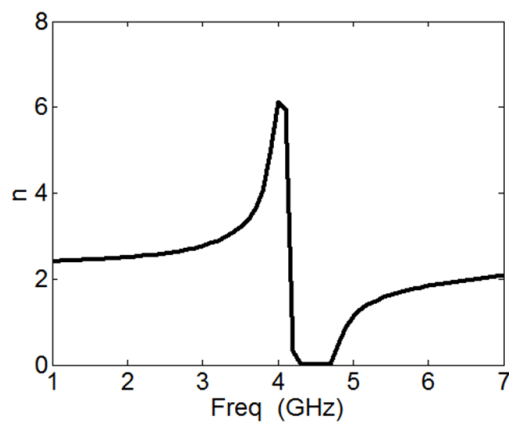
(c)

Fig. 10.12. Paramètres simulés pour la cellule quasi-DSR idéale.
(a,b) Paramètres S, (c) indice de réfraction.
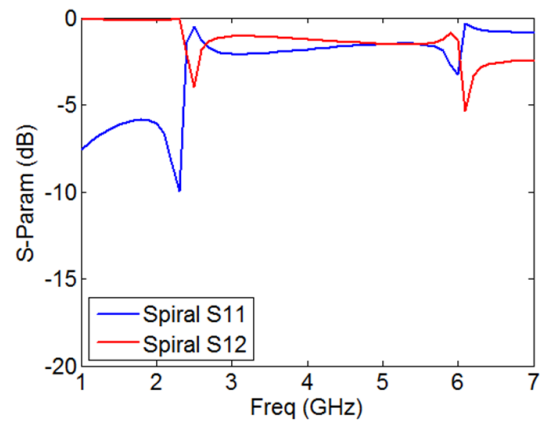
(a)
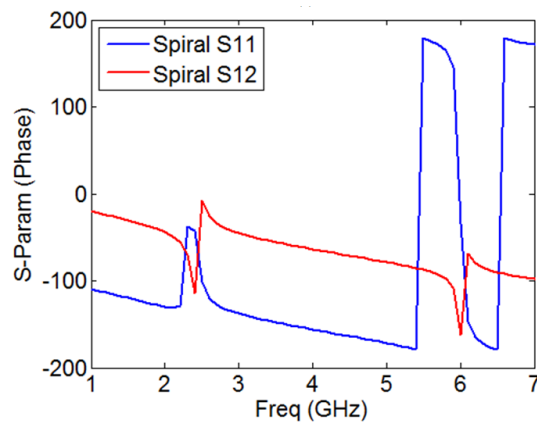
(b)
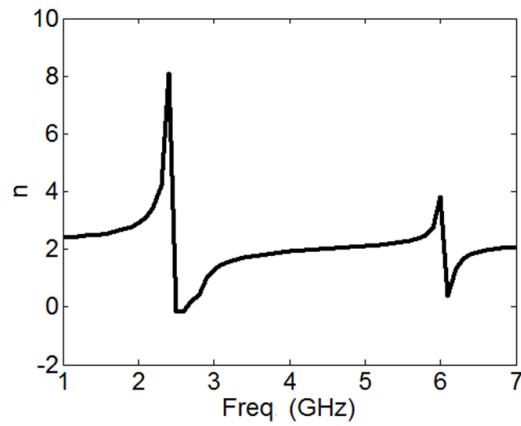
(c)

Fig. 10.13. Paramètres simulés pour la cellule spiral idéale.
(a,b) Paramètres S, (c) indice de réfraction.

Selon les Figs 10.11-10.13, les indices de réfraction des cellules DSR et quasi-DSR suivent la même règle, et la seule différence est un léger décalage de fréquence. Mais dans la configuration spirale, nous avons deux résonances dans l'indice de réfraction et le décalage de fréquence est presque deux fois plus que pour les deux configurations précédentes.
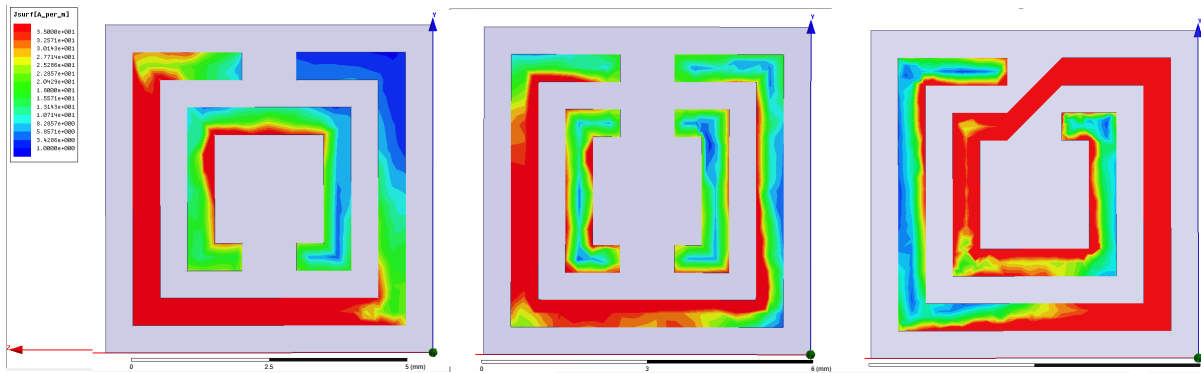
Fig. 10.14. Distribution du courant sur les cellules idéales.

Fig. 10.14 confirme ces comportements en montrant que les distributions de courant de DSR et quasi-DSR sont presque les mêmes, mais pour la spirale, le courant total est le plus grand, et par conséquent, elle a la plus basse fréquence de résonance. Pour vérifier les résultats de la simulation, on a fabriqué un tableau 3D de chaque cellule comme montré dans la Fig. 10.15.
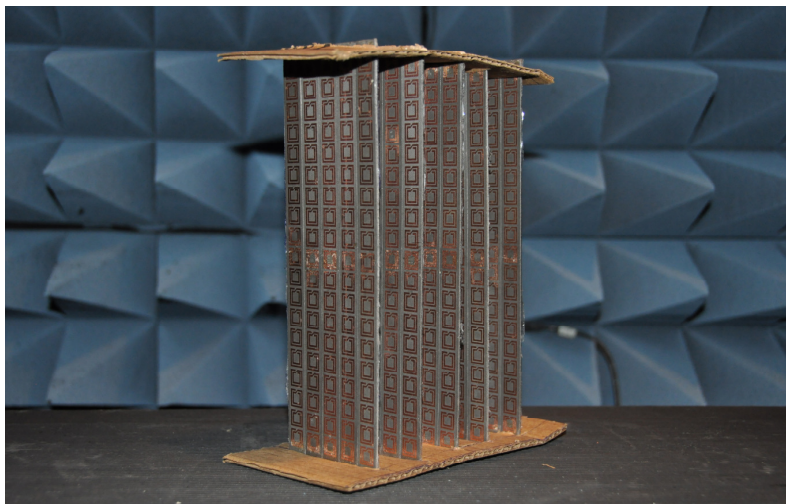
(a)
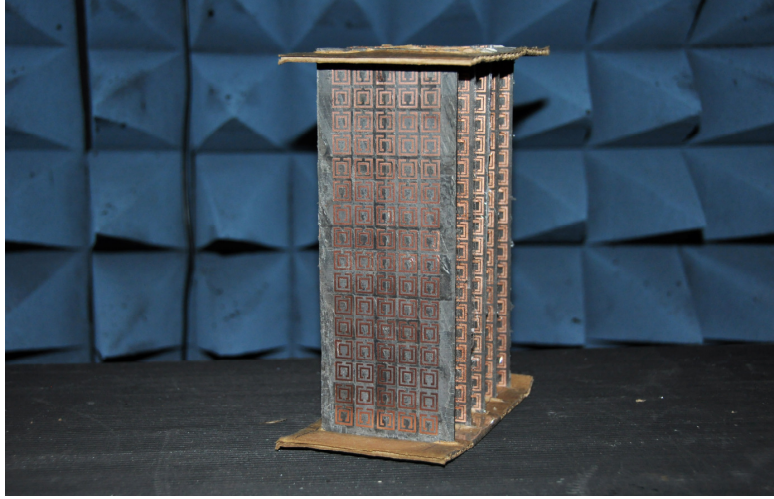
(b)

Fig. 10.15. Le prototype 3D fabriqué pour (a) Spiral et (b) DSR.

On a mesuré les paramètres S de chaque prototype en utilisant la méthode de mesure en espace libre et les résultats de mesure sont présentés dans la Figure 10.16.
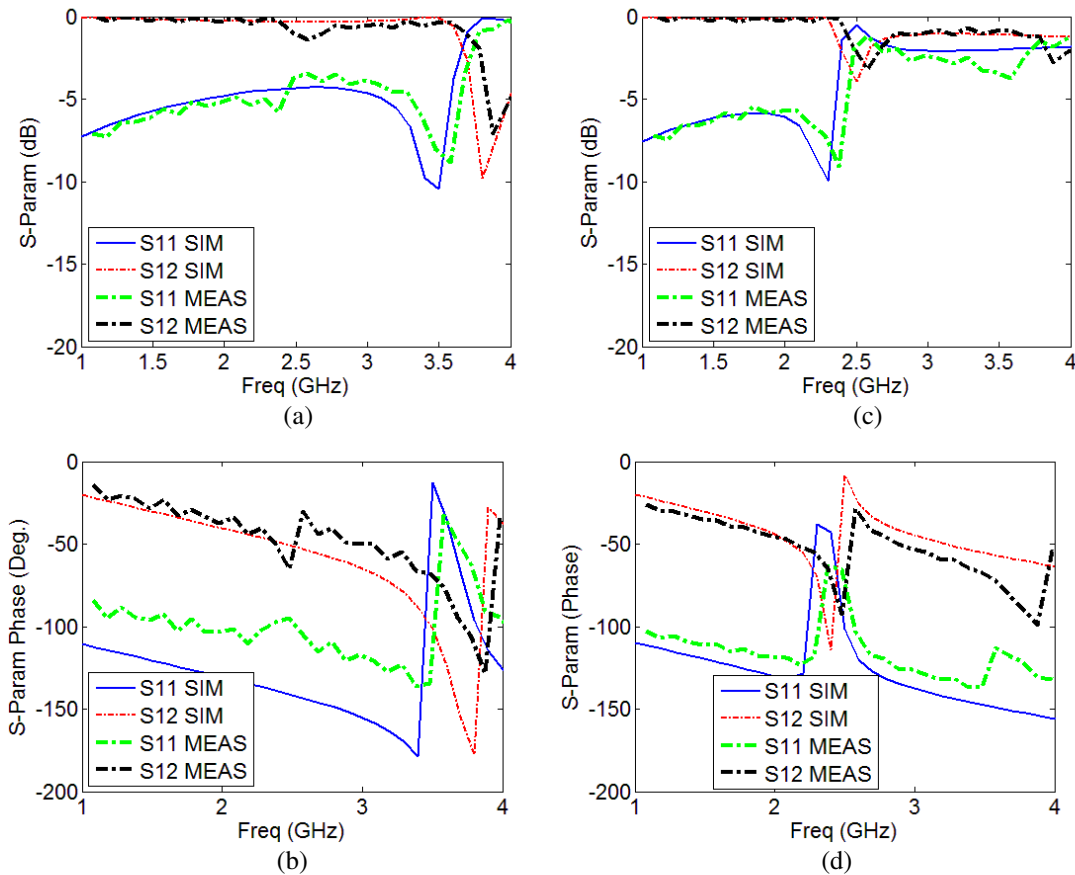
Fig. 10.16. Résultats mesurés pour les cellules non-reconfigurables.
(a),(b): DSR magnitude et phase. (c),(d): Spiral magnitude et phase.

Comme prévu, il y a un très bon accord entre la simulation et l'expérimentation, parce que nous avons utilisé de grands prototypes 3D et une lentille diélectrique pour concentrer le faisceau sur eux.

10.3.2. Les cellules avec les diodes réelles

Dans cette thèse, on a utilisé la diode GMP4201 pour contrôller la configuration de la cellule comme représenté dans la Fig. 10.17.
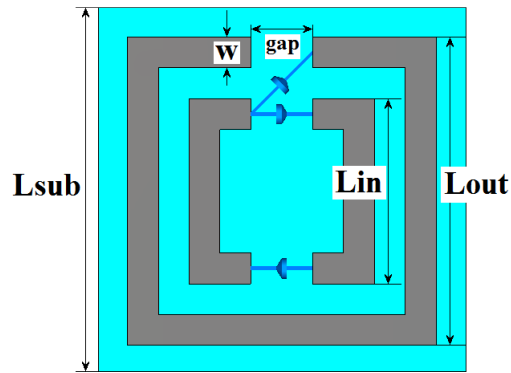
Fig. 10.17. Structure de la cellule avec les diodes

Pour polariser les diodes, on utilise un réseau d'alimentation comme montré dans la Fig. 10.18.
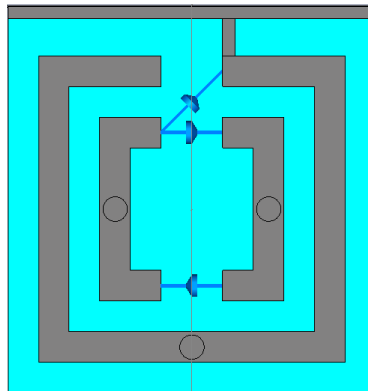
Fig. 10.18. Réseau d'alimentation d'une cellule.

On a utilisé la méthode de mesure en espace libre pour mesurer les paramètres S des cellules métamatériau. Dans ce procédé, le prototype métamatériau est placé entre deux antennes cornets et deux lentilles diélectriques sont utilisées pour concentrer le faisceau de l'antenne cornet sur les cellules métamatériaux. Fig. 10.19 montre le prototype fabriqué, et les résultats de mesure sont représentés sur la Fig. 10.20.
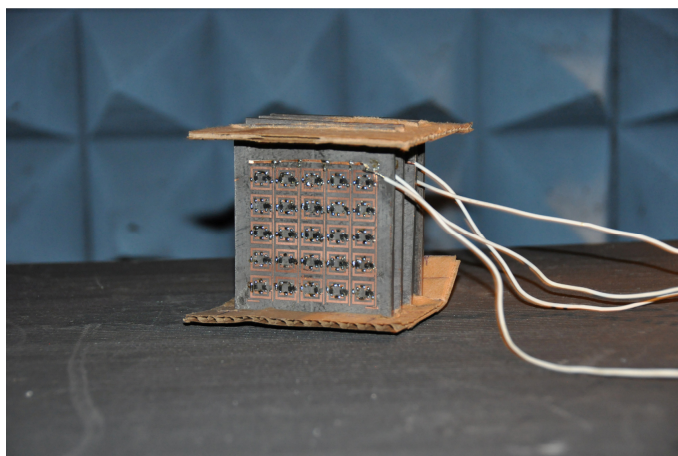
Fig. 10.19. Les cellules reconfigurables fabriqués
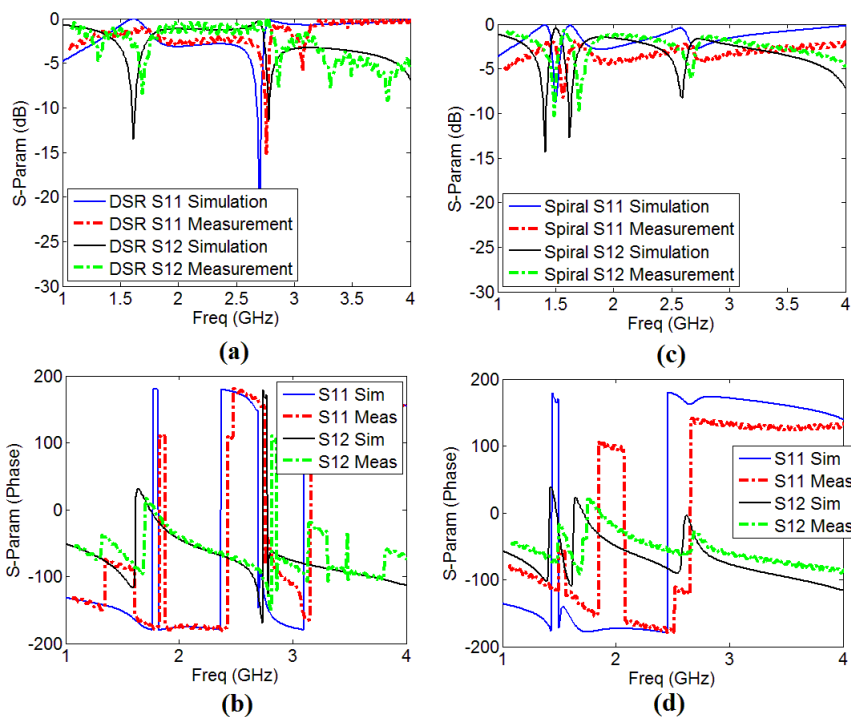
Fig. 10.20. Les paramètres mesurés des cellules reconfigurables.
(a),(b): DSR magnitude et phase.
(c),(d): Spiral magnitude et phase.

10.4. Antenne reconfigurable à bande S

Pour montrer la capacité de notre méthode du permutation de faisceau, nous l'avons mis sur une antenne planaire fonctionnant à la bande de fréquence S. Fig. 10.21 montre la vue schématique de cette antenne sans les cellules métamatériaux.

(a)   (b)
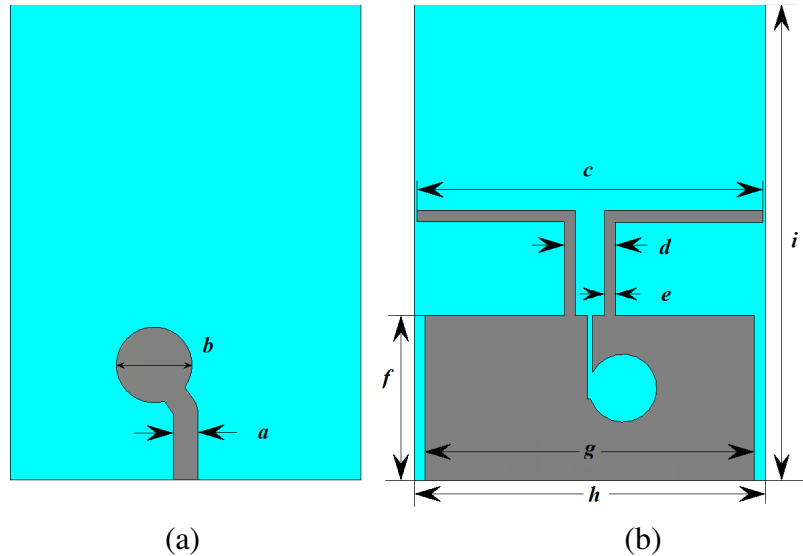
Fig. 10.21. Antenne sans les cellules métamatériaux.
(*a=4.5, b=14, c=63, d=9.4, e=2, f=30, g=60, h=64, i=77 mm*)

L'antenne représentée dans la Fig. 10.21 est chargée avec un réseau de cellules reconfigurables, montrées dans la Fig. 10.13. Le résultat de cette conception est représenté dans la Fig. 10.22.

(a)
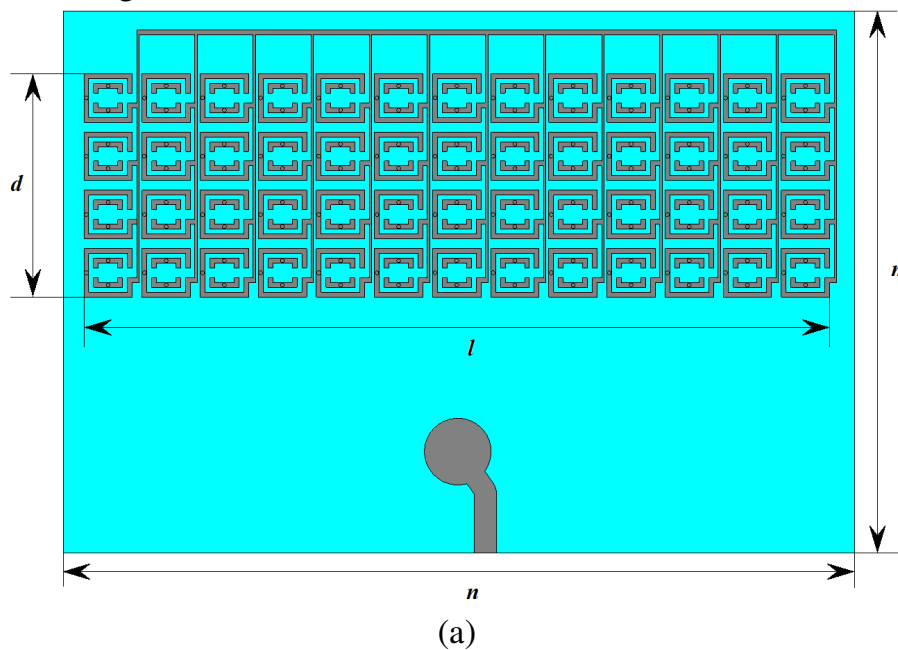
(b)

Fig. 10.22. Antenne avec les cellules reconfigurables (*d=46, l=154, m*=112, *n*=163).

On peut contrôler les diodes avec une source externe de tension continue. De cette façon, lorsque les cellules sur le côté gauche de l'élément de rayonnement sont définies comme des spirales, le faisceau est incliné dans le plan E en direction du côté gauche. Fig. 10.23 montre le diagramme de rayonnement de l'antenne dans cette condition.
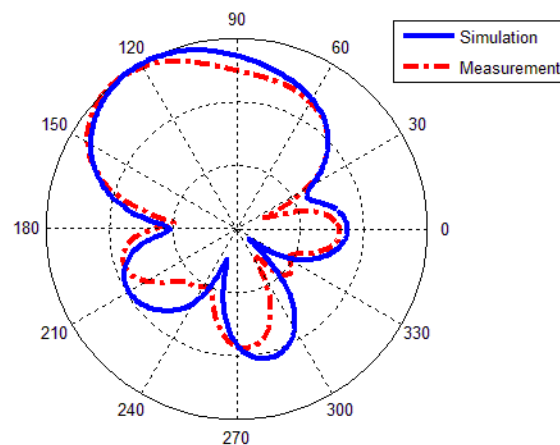
(a)
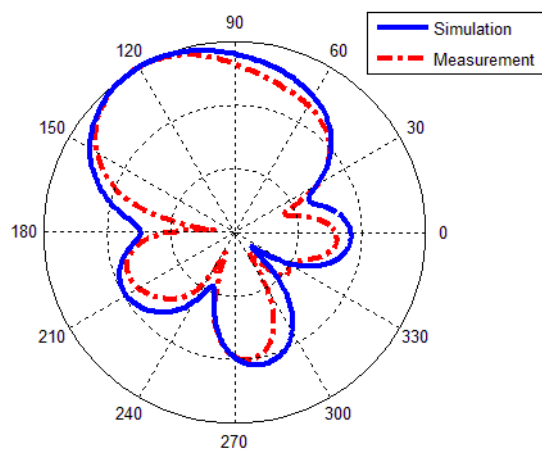
(b)
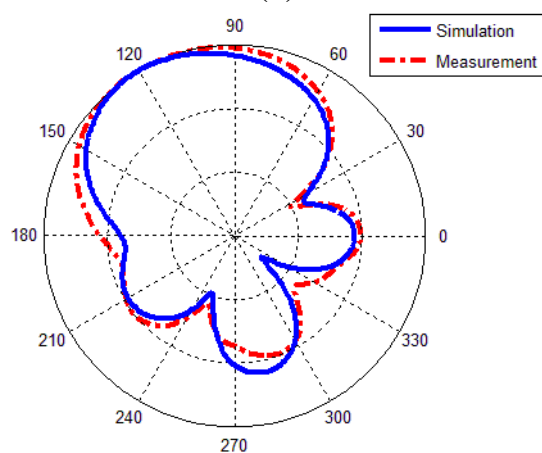
(c)
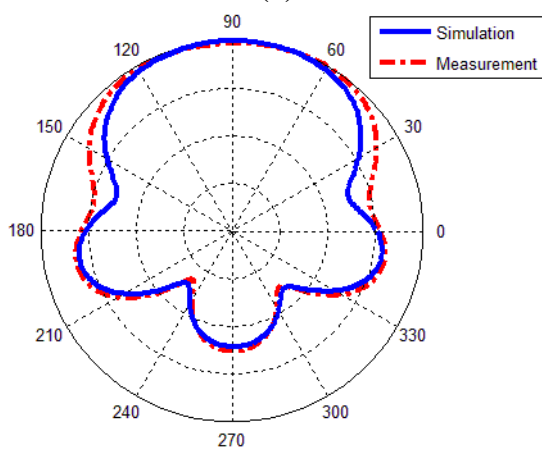
(d)

Fig. 10.23. Diagramme de rayonnement normalisé de l'antenne dans le plan E à: (a) 2,8 GHz, (b) 3 GHz, et (c) 3.2 GH, et (d) dans le plan H à 3 GHz.

On peut éxpliquer la déviation du faisceau obtenu à l'aide des cellules métamatériaux en utilisant la théorie développée dans la section 7.2. Selon cette théorie, lorsque l'onde électromagnétique pénètre dans le milieu métamatériau avec deux sections, comme montré dans la Fig. 10.24, la différence entre les indices de réfraction des sections conduit à une différence de phase et donc un angle de déviation de $\varphi = sin^{-1}[d\,(n2-n1)]/l$.

$$\beta_1 = k_0 n_1 d \qquad \beta_2 = k_0 n_2 d$$

| n1 | n2 | d |

l

●
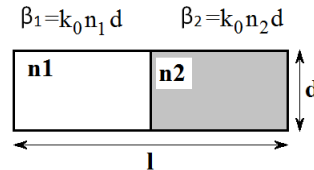
Fig. 10.24. Mécanisme de déviation du faisceau.

Dans notre structure $d=46$, $l=154$, et n_2-$n_1 \approx 1.3$, donc on peut attendre un angle de déviation de 23°. Il importe de mentionner que le réseau des cellules métamatériau ne modifie pas l'adaptation d'antenne sur la bande d'opération comme montré dans la Fig. 10.25.
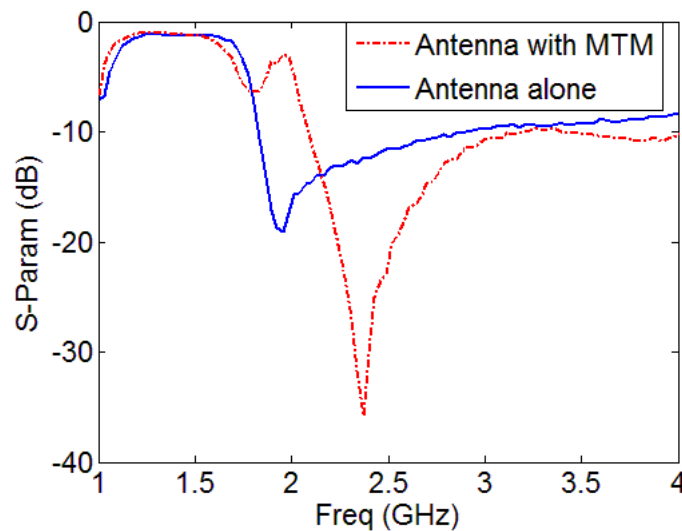
Fig. 10.25. Coefficient de réflexion de l'antenne avec et sans des cellules métamatériaux.

10.5. Antenne avec les cellules SIR

Dans cettte section, on utilise la technique impédance échelonnée pour reduir la taille de la structure. Pour samplifier le probleme, seulement les celulles sans les diodes sont utilisées comme montré dans la Fig. 10.26.

(a)

(b)
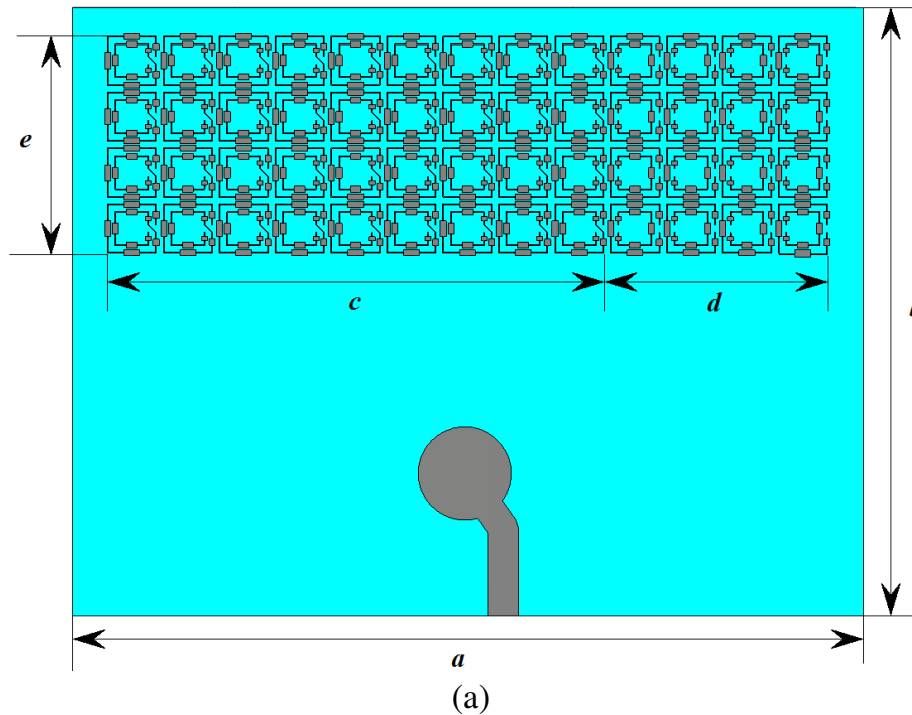
Fig. 10.26. Antenne avec les cellules miniaturisées (*a=116, b=89, c*=65, d=40, e=32 mm).

Le diagramme de rayonnement et coefficient de réflexion de cette antenne sont tracées dans la Fig. 10.27.

(a)

(b)

(c)
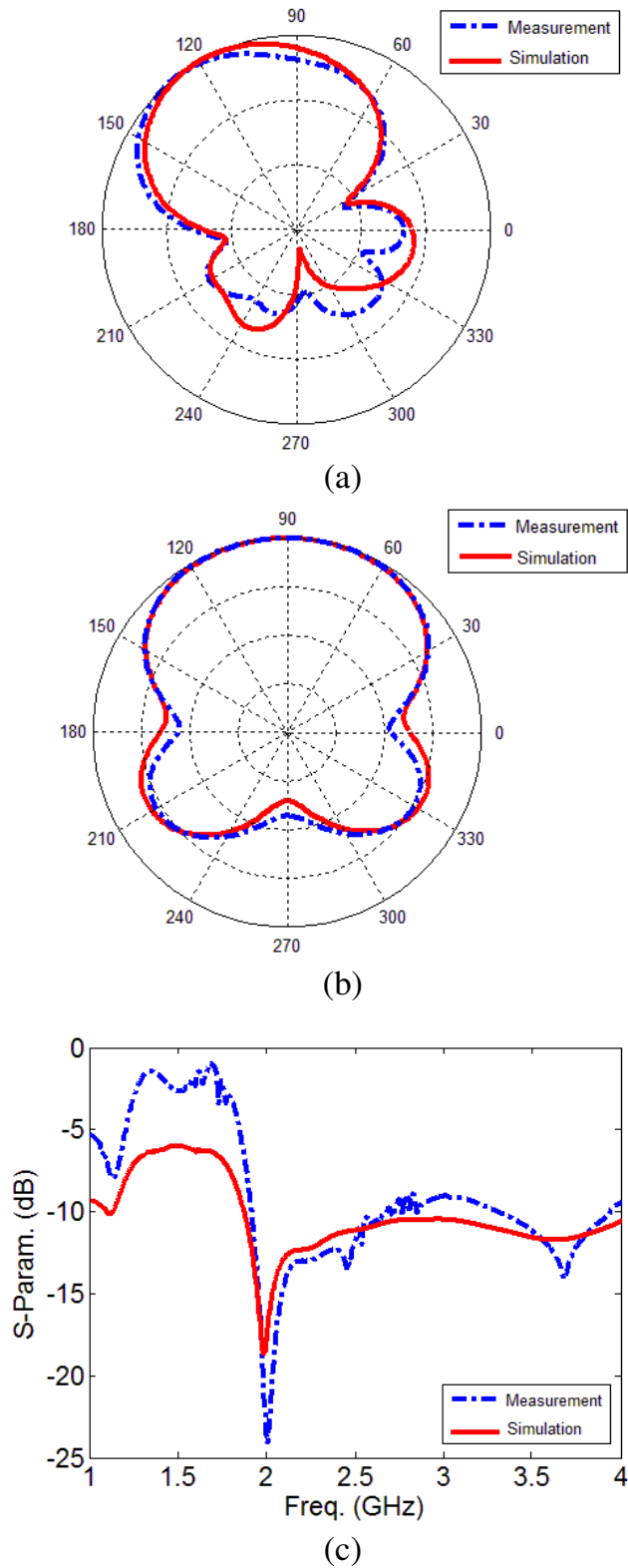
Fig. 10.27. Diagramme de rayonnement et coefficient de réflexion de l'antenne avec les cellules miniaturisées.

Selon Fig. 10.27, on peut obtenir la même déviation du faisceau que l'antenne de la Fig. 10.22, mais la taille de la structure et 30% plus petite.

10.6. Antenne en métamatériaux aux ondes millimétriques

La structure de l'antenne aux ondes millimétriques est représentée dans la Fig. 10.28.

(a)   (b)
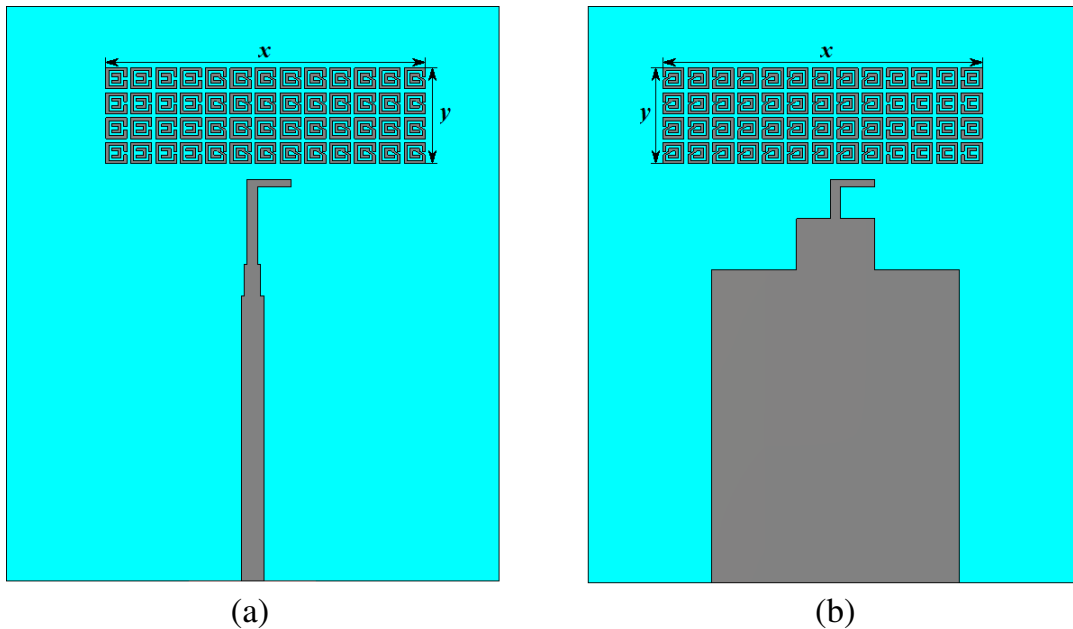
Fig. 10.28. Structure de l'antenne aux ondes millimétriques.

Il importe de mentionner qu'on n'a pas utilisé les diodes dans l'antenne aux ondes millimétriques, mais on a conçu un milieu métamatériau pour incliner le faiseau d'antenne en utilisant des cellules spirale et DSR comme répresenté dans la Fig. 10.29. Les paramètres S de ces cellules sont représentées dans la Fig. 10.30.
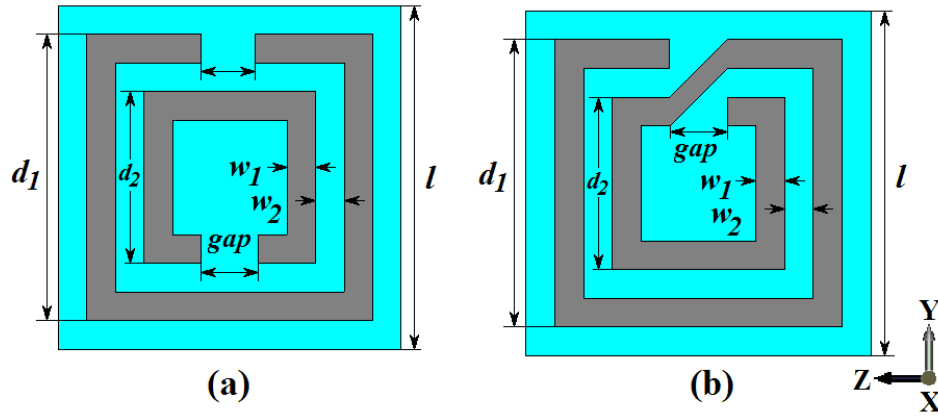
Fig. 10.29. Structure de cellule métamatériau aux ondes millimétriques.

(a)
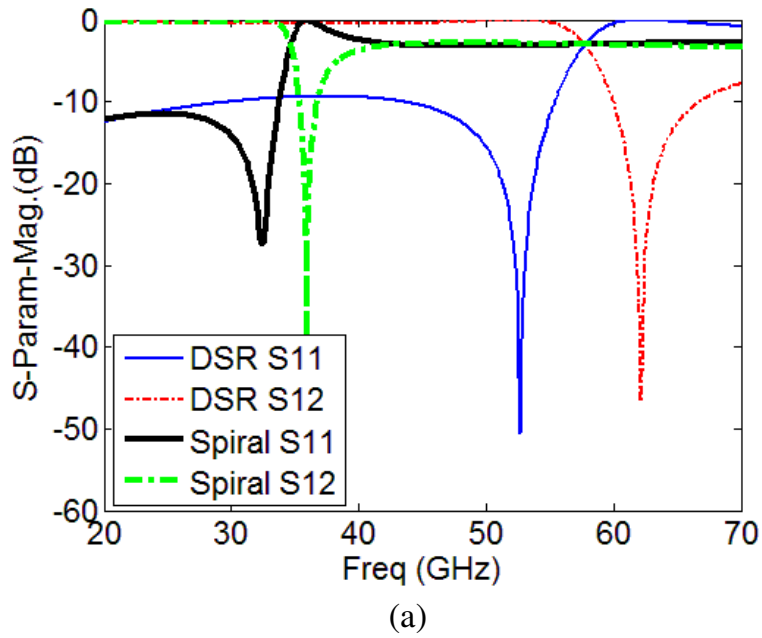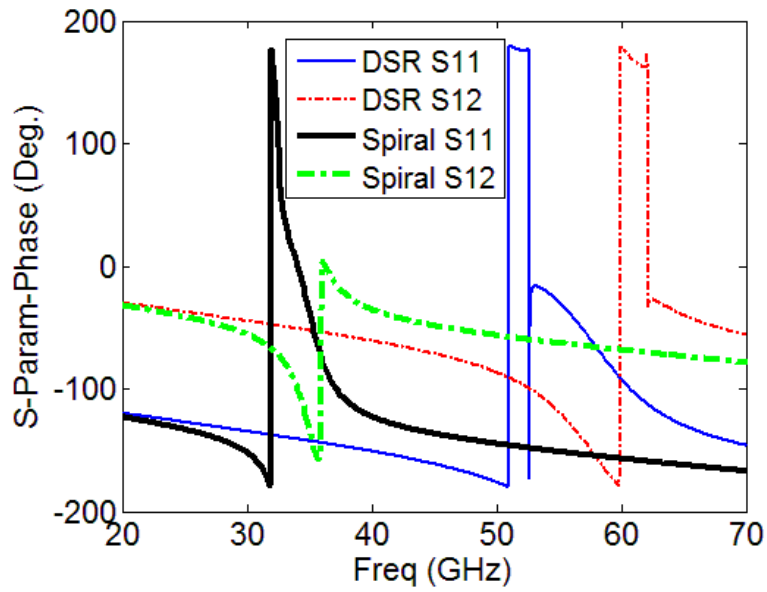
(b)

Fig. 10.30. Paramètres S des cellules aux ondes millimétriques.

L'indice de réfraction des cellules spirale et DSR (extrait des paramètres S) sont représentées dans la Fig. 10.31.

(a)

(b)
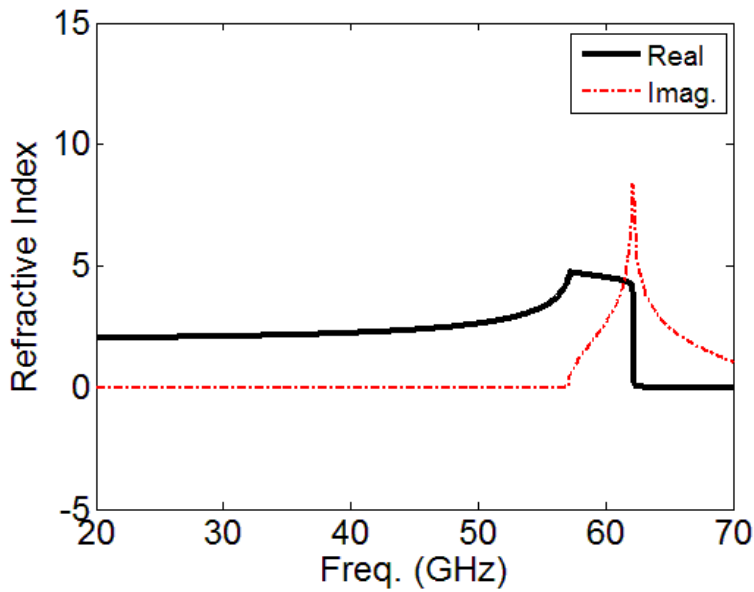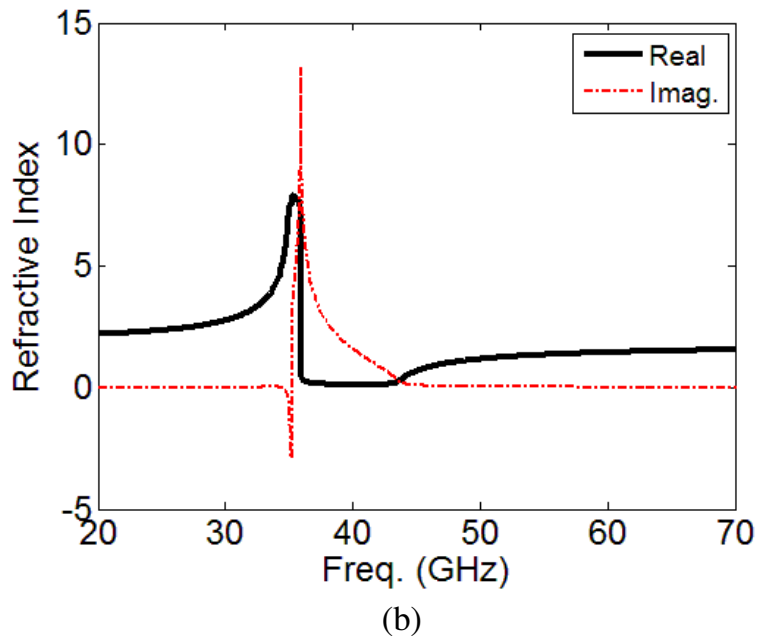
Fig. 10.31. Indice de réfraction de (a) DSR et (b) spirale.

Selon Fig. 10.31, on peut conclure qu'il existe une différence entre l'indice de réfraction de la spirale et DSR autour de 60 GHz. Cette différence est utilisé pour basculer le faisceau. Fig. 10.32 montre le diagramme de rayonnement de l'antenne qui confirme l'effet des cellules métamatériaux.
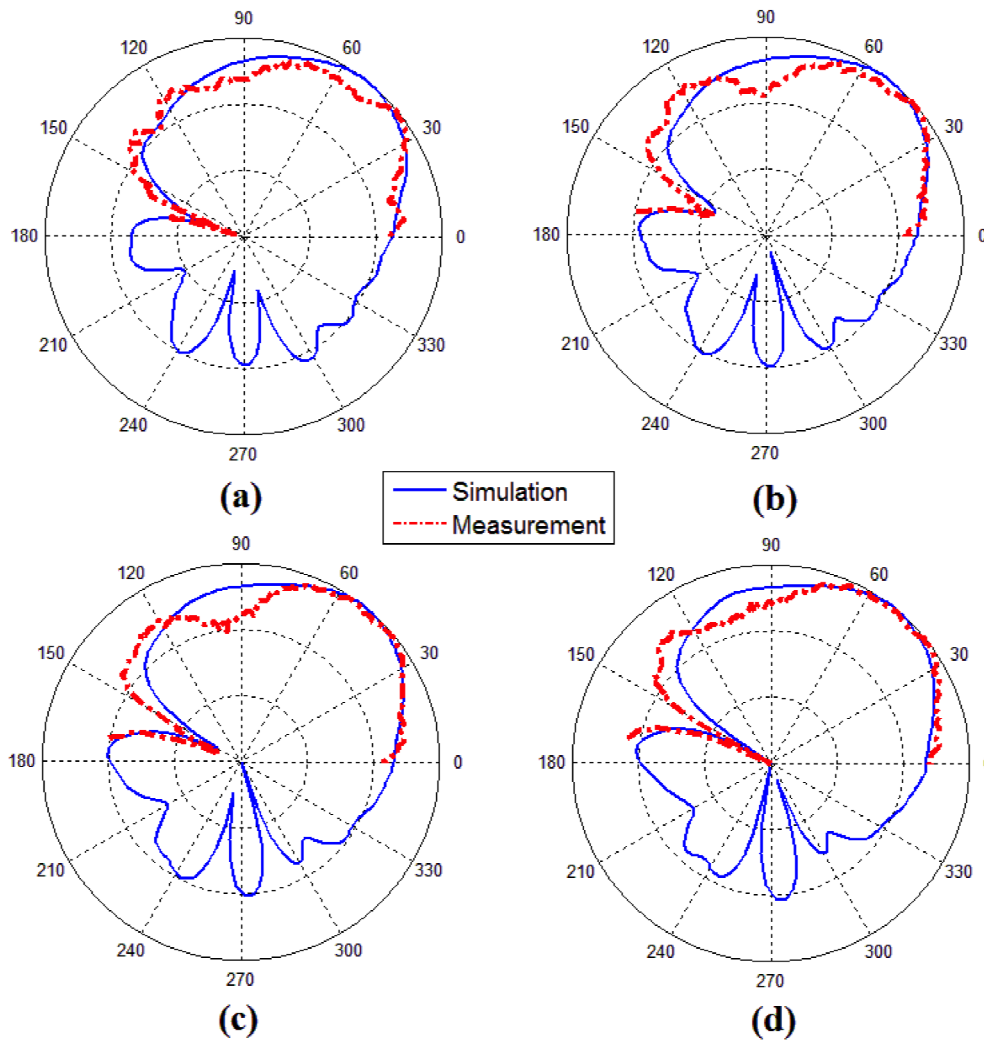
Fig. 10.32. Diagramme de rayonnement de l'antenne aux ondes millimétriques.

L'angle d'inclinaison est environ 32°, et il n'y a aucune perte de gain en utilisant cette méthode. En faite, comme montré dans la Tableau 10.1, il y a une amélioration de gain d'environ 2.4 dB.

Tableau 10.1. Améloration de gain.

Freq. (GHz)	60	61	62	63
Gain simulé (dB)	9.4	9.6	9.7	9.8
Gain measuré (dB)	8.9	9	9.2	9.6
Gain de dipôle sans cellules (dB)	7.4	7.6	7.7	7.8

Il est important de mentionner que le coefficient de réflexion reste inférieur à -10 dB comme tracer dans la Fig. 10.33.
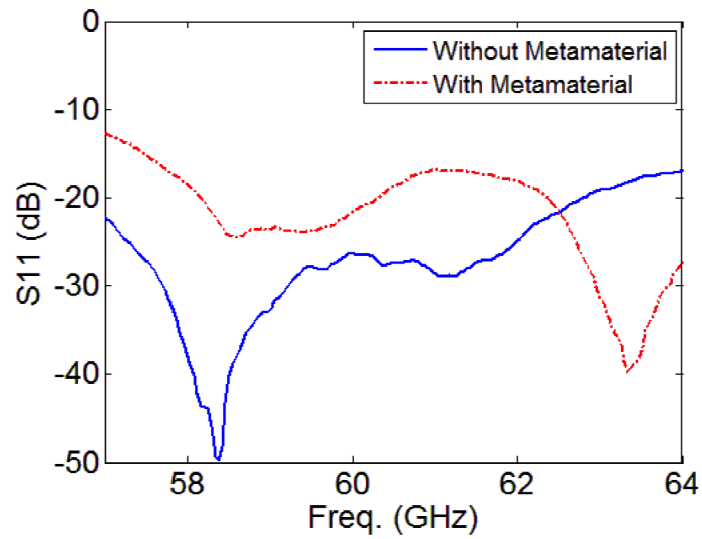
Fig. 10.33. Coefficient de réflexion de l'antenne avec et sans métamatérial.

Enfin, une photo de l'antenne fabriquée est représenté sur la Fig. 10. 34.

Fig. 10.34. Prototype fabriqué aux ondes millimétriques.

10.7. Lentille diélectrique

Dans cette section, on explique le processus de conception et de fabrication d'une lentille diélectrique fabriqué de la paraffine. Cette lentille a été utilisée dans les mesures des paramètres S des cellules métamatériaux conçues dans cette thèse.
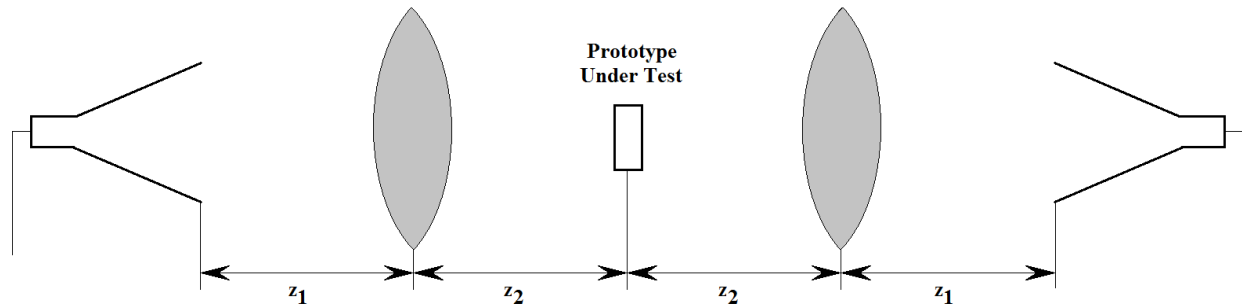
Fig. 10.35. Schéma de la méthode espace-libre pour mesurer les paramètres S des cellules métamatériaux.

Le diagramme schématique de la méthode espace-libre, qui est utilisée dans cette thèse, est montré dans la Fig. 10.35. Dans cette méthode, on a besoin de deux lentilles diélectriques pour concentrer les ondes sur le prototype. La matière qui est normalement utilisé pour fabriquer une lentille diélectrique est Rexolite. Cependant, le processus d'usinage requis pour matériau est très coûteux pour les dimensions associées aux applications dans les bandes C et S. De plus, la densité de Rexolite est 1.11 g/cc qui est relativement élevée et donc le montage de la structure devient difficile. Dans cette thèse, on a utilisé la paraffine et le processus de moulage comme une approche alternative pour la conception et la mise en œuvre de lentille. Cette matière a une permittivité de ε_r=2.55 qui est très proche de Rexolite, tandis que sa densité est d'environ 0.88 g /cc qui rend la structure environ 20% plus légere. Fig. 10.36 présente l'organigramme de la méthode conventionnelle et le procédé de moulage qu'on a utilisé dans cette thèse.
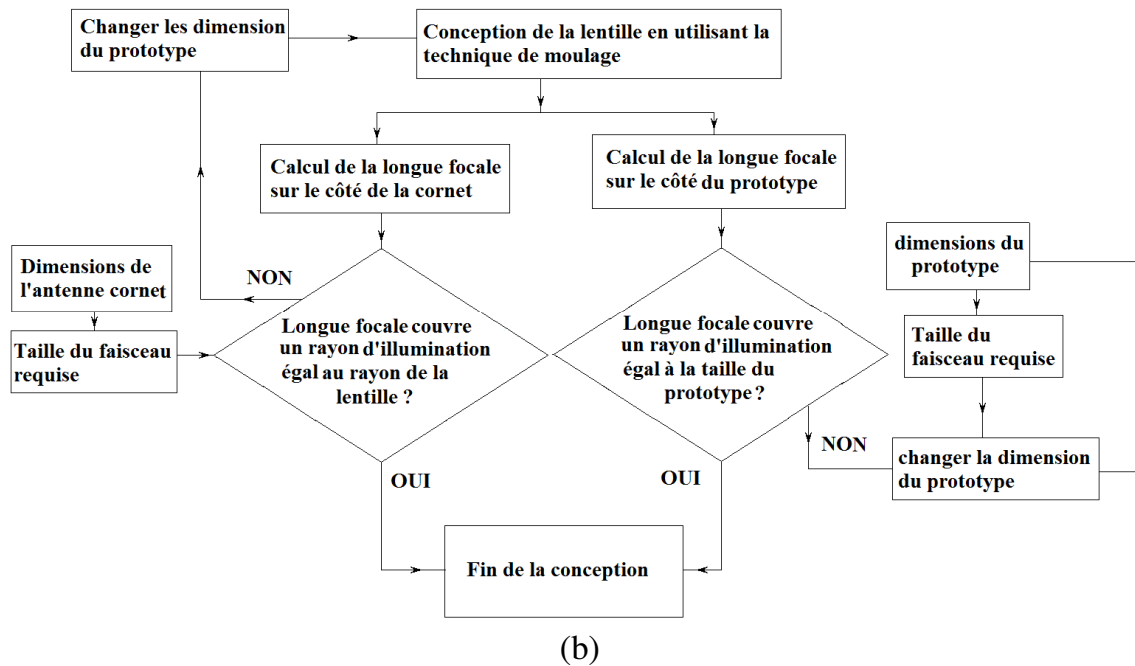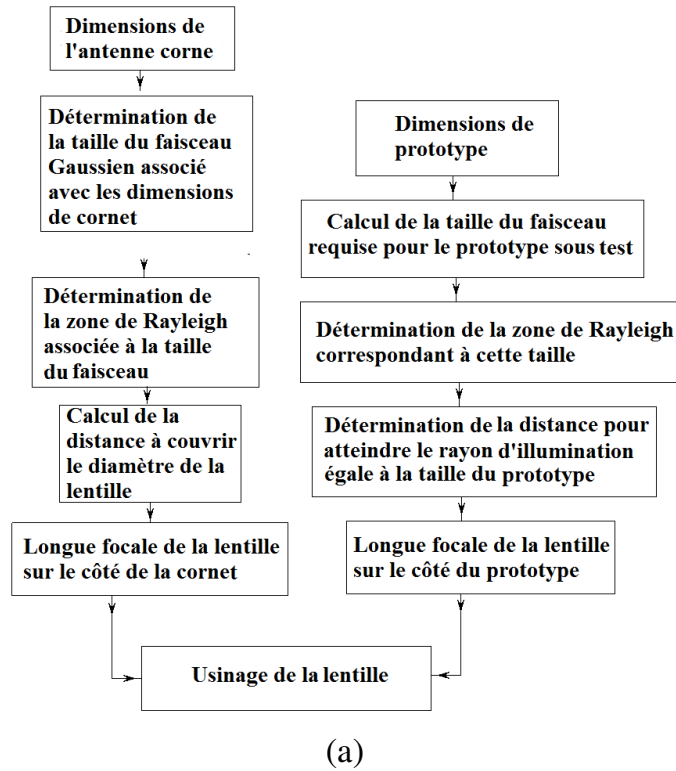
Fig. 10.36. Organigramme de (a) la méthode conventionnelle et (b) le procédé de moulage qu'on a utilisé dans cette thèse.

Comme déjà expliqué dans le chapitre 8, le moulage est très facile et économique pour les bandes S et C, mais on doit changer la taille du réseau des cellules en accord avec les dimensions de la lentille pour assurer que le faisceau qui sorte de la lentille illumine le prototype correctement. Pour ce faire, d'abord on calcule la zone de Rayleigh associée au longueur d'onde d'operation pour la ceinteure du faiseacu minimum w_0

$$z_0 = \frac{\pi w_0^2}{\lambda}$$

(10-24)

Après, on peut déterminer la taille maximale du réseau des cellules (w_i) pour la distance focale de z_1

(10-25)

$$z_1 = z_0 \sqrt{\left(\frac{w_i}{w_0}\right)^2 - 1}$$

Fig. 10.37 montre une photo des lentilles fabriquées

Fig. 10.37. Photo des lentilles fabriquées en utilisant le procédé de moulage.

10.8. Conclusion

Dans cette thèse, les applications des métamatériaux à la réalisation d'antennes reconfigurables en diagramme de rayonnement ont été étudiées. D'abord une nouvelle cellule est conçue, et après on a utilisé cette cellule dans la structure d'une antenne planaire pour balayage du faisceau d'antenne dans le plan E. Il importe de mentionner que dans le processus de la conception de cette cellule, on a développé une méthode de miniaturisation qui est appelée la technique de résonateur à impédance échelonnée. Puis, la cellule proposée est utilisée dans la structure d'une antenne travaillant dans la bande S, pour commuter le faisceau d'antenne dans le plan E. Enfin, le même concept est utilisé dans la structure d'une antenne aux ondes millimétriques mais avec des cellules non-reconfigurables. Ces deux antennes fournissent des solutions prometteuses pour les réseaux sans fil à grande vitesse. Une autre contribution de cette thèse est une nouvelle technique de mesure pour la caractérisation des cellules métamatériaux dans la bande S. Dans cette méthode, on a fabriqué une lentille diélectrique en utilisant le procédé de moulage.

10.9. Axes pour les traveaux futures

Le travail qui a été effectué dans cette thèse ouvre le domaine des cellules planaires métamatériaux reconfigurables et propose leurs applications dans la réalisation d'antennes reconfigurables en diagramme de rayonnement. Cependant, il est évident qu'il y a encore beaucoup d'autres sujets dans ce domaine. La première direction est basée sur les autres types de cellules métamatériaux qui peuvent être utilisées pour fournir un indice de réfraction contrôlable. Par exemple, on peut employer les cellules reconfigurable avec d'indice gradient pour délivrer un indice de réfraction plus lisse et donc présenter une meilleure réponse en fréquence. La deuxième recommandation est liée à la technique de reconfiguration. En fait, on peut utiliser des éléments comme RF-MEMS pour concevoir la future génération des cellules reconfigurables. De plus, en améliorant de la technologie de fabrication, on peut atteindre des meilleurs niveaux de miniaturisation. D'autre part, au niveau de l'antenne, la technologie de commutation de faisceaux peut être étendue par rapport au plan d'élévation en incorporant les cellules dans une structure 3D. Ce concept a beaucoup de potentiel et peut être utilisé pour dévier le faisceau d'antenne dans une direction arbitraire dans l'espace. Enfin, la possibilité d'amélioration de gain en même temps que la permutation du faisceau, qui est un aspect très intéressant de ce travail, peut être considérée comme une axe de recherche important pour l'extension de cette thèse.

References

[1] J. C. Liberti and T. S. Rappaport, *Smart Antennas for Wireless Communications: IS-95 and Third Generation CDMA Applications*, Prentice Hall, 1999.

[2] S. Lim and H. Ling, "Design of Electrically Small Pattern Reconfigurable Yagi Antenna," *IET Elec. Lett.* vol. 43, no. 24, pp. 1326-1327, 2007.

[3] M. Hajj, T. Monediere, B. Jecko and R. Chantalat "A novel directivity/beam reconfigurable M-EBG antenna," in *IEEE Intl. Symp. Antenna Propag. (APSURSI),* pp. 1-4, Toronto, Canada, July 2010.

[4] A. B. Guntupalli and Ke Wu, "Polarization-Agile Millimeter-Wave Antenna Arrays," in *Asia-Pacific Microw. Conf. Proced. (APMC),* pp. 148-150, Kaohsiung, Taiwan, Dec. 2012.

[5] J. L. Araque Quijano, and G. Vecchi, "Optimization of a Compact Frequency and Environment Reconfigurable Antenna," *IEEE Trans. Antennas Propag.*, vol. 60, no. 6, pp. 2682-2689, Jun. 2012.

[6] P. Wang, Y. Li, L. Song and B. Vucetic, "Multi-gigabit millimeter wave wireless communications for 5G: from fixed access to cellular networks," *IEEE Communications Magazine*, vol. 53, no. 1, pp. 168-178, Jan. 2015.

[7] A. Elboushi and A. Sebak, "MMW Sensor for Hidden Targets Detection and Warning Based on Reflection/Scattering Approach," *IEEE Trans. Antennas Propag.* vol. 62. no. 9, pp. 4890-4894, Jul. 2014.

[8] J. Hasch, E. Topak, R. Schnabel, T. Zwick, R. Weigel and C. Waldschmidt, "Millimeter-Wave Technology for Automotive Radar Sensors in the 77 GHz Frequency Band," *IEEE Trans. Mircow. Theory Tech.,* vol. 60, no. 3, pp. 845-860, Jan. 2012.

[9] M. Thumm "Recent applications of millimeter and submillimeter wave gyrotrons," in *Intl. Conf. on Infrared & Millimeter waves,* pp. 99-102, Beijing, China, Sep. 2000.

[10] N. Engheta and R. Ziolkowski, "A positive future for double-negative metamaterials," *IEEE Trans. Microw. Theory Tech.*, vol. 53, no. 4, pp. 1535-1556, April 2005.

[11] N. Engheta and R. Ziolkowski, "Metamaterials: Physics and Engineering Explorations," Wiley-IEEE Press, Sep. 2006.

[12] N. Zheludev, "The Road Ahead for Metamaterials," *Science*, vol. 328, no. 5978, pp. 582-583, April 2010.

[13] J. J. Luther, S. Ebadi, and X. Gong, "A microstrip patch electronically steerable parasitic array radiator (ESPAR) antenna with reactance-tuned coupling and maintained resonance," *IEEE Trans. Antennas Propag.*, vol. 60, no. 4, pp. 1803–1813, Sep. 2012.

[14] A. Dadgarpour, B. Zarghooni, B. S. Virdee and T. A. Denidni, "Beam Tilting Antenna using Integrated Metamaterial Loading," *IEEE Trans. Antennas Propag.*, vol. 62, no. 5, pp. 2874-2879, Feb. 2014.

[15] B. Zarghooni, A. Dadgarpour and T. A. Denidni, "Greek-key Pattern as a Miniaturized Multibalnd Metamaterial Unit-cell," *IEEE Antennas Wireless Propag. Lett.* vol. 14, pp. 1254-1257, Feb. 2015.

[16] B. Zarghooni, A. Dadgarpour and T. A. Denidni, "Reconfigurable Planar Metamaterial Unit-cell," *IET Microw. Antennas Propag.,* March 2015.

[17] A. J. Fenn, *Adaptive Antennas and Phased Arrays for Radar and Communication Systems,* Artech House, 2008.

[18] J. T. Bernard, *Reconfigurable Antennas*, Morgan & Claypool publication series, 2007.

[19] A. Daryoush, P. Herczfeld, V. Contarino and A. Rosen, "Optical Beam Control of Millimeter Wave Phased Array Antennas for Communications," in *16th Europen Microwave Conference*, Dublin, Ireland, Sep. 1986.

[20] M. Kam, W. Jeffrey and P. Herczfeld, "The Impact of Phase-Shifter Sharing on Beam Parameters in Optically Steered Antenna Arrays," *MILCOM*, Washington, USA, 1987.

[21] J. C. Langer, J. Zou, C. Liu and J. T. Bernhard, "Micromachined reconfigurable out-of-plane microstrip patch antenna using plastic deformation magnetic actuation," *IEEE Lett. Microw. Comp.,* vol. 13, no. 3, pp. 120-122, March 2003.

[22] W. Kim, M. F. Iskander and W. D. Palmer, "An Integrated Phased Array Antenna Design Using Ferroelectric Materials and the Continuous Transverse Stub Technology," *IEEE Trasn. on Ant. and Propag.*, Vol. 54 (No. 11), p. p. 3095-3105, 2006.

[23] R. R. Romanofsky, "Advances in Scanning Reflectarray Antennas Based on Ferroelectric Thin-Film Phase Shifters for Deep-Space Communications," *IEEE Proceedings*, Vol. 95 (No. 10), p. p. 1968-1975, 2007.

[24] S. L. Preston, D. V. Thiel, J. W. Lu, S. G. O'Keefe and T. S. Bird, "Electronic Beam Steering Using Switched Parasitic Patch Elements," *Elec. Lett.*, Vol. 33 (No. 1), p. p. 7-8, 1997.

[25] M. N. Jazi and T. A. Denidni, "Agile Radiation-Pattern Antenna Based on Active Cylindrical Frequency Selective Surfaces," *IEEE* on *Antennas and Wireless Propag. Lett.,* Vol. 9, p. p. 387-388, 2010.

[26] M. N. Jazi and T. A. Denidni, "Frequency Selective Surfaces and Their Applications for Nimble-Radiation Pattern Antennas," *IEEE Trans. on Ant. and Propag.*, Vol. 58 (No. 7), p. p. 2227-2237, 2010.

[27] A. Edalati and T. A. Denidni, "High-Gain Reconfigurable Sectoral Antenna Using an Active Cylindrical FSS Structure," *IEEE Trans. on Ant. and Propag.*, Vol. 59 (No. 7), p. p. 2464-2472, 2011.

[28] M. N. Jazi and T. A. Denidni, "Frequency Selective Surfaces and Their Applications for Nimble-Radiation Pattern Antennas," *IEEE Trans. on Ant. and Propag.*, Vol. 58 (No. 7), p. p. 2227-2237, 2010.

[29] M. N. Jazi and T. A. Denidni, "Agile Radiation-Pattern Antenna Based on Active Cylindrical Frequency Selective Surfaces," *IEEE* on *Antennas and Wireless Propag. Lett.,* Vol. 9, p. p. 387-388, 2010.

[30] U. Madhow, "Networking at 60 GHz: The emergence of multiGigabit wireless," in *Second Intl. Conf. on Communication Systems and Networks (COMSNETS),* pp. 1-6, Banglore, Jan 2010.

[31] K. Ohata "Sixty-GHz-band ultra-miniature monolithic T/R modules for multimedia wireless communication systems," *IEEE Trans. Microw. Theory Tech.*, vol. 44, no. 12, pp. 2354 -2360, 1996.

[32] E. E. Altshuler and R. A. Marr, "A comparison of experimental and theoretical values of atmospheric absorption at the longer millimeter wavelengths," IEEE Trans. Antennas Propag., vol. AP-36, no. 10, pp. 1471–1480, Oct. 1988.

[33] FCC 03-248, "Allocation and service rules for the 71-76GHz, 81-86GHz, and 92-95GHz bands," *Federal Communication Commission*, Nov. 2003.

[34] SPP 2006-11, "Planning of the 71-76 GHz and 81-86 GHz bands for millimeter wave high capacity fixed link technology," *Australian communication and media authority*, Dec. 2006.

[35] Hodges, R.J. Badley, and Tarsier, "A millimeter wave radar for airport runway debris detection," *in Proc. European Radar Conf.*, Amsterdam, 2004.

[36] B.D. Nguyen, J. Lanteri, J.-Y. Dauvignac, C. Pichot, and C. Migliaccio, "94 GHz folded Fresnel reflector using C-patch elements," *IEEE Trans. Antennas Propag.*, vol. 55, pp. 3373–3381, Nov. 2008.

[37] L. Yujiri, M. Shoucri, and P. Moffa, "Passive millimeter wave imaging," *IEEE Microwave Magazine*, vol. 4, pp. 39-50, 2003.

[38] M. Xu, A. Rahim and P. Nuechter, "Investigation of system parameters of mm-wave point to point radios," *IEEE Intl. Conf. in Central Asia on Internet*, Sep. 2005.

[39] A. D. Brown, L. C. Kempel and J. L. Volakis, "Design method for antenna arrays employing ferrite printed transmission line phase shifters," *IEE Proceedings Microwav. Antenna Propag.* vol. 149, no. 1, pp. 33-40, Feb. 2002.

[40] M. Y. Ismail and R. Cahil, "Beam steering reflectarrays using liquid crystal substrate," *High Frequency Postgraduate Student Colloquium*, pp. 62-65, Sep. 2005.

[41] E. B. Lima, J. R. Costa and C. A. Fernandes, "Mechanical beam-steerable elliptical dome lens," in *3rd European Conf. on Antennas Propag.,* pp. 1814-1818, March 2009.

[42] P. Y. Qin, A. R. Weily, Y. J. Guo and C-H Liang "Millimeter wave frequency reconfigurable quasi-Yagi antenna," Asia-Pacific Microw. Conf. Proceedings (APMC), pp. 642-645, Yokohama, Dec. 2010.

[43] R. O. Ouedraogo, E. J. Rothwell and B. J. Greetis "A Reconfigurable Microstrip Leaky-Wave Antenna With a Broadly Steerable Beam," *IEEE Trans Antenna Propag.*, vol. 59, no. 8, pp. 3080-3083, June 2011.

[44] G. M. Rebeiz and J. B. Muldavin, "RF MEMS switches and switch circuits," *IEEE Microwave Magazine,* vol. 2, no. 4, pp. 59-71, Dec. 2001.

[45] S. Cheng, P. Rantakari, R. Malmqvist, C. Samuelsson, T. Vähä-Heikkilä, A. Rydberg, and J. Varis "Switched Beam Antenna Based on RF MEMS SPDT Switch on Quartz Substrate," *IEEE Lett. Antenna Propag.* vol. 8, pp. 383-386, March 2009.

[46] J. C. Bose, "On the Rotation of Plane of Polarisation of Electric Waves by a Twisted Structure," *Proceedings of the Royal Society 63: 146*, 1898.

[47] I. V. Lindell, A. Sihvola, J. Kurkijarvi "Karl F. Lindman: The last Hertzian, and a harbinger of electromagnetic chirality". *IEEE Antennas Propag. Magazine* vol. 34, no. 3, pp. 24–30, 1992.

[48] W. Kock, "Path-Length Microwave Lenses," *Proceedings of the Institute of Radio Engineers*, vol. 37, no. 8, pp. 852–855, August 1949.

[49] V. G. Veselago, "The electrodynamics of substances with simultaneously negative values of ε and μ*," Soviet Physics Uspekhi*, vol. 10, no. 4, Jan 1968.

[50] J. B. Pendry, A. J. Holden, W. J. Stewart and D. J. Robbins "Low frequency plasmons in thin wire structures," *J. Phys.: Condensed Matter* 10, pp. 4785-4809, Mar. 1998.

[51] J. B. Pendry, A. J. Holden, D. J. Robbins and W. J. Stewart "Magnetism from conductors and enhanced nonlinear phenomena," *IEEE Trans. Microwave Theory Tech.*, vol. 47, no. 11, pp.2075-2084, Nov. 1999.

[52] D. R. Smith, W. J. Padilla, D. C. Vier, S. C. Nemat Nasser, and S. Schultz, "Composite medium with simultaneously negative permeability and permittivity," *Phys. Rev. Lett.*, vol. 84, no. 18, pp. 4184-4187, May 2000.

[53] J. B. Pendry, "Negative refraction makes a perfect lens," *Phys. Rev. Lett.*, vol. 85, no. 18, pp. 3966–3969, Oct. 2000.

[54] C. Caloz, H. Okabe, T. Iwai, T. Itoh, "Transmission line approach of left-handed materials," *in IEEE AP-S International Symposium and USNC/URSI National Radio Science Meeting*, San Antonio, USA, June, 2002.

[55] X. Chen, Y. Luo, J. Zhang, K. Jiang, J. B. Pendry and S. Zhang "Macroscopic invisibility cloaking of visible light," *Nature Communications*, Feb. 2011.

[56] R. W. Ziolkowski and E. Heyman, "Wave propagation in media having negative permittivity and permeability," *Phys. Rev. E*, vol. 64, no. 5, Oct. 2001.

[57] T. J. Cui, D. R. Smith and R. Liu, *Metamaterials, Theory, Design and Applications,* Springer, 2010.

[58] W. Rotman, "Plasma simulation by artificial dielectrics and parallel-plate media," *IEEE Trans. Antennas Propag.*, vol. 10, no. 1, pp. 82–95, Jan. 1962.

[59] J. B. Pendry, A. Holden, J. D. Robbins, and J.W. Stewart, "Magnetism from conductors ☐and enhanced nonlinear phenomena," *IEEE Trans. MTT*, vol. 47, no. 11, pp. 2075 – 2084, ☐Nov. 1999.

[60] X. Chen, T. M. Grzegorczyk, B. I. Wu, J. Pacheco Jr., and J. A. Kong, "Robust method to retrieve the constitutive effective parameters of metamaterials," *Phys. Rev. Lett.,* E 70, 016608 (2004).

[61] Z. Szabo, Gi-Ho Park, R. Hedge and Er-Ping Li, "A Unique Extraction of Metamaterial Parameters Based on Kramers–Kronig Relationship," *IEEE Trans. Microw. Theory Tech.,* vol. 58, no. 10, pp. 1451-1461, Oct. 2010.

[62] R. Marques, F. Mesa, J. Martel, and F. Medina, "Comparative analysis of edge- and broadside-coupled split ring resonators for metamaterial design-theory and experiments," *IEEE Trans. Antennas Propag.,* vol. 51, no. 10, pp. 2572–2581, Oct. 2003.

[63] R. Shelby, D. Smith, and S. Schultz, "Experimental verification of a negative index of refraction," *Science*, vol. 292, pp. 77–79, Apr. 2001.

[64] M. M. I. Saadoum and N. Engheta, "A reciprocal phase shifter using novel pseudochiral or omega medium," *Microwave Opt. Technol. Lett.*, vol. 5, pp. 184–188, Apr. 1992.

[65] H. Chen, L. Ran, J. Huangfu, X. Zhang, K. Chen, T. M. Grzegorczyk, and J. A. Kong, "Left-handed metamaterials composed of only S-shaped resonators," *Phys. Rev. E*, vol. 70, 057605, 2004.

[66] B. Zarghooni and T. A. Denidni, " New Compact Metamaterial Unit-Cell Using SIR Technique," *IEEE Lett. Antenna Propag.,* vol. 24, no. 5, pp. 315-317, March 2014.

[67] A. Dadgarpour, B. Zarghooni, B. S. Virdee and T. A. Denidni, "Beam Tilting Antenna using Integrated Metamaterial Loading," *IEEE Trans. Antennas Propag.*, vol. 62, no. 5, pp. 2874-2879, Feb. 2014.

[68] M. A. Antoniades and G. V. Eleftheriades, "Compact, linear, lead/lag metamaterial phase shifters for broadband applications," *IEEE Antennas Wireless Propag. Lett.*, vol. 2, no. 7, pp. 103–106, July 2003.

[69] M. Sun, Z. N. Chen, and X. Qing "Gain Enhancement of 60-GHz Antipodal Tapered Slot Antenna Using Zero-Index Metamaterial," *IEEE Trans Antenna Propag.* vol. 61, no. 4, pp. 1741-1746, April 2013.

[70] D. Li, Z. Szabó, X. Qing, E. P. Li, and Z. N. Chen "A High Gain Antenna With an Optimized Metamaterial Inspired Superstrate," *IEEE Trans Antenna Propag.* vol. 60, no. 12, pp. 6018-6023, Dec. 2012.

[71] W. Cao, Y. Xiang, B. Zhang, A. Liu, T. Yu, and D. Guo "A Low-Cost Compact Patch Antenna With Beam Steering Based on CSRR-Loaded Ground," *IEEE Lett. Antenna Propag.* vol. 10, no. 5, pp. 1520-1523, Dec. 2011.

[72] B. Zarghooni, A. Dadgarpour and T. A. Denidni, "Greek-key Pattern as a Miniaturized Multibalnd Metamaterial Unit-cell," *IEEE Antennas Wireless Propag. Lett.* vol. 14, pp. 1254-1257, Feb. 2015.

[73] B. Zarghooni and T. A. Denidni, "Agile Double Negative Metamaterial Unit-cell for Advanced Antenna Applications," in *Int. Symp. on Antenna Tech. and Applied Electromagnetics (ANTEM)*, Toulouse, France, June 2012.

[74] B. Zarghooni and T. A. Denidni, "Miniaturized DNG Superstrate for Microstrip Antenna Applications," in *IEEE Int. Symp. on Antennas and Propag. (APSURSI)*, Orlando, USA, July 2013.

[75] J. D. Baena, R. Marques, and F. Medina, "Artificial magnetic metamaterial design by using spiral resonators," *Phys. Rev. B* 69–014402, 2004.

[76] B. Zarghooni and T. A. Denidni, "New Fractal Metamaterial Unit-cell for Microwave Applications," in *European Conference on Antennas Propag. (EuCap),* April 2014.

[77] B. Zarghooni, A. Dadgarpour and T. A. Denidni, "Effect of Stepped-Impedance Resonators on Rectangular Metamaterial Unit-cells," *Wiley Intl. Journal of RF & Microw. Computer Aided Eng.* Feb. 2015.

[78] M. Makimoto and S. Yamashita, "Compact Bandpass Filters Using Stepped Impedance Resonators," Proceedings of IEEE, vol. 67, no. 1, pp. 16-19, Jan. 1979.

[79] M. Makimoto and S. Yamashita, *Microwave Resonators and Filters for Wireless Communication, Theory, Design and Application,* Springer, 2000.

[80] B.C. Wadell, *Transmission line design handbook*, Artech House, Boston, MA, 1991.

[81] D.M. Pozar, *Microwave engineering*, 3rd ed., Wiley, MA, USA, 2004.

[82] B. Zarghooni, A. Dadgarpour and T. A. Denidni, "Reconfigurable Planar Metamaterial Unit-cell," *IET Microw. Antennas Propag.,* March 2015.

[83] J. Wu, Z. Zhao, Z. Nie and Q-H Liu, "Design of a Wideband Planar Printed Quasi-Yagi Antenna Using Stepped Connection Structure," *IEEE Trans Antenna Propag,* vol. 62, no. 6, pp. 3431-3435, June 2014.

[84] C. Park and T. Rappaport, "Short range Wireless Communications for Next Generation Networks: UWB, 60 GHz millimeter wave WPAN and Zigbee," *IEEE Wireless Communications,* vol. 14, no. 4, pp. 70-78, Aug. 2007.

[85] A. Maltsev, R. Maslennikov, A. Sevastyanov, A. Lomayev, A. Khoryaev, A. Davydov and V. Ssorin, "Characteristics of Indoor Millimeter-Wave Channel at 60 GHz in Application to Perspective WLAN System," *European Conf Antenna Propag (EuCap),*

April 2010.

[86] H. T. Friis, "A note on a simple transmission formula," *Proc. I.R.E. and Waves and Electrons,* pp. 254–256, May 1946.

[87] D. A. Fittipaldi, S. Skafidas, and M. Luise, "IEEE 802.15.3c medium access controller throughput for phased array systems," in Proc. 18th Annu. *IEEE Int. Symp. Personal, Indoor, Mobile Radio Commun. (PIMRC'07),* Athens, Greece, Sep. 2007, pp. 1–5.

[88] K. Hosoya, N. Parsad, K. Ramachandran, N. Orihashi, S. Kishimoto, S. Rangarajan and Kenichi Maruhashi, "Multiple Sector ID Capture (MIDC): A Novel Beamforming Technique for 60-GHz Band Multi- Gbps WLAN/PAN Systems," *IEEE Trans Antenna Propag.* vol. 63, no. 1, Jan 2015.

[89] P. Deo, D. Mirshekar-Syahkal, L. Seddon, S. E. Day and F. A. Fernandez "60 GHz id crystal phased array using reflection-type phase shifter," *European Conf. on Antennas and Propag.,* pp. 927-929, April 2013.

[90] C-H. Tseng, J-C. Chen and T-H Chu "A low-cost 60-GHz switched- beam patch antenna array with butler matrix network," *IEEE Lett. Antenna. Propag.* vol.7, pp.432-435, 2008.

[91] R. M. Alhalabi and G. M. Rebeiz, "High-Efficiency Angled-Dipole Antennas for Millimeter-Wave Phased Array Applications," *IEEE Trans Antenna Propag.,* vol. 56, no. 10, pp. 3136-3142, Oct. 2008.

[92] A. Parkash, J. K. Vaid, and A. Mansingh, "Measurement of dielectric parameters at microwave frequencies by cavity- perturbation technique," *IEEE Trans. Microw. Theory Tech.*, vol. MTT-27, no. 9, pp. 791–795, Sep. 1979.

[93] H. Chen, J. Zhang, Y. Bai, Y. Luo, L. Ran, Q. Jiang, and J. A. Kong, "Experimental retrieval of the effective parameters of metamaterials based on a waveguide method" *Optics Express* 12949 Vol. 14, No. 26, Dec. 2006.

[94] Long Li, Yingchun Fan, Shixing Yu, Cheng Zhu and Changhong Liang, "Design, fabrication and measurement of highly sub-wavelength double negative metamaterials at high frequencies," *Journal of Applied Phys.* 113, 213712, Sep. 2013.

[95] J. W. Schultz, "Focused Beam Methods, Measuring Microwave Materials in Free Space," 2012.

[96] P. F. Goldsmith, "Quasioptical Systems, Gaussian Beam Quasioptical Propagation and Applications," *IEEE Press*, 1998.

[97] J. Musil, F. Zacek, *Microwave Measurement of Complex Permittivity by Free Space Methods and Their Applications*, Elsevier.

[98] P. F. Goldsmith, T. Itoh, K. D. Stephan, "Quasi-Optical Techniques," in Handbook of Microwave and Optical Components, vol. 1, Wiley, 344-363, 1989.